

University of Kentucky

UKnowledge

Theses and Dissertations--Electrical and
Computer Engineering

Electrical and Computer Engineering


2023

Building Energy Modeling and Studies of Electric Power Distribution Systems with Distributed Energy Resources

Evan S. Jones

University of Kentucky, sevanjones@outlook.com

Author ORCID Identifier:

 <https://orcid.org/0000-0001-8325-9752>

Digital Object Identifier: <https://doi.org/10.13023/etd.2023.163>

[Right click to open a feedback form in a new tab to let us know how this document benefits you.](#)

Recommended Citation

Jones, Evan S., "Building Energy Modeling and Studies of Electric Power Distribution Systems with Distributed Energy Resources" (2023). *Theses and Dissertations--Electrical and Computer Engineering*. 191.

https://uknowledge.uky.edu/ece_etds/191

This Doctoral Dissertation is brought to you for free and open access by the Electrical and Computer Engineering at UKnowledge. It has been accepted for inclusion in Theses and Dissertations--Electrical and Computer Engineering by an authorized administrator of UKnowledge. For more information, please contact UKnowledge@lsv.uky.edu.

STUDENT AGREEMENT:

I represent that my thesis or dissertation and abstract are my original work. Proper attribution has been given to all outside sources. I understand that I am solely responsible for obtaining any needed copyright permissions. I have obtained needed written permission statement(s) from the owner(s) of each third-party copyrighted matter to be included in my work, allowing electronic distribution (if such use is not permitted by the fair use doctrine) which will be submitted to UKnowledge as Additional File.

I hereby grant to The University of Kentucky and its agents the irrevocable, non-exclusive, and royalty-free license to archive and make accessible my work in whole or in part in all forms of media, now or hereafter known. I agree that the document mentioned above may be made available immediately for worldwide access unless an embargo applies.

I retain all other ownership rights to the copyright of my work. I also retain the right to use in future works (such as articles or books) all or part of my work. I understand that I am free to register the copyright to my work.

REVIEW, APPROVAL AND ACCEPTANCE

The document mentioned above has been reviewed and accepted by the student's advisor, on behalf of the advisory committee, and by the Director of Graduate Studies (DGS), on behalf of the program; we verify that this is the final, approved version of the student's thesis including all changes required by the advisory committee. The undersigned agree to abide by the statements above.

Evan S. Jones, Student

Dr. Dan M. Ionel, Major Professor

Dr. Daniel Lau, Director of Graduate Studies

BUILDING ENERGY MODELING AND STUDIES OF ELECTRIC POWER
DISTRIBUTION SYSTEMS WITH DISTRIBUTED ENERGY RESOURCES

DISSERTATION

A dissertation submitted in partial fulfillment of the requirements for the
degree of Doctor of Philosophy in the College of Engineering at the
University of Kentucky

By

Evan S. Jones

Lexington, Kentucky

Director: Dr. Dan M. Ionel, Professor and L. Stanley Pigman Chair in Power

Lexington, Kentucky

2023

Copyright© Evan S. Jones 2023

ABSTRACT OF DISSERTATION

BUILDING ENERGY MODELING AND STUDIES OF ELECTRIC POWER DISTRIBUTION SYSTEMS WITH DISTRIBUTED ENERGY RESOURCES

There is significant opportunity for savings in energy and investment from improved performance of electric Power Distribution Systems (PDSs) through optimal planning and operation of conventional voltage-controlling devices. Novel multi-step model conversion and optimal capacitor planning (OCP) procedures are proposed for large-scale utility PDSs and are exemplified with an existing utility circuit of approximately 4,000 buses. Simulated optimal control and operation is achieved with a cluster-based approach that utilizes load-forecasting to minimize equipment degradation by intelligently dispersing device setting adjustments over time such that they remain most applicable.

Improved performance may also be achieved through smart building technologies and Virtual Power Plant (VPP) control of increasingly more prevalent Distributed Energy Resources (DERs). The established simulation test bed for PDSs incorporates DERs to evaluate VPP implementations and an optimization process for control timing is proposed that minimizes targeted peak power and possible resulting increase in total daily energy. The advanced VPP controls incorporate the Consumer Technology Association (CTA) 2045 standard and EnergyStar performance characterizations to leverage HVAC systems as Generalized Energy Storage (GES) for load manipulation and to support the integration of demand-side generating DERs, such as local solar Photo-Voltaic (PV) systems.

KEYWORDS: Distributed Energy Resource (DER), Generalized Energy Storage (GES), Power Distribution System (PDS), Smart Grids, Smart Homes, Virtual Power Plant (VPP).

Author's signature: Evan S. Jones

Date: May 1, 2023

BUILDING ENERGY MODELING AND STUDIES OF ELECTRIC POWER
DISTRIBUTION SYSTEMS WITH DISTRIBUTED ENERGY RESOURCES

By
Evan S. Jones

Director of Thesis: Dr. Dan M. Ionel

Director of Graduate Studies: Dr. Daniel Lau

Date: May 1, 2023

ACKNOWLEDGMENTS

It is to my Ph.D. advisor and mentor, Professor Dan M. Ionel, Ph.D., FIEEE, L. Stanley Pigman Chair in Power, Prof, that I owe profound gratitude and the most appreciation. As a great supporter with significant experience, he guided my growth and decisions as a student, engineer, and researcher. This invaluable guidance and his teachings led me through my Ph.D. studies and prepared me to excel in my profession. His ability to identify and foster the potential in others facilitated my own realization of my personal academic ability and inspired my contributions to the Power and Energy field.

It is this ability that also led to the congregation of the SPARK group, which is a collection of incredibly intelligent, strong-willed, and supportive individuals whom I consider my academic family. I am most thankful to have had the opportunity to learn from, contribute with, and befriend my student colleagues, in approximate chronological order, Narges, Akeyo, Murat, Huangjie, Yibin, Damien, Rosemary, Donovan, Gerald, Yaser, Ali, Badewa, Matin, and Steven as well as my postdoctoral colleagues: Drs. Vandana Rallabandi, Peng Han, and Abdullah Al Hadi.

At UK, I am especially thankful for the advice and feedback received from my Ph.D. Committee members Drs. Nicholas Jewell, Yuan Liao, Silvestri Simone, Joseph Sottile, and external examiner Professor Zongming Fei.

The continued support of University of Kentucky, the L. Stanly Pigman Chair in Power Endowment is gratefully acknowledged. The support of the Department of Education's (DoEd) GAANN Fellowship Program through the University of Kentucky Electrical and Computer Engineering Department and the Department of Energy (DOE) through the project DEEE000902 led by the Electric Power Research Institute (EPRI) is also gratefully acknowledged. My great appreciation is also due to the support of Louisville Gas and Electric and Kentucky Utilities, part of the PPL Corporation family of companies, and the Tennessee Valley Authority (TVA). Any opinions, findings, and conclusions, or recommendations expressed in this material are those of the author and do not necessarily reflect the views of DOE, DoEd, LG&E and KU, PPL, and TVA.

At LG&E and KU, special thanks are due to Mr. Aron Patrick and Dr. Nicholas Jewell for their advice and support on topics of power systems and renewable energy, including access to experimental data and equipment. At TVA, special thanks are due to Mr. Andrew Frye for his collaboration on smart buildings and grids.

I am most grateful to Mr. and Mrs. Stanley and Karen Pigman for their personal mentorship and for their significant support to UK and SPARK.

I would also like to express my sincere and unlimited gratitude for my parents, Stewart and Pamela Jones, as well as my Aunt Barbara Bell and brother Seth Jones for their unconditional love and sacrifice that helped me to become the person capable of this accomplishment. My greatest appreciation also goes to my loving wife Brooklyn Jones who has stood as a constant source of support and comfort over the last eight years during both the most difficult and best of times.

Evan S. Jones
April, 2023

TABLE OF CONTENTS

Acknowledgements		iii
List of Tables		vii
List of Figures		xiv
1	Introduction	1
1.1	Background	1
1.2	Literature Review	3
1.3	Research Objectives and Original Contributions	5
1.4	Dissertation Outline	9
1.5	Main Publications	9
2	Planning and Optimization for Electric Power Distribution Systems	13
2.1	Introduction and Main Problem	13
2.2	Conventional Approaches	17
2.3	Electric Power Distribution System Modeling	20
2.4	Large-Scale Utility Circuit Model Conversion	24
2.5	Problem Formulation and Sensitivity Analysis for Candidate Installation Buses	31
2.6	Optimization Algorithms	34
2.7	Multi-objective Optimization Methods	39
2.8	Optimal Configuration Selection through Sub-circuit Analysis	45
2.9	Time Series Evaluation of Circuit Configurations	52
2.10	Summary	58
3	Optimal Operation of Voltage-Controlling Devices in Distribution Systems	61
3.1	Introduction and Main Problem	61
3.2	Time Series Power Distribution System Simulation with ZIP Load Modeling	64
3.3	Baseline Case with Conventional Controls	68
3.4	Best Performance Case with Optimal Operation and Unlimited Adjustments	71
3.5	New Cluster-based Method for Improved Optimal Controls	74
3.6	Comparative Studies and Discussion	83
3.7	Summary	87

4	Electric Power and Energy for Smart Buildings	89
4.1	Introduction and Main Problem	89
4.2	Field Demonstrators	93
4.3	Physics-based HVAC and Building Modeling with EnergyPlus	95
4.4	HVAC and Building Technologies and their Effect on Energy Usage	99
4.5	Water Heaters and Other Appliances	103
4.6	Rooftop PV Performance for Different Geographical Locations	106
4.7	Appliance Power Factor and Reactive Power	111
4.8	Summary	118
5	Virtual Power Plant Control of Smart Homes and Grids	120
5.1	Introduction and Main Problem	120
5.2	Models for Buildings, Energy Storage, and PV Generation	124
5.3	Power System and DER Operation	132
5.4	Problem Formulation and Algorithms for Optimal VPP Control of HVAC Systems	137
5.5	Case Study and Discussion of Optimal Control Settings	143
5.6	Individual Building and Occupant Effects	146
5.7	Summary	148
6	Conclusions	152
6.1	Summary	152
6.2	Original Contributions	155
6.3	Recommendations for Future Research	156
	References	158
	Vita	167

LIST OF TABLES

2.1	Global circuit conversion summary	27
2.2	Characteristics of the eight (8) considered optimization methods. . . .	40
2.3	Percent change to circuit characteristics applied by selected optimal configurations with respect to reference ("Ref") configuration and compromise factors as defined in Eq.2.30	48
3.1	The simulation results for the reference case from the equivalent ZIP parameter estimation as well as for the minimum and maximum cases from the sensitivity analysis. Percent change for the latter two cases is also indicated with respect to the reference case.	66
3.2	Simulation results for the four considered control cases.	83
3.3	Resulting percent changes [%] for the control cases with respect to the conventional case.	85
4.1	Monthly and annual comparison of simulation results to measured data of Conv19S based on actual locally measured weather data in 2013. . .	98
4.2	Monthly and annual comparison of simulation results to measured data of RetroF based on actual locally measured weather data in 2013. . .	98
4.3	Monthly and annual comparison of simulation results to measured data of Conv13S based on actual locally measured weather data in 2010. . .	99
4.4	Monthly and annual comparison of simulation results to measured data of NNZE based on actual locally measured weather data in 2010. . . .	101
4.5	Energy usage and peak power for different HVAC systems in the house models with Knoxville, TN TMY3 weather	102
4.6	Average hourly solar radiation, total annual PV energy generation calculated on an hourly basis, and CF for simulated locations based on TMY3 weather	108
4.7	PV ratings (kW) required to achieve NZE for houses of different types in all simulated locations	111
4.8	Energy and Power Factor Characteristics of Typical Residential Appliances in the U.S.	114
5.1	Results of optimal designs from the Pareto set and the baseline cases, including the maximum power during the evening peak (on-peak) as well as total energy for the full day, the on-peak time window, and off-peak time window.	143

5.2	The control time settings and resulting percent change with respect to the baseline case for all simulated cases in terms of maximum power during the evening peak (on-peak) as well as total energy for the full day, the on-peak time window, and off-peak time window.	143
5.3	Total energy during the “load-up” and “shed” time windows, which are different for each case based on the input time settings, with and without the controls active.	145
5.4	The BTM solar PV utilization for the baseline and control cases at different levels of penetration.	147

LIST OF FIGURES

2.1	Flowchart for the overall proposed OCP procedure with five main processes, including circuit modeling, candidate bus location determination, multi-objective optimization, solution selection considering objective priority, and selected configuration analysis.	16
2.2	Comparison of the Synergi and converted OpenDSS circuit model line and component mappings for the original configuration of the actual 48MW, 9Mvar power distribution system KUs1. Also included for comparison are both individual bus voltage and line loss analyses for the peak load instance. The OpenDSS circuit diagram is labeled with the top candidate bus locations for CB installation. Candidacy is determined by a sensitivity analysis in terms of power loss reduction factor (rf_w) as discussed in section 2.5. Change in voltage for buses with high rf_w causes relatively significant change in power losses for connected lines. Such buses typically cluster near the main distribution feeder lines.	24
2.3	Geographical circuit schematics of different characteristics for KUs1, including number of phases and conductor type for the line associated with the buses.	25
2.4	Summary of circuit conversion for KUs1 in terms of individual bus voltage, including Synergi and OpenDSS average bus voltages as well as the ratio and difference of Synergi to OpenDSS average bus voltages.	26
2.5	Circuit schematic of LGEs1, indicating the location of its 13 CBs.	28
2.6	Geographical circuit schematics of different characteristics for LGEs1, including number of phases and conductor type for the line associated with the buses.	29
2.7	Summary of circuit conversion for KUs1 in terms of individual bus voltage, including Synergi and OpenDSS average bus voltages as well as the ratio and difference of Synergi to OpenDSS average bus voltages.	30
2.8	Histogram for rf_w of all buses in the KUs1 circuit with no. of occurrences on a logarithmic scale. Buses with higher rf_w correspond to those most sensitive to CB installation. The red line marks the minimum cutoff rf_w for consideration of candidacy.	31
2.9	Comparison of resulting example Pareto sets for the KUs1 T1 sub-circuit from the most basic NM2 optimization employing the two considered optimization algorithms, NSDE (DE) and NSGA-III (GA), at different numbers of allowed generations as indicated legend labels.	34

2.10	Possible configurations and Pareto sets for the (a) NM2, (b) PM2, (c) NA2, and (d) PA2 methods. Configurations with voltage violations of more than 0 are not considered and not illustrated within any of the plots. Introducing the penalty constraint as illustrated with PM2 and PA2 increases the breadth of the search space. It also provides additional valid configurations along the Pareto sets that require less investment. Incorporating automatic LTC tap setting adjustment within the optimizer, as in NA2 and PA2, improves overall $w_{a,t}$ and $c_{r,t}$.	40
2.11	Possible configurations and Pareto sets for the three-objective (a) NM3, (b) PM3, (C) NA3, and (D) PA3 methods. Configurations with voltage violations of more than 0 are not considered and not illustrated within any of the plots. Effects observed in Fig. 2.10 remain present. The additional third objective increases focus by the optimizer in the region of increased $c_{r,t}$ and yields configurations with improved $v_{n,d}$, including some with penalty to $w_{a,t}$ and $c_{r,t}$, which indicates it's independence as a third objective.	41
2.12	Pareto sets of $w_{a,t}$ and $c_{r,t}$ for all eight (8) optimization methods. The introduction of automatic LTC tap adjustment improves overall $w_{a,t}$ and $c_{r,t}$, especially for configurations of lower $c_{r,t}$.	45
2.13	Pareto sets of $c_{r,t}$ and $v_{n,d}$ for all eight (8) optimization methods. $v_{n,d}$ is mostly dependent upon CB placement with some correlation to increased $c_{r,t}$ since more CBs are available to improve voltage uniformity.	46
2.14	Pareto sets of $w_{a,t}$ and $v_{n,d}$ for all eight (8) optimization methods. Higher tap settings in the LTC tap function-enabled NA3 and PA3 methods further reduce $w_{a,t}$, which was made possible in part by improved $v_{n,d}$.	46
2.15	Circuit diagrams with reference CB locations and bus voltages for the three KUs1 sub-circuits corresponding to substation transformers with manually calibrated tap settings such that voltages operate as low as possible without any voltage violations.	47
2.16	Possible configurations and Pareto set for T1. $v_{n,d}$ is exceptional for all configurations, including Ref, in comparison to T2 and T3. Improved $w_{a,t}$ is achieved with less $c_{r,t}$ with respect to Ref.	49
2.17	Possible configurations and Pareto set for T3. Considerable improvement of $v_{n,d}$ possible with reduced $c_{r,t}$ and $w_{a,t}$ compared to Ref.	49
2.18	Comparison of the three Pareto sets with shared axes to illustrate how each sub-circuit may benefit from OCP with respect to their corresponding reference configurations and to each other in terms of the three objectives. T1 can experience similar $w_{a,t}$ with much less $c_{r,t}$ than Ref and no penalty to $v_{n,d}$. Opportunity exists for T2 and T3 to improve in $v_{n,d}$ with less $w_{a,t}$. T2 can achieve this with even less $c_{r,t}$ than Ref, whereas T3 would require more to yield similar benefits.	50

2.19	Circuit bus voltages of the three sub-circuits for each selected configuration type. As anticipated, D reduces $v_{n,d}$ more than the other configurations. Both T2 and T3 experience more $v_{n,d}$ than T1 and have the most opportunity for improvement in that regard.	50
2.20	Example six month loadshape from January to June 2022 for total active (top) and reactive (bottom) power measured at the KUs1 T2 substation transformer every minute.	52
2.21	Two consecutive example days (left and right columns) from the full 180-day minutely simulations of KUs1 T2 in all considered configurations with results for LTC secondary bus voltage (top row) as well as total reactive power (middle row), and total active power losses (bottom row).	53
2.22	Comparison of distribution fits through CDFs of active power losses over an example week-long period.	54
2.23	Histograms and resulting PDFs assuming a normal distribution for each of the considered configuration types in terms of total active power losses.	55
2.24	Histograms and resulting PDFs assuming a normal distribution for each of the considered configuration types in terms of average voltage for all power system buses.	56
2.25	CDFs of total active power losses for each circuit configuration in (a) full and (b) zoomed in views.	59
2.26	CDF for average bus voltage of each circuit configuration case.	60
3.1	Circuit diagram of KUs1T1 with load at associated buses for an example time instance.	65
3.2	Sensitivity analysis results of all 10,000 simulation case in term of total active power.	67
3.3	Conventional control of LTC transformer taps from Beckwith Electric technical documents [1].	68
3.4	Bus voltage at the secondary side of the KUs1T1 LTC transformer with simulated conventional control.	69
3.5	Conventional control simulation results with voltage for each individual bus in KUs1T1.	70
3.6	Individual bus voltages monitored by the nine CBs of KUs1T1 for switching control.	70
3.7	Solution quality of various PDS characteristics and simulation time at different allowed no. of generations as indicated by the legend for the control optimization with unlimited adjustments. The simulation results are determined for an example day with respect to another simulation of no control.	73
3.8	Final LTC voltage results having run the control optimization with 20 generations for every timestep and with no limits to adjustments aside from the built-in CB discharge time limit.	74

3.9	Flowchart of time series PDS simulation with ZIP load modeling and the three considered control types.	75
3.10	The example day time-load profiles measured minutely at the substation transformers for KUs1T1 with the clusters of time most similar in total power determined by the machine learning K-means clustering algorithm.	76
3.11	Relationship between results for (top) total energy use and the control settings n_{clr} and $v_{t,m}$ over the example day for KUs1T1 with a (bottom) zoomed view of the case with the best selected settings.	79
3.12	Relationship between n_{clr} and resulting e_d , n_{adj} for LTC taps only, and $n_{vio,a}$ over the example day for KUs1T1 with (left) full-scale and (right) zoomed views. Although n_{clr} does not directly correlate to e_d as $v_{t,m}$ does, a minimum n_{clr} of around 11 is required to access cases with much lower e_d and $n_{vio,a}$ of less than 11.	80
3.13	Relationships between control setting n_{clr} and resulting n_{adj} for LTCs and CBs. Increased n_{clr} correlates to increased mean and variance of n_{adj} for LTCs and CBs. For designs with greater than 60 CB n_{adj} , CB unavailability is observed due to more frequent timer activation. . . .	81
3.14	Resulting $n_{vio,a}$, e_d , and n_{adj} from different input control setting combinations of n_{clr} and $v_{t,m}$ for the 409 designs with less than or equal to 10 $n_{vio,a}$ along with the calculated Pareto front of 8 best designs and selected case.	84
3.15	Comparison of control methodologies for KUs1T1 by individual bus voltages every simulation timestep, including the cases of conventional (top left), optimal with unlimited adjustments (top right), and improved cluster-based optimal that has limited adjustments with both example (bottom left) and best control settings (bottom right).	86
4.1	Residential energy use survey results for 2015 provided by the U.S. Energy Information Administration. Provided are (a) annual energy use by different appliances of a typical residential building in the U.S. and (b) end-user energy use distribution by different types of U.S. homes. Energy use excludes the losses in electricity generation and delivery.	90
4.2	Typical operation schedule through energy use for (a) a refrigerator (Ref) and (b) clothes washer (CW) of a 3 bedroom, 2.5 bathroom house based on the Building America house simulation protocols. . . .	92
4.3	The near net-zero-energy (NNZE) house front (a) and back (b). TVA robotic devices are controlled to mimic realistic human behavior. Also shown is a HPWH used in the retrofit house (c), a shower emulator (d), and a refrigerator with programmed arms (e) that operate according to automatic schedules.	94
4.4	Example BEopt simulation model for the typical construction house type. All models follow a very similar floor plan but different construction materials and techniques.	94

4.5	The overall system architecture of EnergyPlus, an open source whole building energy simulation program that models energy use for both HVAC system and plug and process loads.	95
4.6	Hourly energy usage for the HVAC system of the simulated conventional house (a) and the hourly energy difference between the HVAC systems of the conventional house and the NNZE house (b) based on Knoxville, TN TMY3 weather data.	100
4.7	Power for the HVAC systems in the Conv13S and Conv19S models. Both were simulated using Knoxville TN, TMY3 weather data on an example summer day.	101
4.8	HVAC system power for a high energy use, heating-only February day and a low energy use day in May with a mixture of heating and cooling.	102
4.9	Total actual measured energy usage of the HVACs, WHs, lights, Miscellaneous Electric Load (MEL), and appliances (Apps) within the conventional and retrofit houses for the year of 2010. The HVAC is consistently the highest individual energy user, while the water heater is always the second highest.	104
4.10	Example week for the electric water heater (EWH) schedule.	104
4.11	Power for the conventional house EWH and the retrofit house HPWH during an example day in 2010.	105
4.12	Example daily PV power for the typical case of very low daily energy error and the rare case of higher error which is likely due to differing solar radiation between the irradiance sensor and actual PV panel. . .	108
4.13	Monthly total PV generation for TN1 (Knoxville, TN), TN2 (Memphis, TN), and KY (Bowling Green, KY) locations.	109
4.14	Hourly PV energy generation of the simulated 2.5kW PV system in Memphis, TN (a) and the hourly energy difference between system simulations in Memphis, TN and Bowling Green, KY (b). All simulations were based on TMY3 weather data.	110
4.15	Overview of the system losses (grid and building level) caused by low PF of the typical residential home appliances. The upstream losses of the distribution transformers are not shown.	112
4.16	Real examples of voltage and current waveforms for (top) a vacuum cleaner and (bottom) DC power supply illustrating the influence of harmonic distortion on PF.	112
4.17	Real and reactive power during example operation cycles of (a) a typical HVAC system as well as (b) a refrigerator and a clothes washer based on experimental data.	115
4.18	Experimental minutely PF and calculated equivalent PF for 15-minute interval, which corresponds to typical smart metering, and the traditional hourly interval for (a) an HVAC system, (b) a refrigerator, and (c) a clothes washer (CW).	117

5.1	Schematic illustration of the newly developed co-simulation framework with multiple HVAC and building models and CTA-2045 control implementation. The framework employs ultra-fast HVAC system and building models with distinct base load energy profiles for typically human behavior-based loads. A representative community of individually unique building models for both electric power and indoor temperature may be simulated at the buildings and power system levels. It may also incorporate other DER types with controls, such as solar PV and BESSs.	121
5.2	Histograms of HVAC cooling characteristics associated with the 351 synthesized EnergyPlus models from which the ML models were trained.	126
5.3	Histograms of HVAC heating characteristics associated with the 351 synthesized EnergyPlus models from which the ML models were trained.	127
5.4	Histograms of conductivity values for different construction materials of the 351 synthesized EnergyPlus models from which the ML models were trained.	128
5.5	Histograms of thickness and density values for different construction materials as well as window efficiency metrics of the 351 synthesized EnergyPlus models from which the ML models were trained.	129
5.6	Schematic of HVAC and building time dependent simulator capable of executing both explicit and CTA-2045 commands, as well as providing Energy Star GES performance, such as electric energy capacity, energy take, and equivalent SOC.	130
5.7	Flowchart for the HVAC and building simulator that employs ML HVAC models as well as the PV simulator.	131
5.8	The circuit diagram for the modified IEEE 123-bus test system. The original circuit has a peak load of 3.6MW, 1.3MVA and is to be representative of a very large residential subdivision in the U.S.	133
5.9	PDS total active power for the baseline and control cases. This is an aggregation of all building loads minus the power losses across the PDS without considering any contributions from PV generation.	133
5.10	Results for the PDS total solar PV power generation for the simulated 15% and estimated solar PV penetration cases of up to 100%. The variability in solar PV power generation is caused by variability in irradiance.	135
5.11	Results for the PDS total net power for the simulated 15% and estimated solar PV penetration cases of up to 100%.	135
5.12	Simulation results for individual on/off statuses for HVACs to show control phasing in the baseline case (top) and in case P6 (bottom) for both the baseline and P6 cases. The “load-up” and “shed” event windows are shaded in light gray and purple, respectively. This format is replicated in following figures.	138
5.13	Simulation results hourly average PDS bus voltages for both the baseline and P6 cases.	138

5.14	Resulting evaluation of optimization objectives for both the central composite (CC) and full factorial (FF) DOEs with respect to the baseline case.	140
5.15	Response surfaces for the central composite (left) and full factorial (right) DOEs that captures the relationships between input control time settings and the objectives.	141
5.16	Four dimensional representations of the objective evaluations for the optimization results, which include over 750 designs.	141
5.17	Resulting (top) objective evaluations and (bottom) a cropped view of all cases simulated during the NSGA-III optimization with respect to the baseline case and with the Pareto front of the eleven (11) best cases indicated.	142
5.18	Relationships between the two (2) objectives and the three (3) independent variables of control times for all simulated cases during the optimization.	144
5.19	Total energy use for the baseline and P6 cases.	148
5.20	HVAC energy use only for the baseline and P6 cases.	149
5.21	Hourly average indoor temperatures of all buildings for the baseline and P6 cases.	149
5.22	Hourly equivalent SOC, which is inversely related to indoor temperature, of all buildings for the baseline and P6 cases.	150

Chapter 1

Introduction

1.1 Background

Improved performance of electric Power Distribution Systems (PDSs) through optimal planning and operation of conventionally available voltage-controlling devices can offer significant savings in both energy and investment. Such devices include capacitor banks (CBs), which are typically employed to increase system load capacity, reduce losses and improve power factor through voltage drop counteraction along a circuit by providing reactive power. They have long been considered a popular technology due to their lower cost and maintenance requirements when compared to other reactive power compensating devices and methods.

Traditionally, the CB installation process is performed through “rule-of-thumb” simulation techniques with the assumption of peak load operation since this scenario represents the most extreme condition of the circuit and the best opportunity for savings. The yielded benefits of CBs are directly determined by both their placement and rating [2]. Therefore, the application of optimal CB placement and rating can improve savings and system performance. Such optimization is typically multi-objective in nature since costs from system power losses, capital investment, and voltage quality may compete.

Conventional control of PDSs over time is achieved through Supervisory Control and Data Acquisition (SCADA) networks and compatible devices, such as switchable CBs, automatic voltage regulators (AVRs), and Load-Tap-Changing (LTC) transformers [1]. The improved control and management of these devices are also currently of great interest for grid modernization and are typically associated with the concepts of Conservation Voltage Reduction (CVR) and Volt-Var Optimization (VVO) [3]. CVR has long been considered as a function of VVO to cost-effectively reduce energy use and peak power [4].

Techniques for optimal PDS planning may also be adapted for optimal operation and control that employ CVR and VVO functions. Through time-series simulation and computational optimization, total energy use, voltage quality, and utility asset degradation may be improved. Relevant optimization objectives may include total energy use and targeted peak power reduction by either minimizing losses or demand through adjusting system-wide voltage. The degree of benefit from either minimization is dependent upon circuit-specific voltage dependency of associated loads.

Various utility and national laboratory demonstrations of CVR and VVO have been performed through pilot programs and test cases of differing M&V types [5]. It has been determined based on such field implementations that PDS energy use may be reduced by 0.3% to 1.0% for every 1% of reduction in system voltage [6]. A range of 1% to 4% in total energy use savings is expected based upon circuit-specific characteristics. Therefore, as smart grid technologies and Advanced Meter Infrastructure (AMI) become increasingly more prevalent in modern distribution systems, the improved control of these devices offers significant opportunity for savings in both

energy use and costs due to equipment degradation.

Emerging smart technologies can provide visibility and control of individual residential loads in buildings as well. Various energy-using appliances constitute a smart building, including larger energy users like Heating, Ventilation, and Air-Conditioning (HVAC) and water heating systems. Such appliances can reduce energy use of residential loads through considerable efficiency improvements and may be employed as Distributed Energy Resources (DERs) for residential energy storage and load manipulation.

Load manipulation, especially for electric PDSs with highly variable distribution-side generators such as solar Photo-Voltaic (PV) systems, can be an invaluable tool for utilities in managing the smart grid and for improved renewable integration and local utilization. Co-simulation frameworks of DER and PDS models as testbeds enable study and development of such Virtual Power Plant (VPP) methodologies.

1.2 Literature Review

The following is a brief introductory literature review for each of the chapters. Additional literature review is included in the corresponding introductory sections.

For current PDSs, various optimization approaches have been applied in literature to the CB placement and sizing problem with differing considerations of objectives and independent variables. Some techniques include plant growth-based and multi-objective Particle Swarm Optimization (PSO) algorithms [7–12]. Additional reported methods involve the hybrid utilization of multi-criteria algorithms at different levels with comparisons of algorithm types [13–17].

It was found that typical objectives for CB planning generally include the minimization of active power losses and investment [18–20]. Constraints were also sometimes applied concurrently with the optimization, or afterward upon the resulting Pareto set, to ensure power system operational compliance for proposed CB configurations by limiting voltage violations and Total Harmonic Distortion (THD) [20–22].

A literature gap exists with respect to the consideration or evaluation of CB efficacy over time as well as for application on real large-scale PDSs, as the studied methods usually employed the IEEE test systems at their peak load instances. PDSs can experience considerable change in load demand and bus voltages due to natural loadshapes and operational events of typical control devices, such as LTC transformers and voltage regulators [23–25]. The readjustment of such devices upon reconfiguration of CBs during the optimization process also seems to be insufficiently reported.

The evaluation of CVR and VVO effects may be performed through measurement and verification (M&V) methods that should consider load effects from typical causes, such as weather, time of day, and occupant behavior. Such M&V methods may be categorized as comparison, regression, or simulation-based [5, 26]. Simulation-based methods employ power system models that enable simulated control of components with the challenge of considering load changes over time and voltage-dependency, which can be captured through constant impedance, constant current, and constant power (ZIP) modeling [23, 24, 27].

The U.S. residential sector is a major participant in the electric power grid at nearly 25% of the total energy demand [28]. U.S. residences, regardless of building type or geographical location, typically contain various appliances, many of which are

becoming controllable devices in the emerging smart grid. Based on a survey of end user energy consumption, space heating and cooling are the top categories in energy use among typical household appliances [29]. Combined, they may be considered as a complete HVAC system and use over 50% of total annual residential energy [30–32]. Therefore, the application of VPP control for HVAC systems, in aggregate, offers a significant opportunity for the shift or reduction of load peaks in power systems [33].

Simulation testbeds are reported to have an important role in both the development of VPP control schemes and in the planning of DER deployment [34]. Battery Energy Storage Systems (BESSs) can be an effective, but costly, utility grid energy management solution and, therefore, are typically optimally planned through distribution system simulation [35]. Control strategies that coordinate multiple types of DERs, such as BESSs and solar PV, are an integral aspect of the smart grid which can be developed and tested through simulation [36].

1.3 Research Objectives and Original Contributions

Research Objectives

The study of optimal planning and operation for PDSs is a main research objective of this work. Recent improvements in modeling, measurement, and control offers considerable opportunity in this regard. Currently available large-scale PDS models are employed by utilities for general planning purposes and may be converted into an open-source version with custom reformatting software for the development and study of control and optimization methodologies.

The combination of these highly inter-operable model versions and computational

intelligence methods allows for the optimization of both CB placement and rating in actual many thousand-node utility PDSs at their static peak load case, which offers the most opportunity for savings. Measured circuit data enables time series simulation with the assumption that individual loads experience the same loadshape and may be scaled accordingly to match that of the total circuit load measured at the source bus. Increasingly available AMI data offers the prospect of individually unique load profiles and increased simulation granularity in the near future.

With time-series simulation capability, methods employed in optimal planning may also be adapted for optimal operation and control. Typically available devices, such as switchable CBs and controllable LTC transformers, may be utilized to minimize total system power and to improve its voltage-time profile. Power demand reduction is achieved through the decrement of LTC tap settings, while considering violations of the standard tolerance at all buses, to decrease voltage-dependent load demand. Voltage-dependency is captured by an equivalent ZIP load modeling method that employs available measured data for a specific circuit. Power losses are also reduced through optimal operation of CBs to maintain voltage near relatively high-loss buses. Such optimal performance, though, is likely to increase device operation frequency, which may cause faster equipment degradation and is also to be considered.

For the utilization of typical residential loads as DERs in power systems, consideration of various appliance-specific dependencies is necessary to develop adequate models. As the largest energy-using household appliance with the most opportunity as a controllable DER, HVAC systems are of significant focus. The modeling of HVAC

systems must capture both weather effects and the building thermal properties with which it is associated. Furthermore, control effects on occupant thermal comfort must also be considered as they represent a constraint in realistic scenarios. Other appliances are not as dominantly weather-dependent and can be modeled based on use schedules that represent typical human behavior.

In order to study large-scale VPP control strategies that employ such residential loads, their models must be highly inter-operable in a co-simulation framework with PDSs. Current building energy modeling methods are typically of the white-box, physics-based nature and require considerable computation time, which limits scalability. Computational and artificial intelligence methods offer solutions to such limitations and enable large-scale case studies. The characterization of residential loads as Generalized Energy Storage (GES) also enables uniform control methods for all localized DER. Through such developments, applications of VPP controls for peak power manipulation and the study of corresponding effects at both the power system and individual building levels are of great interest.

Original Contributions

1. A comparative study of multi-objective optimization approaches for a power system specific problem that employ computational intelligence methods, such as Differential Evolution (DE) and the Non-Dominated Sorting Genetic Algorithm (NSGA) III, as applied to three real large-scale utility circuits.
2. A new multi-step procedure for optimal power system configuration selection that utilizes pseudo weight vectors based on objective priority and a systematic

analysis of the most extreme configuration types.

3. An efficacy evaluation approach for power system configurations through time-series simulation and stochastic analysis.
4. Optimal operation of PDSs through CB and LTC transformer control that minimizes total system energy use and improves its voltage-time profile.
5. A cluster-based method to optimally disperse PDS device control adjustments over time through load-forecasting in order to minimize utility asset degradation and maintain best performance.
6. Development of EnergyPlus models through extensive multi-annual data from experimental homes with robot-operated appliances to mimic human habitation that represent different levels of energy efficiency for U.S. houses.
7. Development and demonstration of a highly scalable co-simulation framework for ultra-fast machine learning models of building electric power and indoor temperature with actual many-thousand node PDSs.
8. Simulation and analysis of VPP scenarios that employ hundreds of unique buildings and their corresponding HVAC systems with other DER, such as local solar PV, through GES characterization and Consumer Technology Association (CTA) 2045 control schemes.
9. Multi-objective optimization of VPP HVAC control considering peak power reduction in exchange for increased total energy use through control timing.

1.4 Dissertation Outline

Following the introduction, Chapter 2 proposes a multi-objective optimal planning method for PDS CBs with procedures for configuration selection and efficacy evaluation over time. Chapter 3 discusses the optimal operation of conventional PDS devices, such as CBs and LTC transformers, through machine learning clustering and load-forecasting. Chapter 4 explores the energy effects of smart building technologies and discusses the modeling of robot-operated smart homes, which enables evaluation in different geographical locations and utilization in DER control schemes. As an application and continuation of study from the previous chapters, the co-simulation framework for the building models in Chapter 4 with the PDS simulation testbed from Chapters 2 and 3 is provided in Chapter 5 . Also included in Chapter 5 are studies of VPP scenarios that employ HVAC systems as energy storage in coordination with other DERs through GES characterizations and control setting optimization. Finally, conclusions and recommendations for continued and future work are provided in Chapter 5.7.

1.5 Main Publications

The main concepts, methods, and results of this dissertation have been published or under consideration for publication in the following journal and conference proceeding papers:

- **E. S. Jones**, N. Jewell, Y. Liao, and D. M. Ionel, “Optimal Capacitor Placement and Rating for Large-Scale Utility Power Distribution Systems Employing Load-Tap-Changing Transformer Control,” *IEEE Access*, vol. 11, pp. 19324-19338, 2023, doi: 10.1109/ACCESS.2023.3244572.

- **E. S. Jones**, R. E. Alden, H. Gong, and D. M. Ionel, “Co-simulation of Electric Power Distribution Systems and Buildings including Ultra-fast HVAC Models and Optimal DER Control,” 14p, *prepared for journal submission (April 2023)*.
- **E. S. Jones**, N. Jewell, Y. Liao, and D. M. Ionel, “A Cluster-based Method for Optimal Operation of Power Distribution Systems with Minimal Utility Asset Degradation,” 10p, *prepared for journal submission (April 2023)*.
- **E. S. Jones**, R. E. Alden, H. Gong, A. Hadi, and D. M. Ionel, “Co-simulation of Smart Grids and Homes including Ultra-fast HVAC Models with CTA-2045 Control and Consideration of Thermal Comfort,” 2022 IEEE Energy Conversion Congress and Exposition (ECCE), Detroit, MI, USA, 2022, pp. 1-6, doi: 10.1109/ECCE50734.2022.9948200.
- **E. S. Jones**, R. E. Alden, H. Gong, A. G. Frye, D. Colliver and D. M. Ionel, “The Effect of High Efficiency Building Technologies and PV Generation on the Energy Profiles for Typical US Residences,” 2020 9th International Conference on Renewable Energy Research and Application (ICRERA), 2020, pp. 471-476, doi: 10.1109/ICRERA49962.2020.9242665.
- R. E. Alden, **E. S. Jones**, S. B. Poore, H. Gong, A. Al Hadi and D. M. Ionel, “Digital Twin for HVAC Load and Energy Storage based on a Hybrid ML Model with CTA-2045 Controls Capability,” 2022 IEEE Energy Conversion Congress and Exposition (ECCE), Detroit, MI, USA, 2022, pp. 1-5, doi: 10.1109/ECCE50734.2022.9948141.
- H. Gong, **E. S. Jones**, A. H. M. Jakaria, A. Huque, A. Renjit and D. M. Ionel, “Large-Scale Modeling and DR Control of Electric Water Heaters With Energy Star and CTA-2045 Control Types in Distribution Power Systems,” in IEEE Transactions on Industry Applications, vol. 58, no. 4, pp. 5136-5147, July-Aug. 2022, doi: 10.1109/TIA.2022.3178066.
- H. Gong, **E. S. Jones**, R. E. Alden, A. G. Frye, D. Colliver and D. M. Ionel, “Virtual Power Plant Control for Large Residential Communities Using HVAC Systems for Energy Storage,” in IEEE Transactions on Industry Applications, vol. 58, no. 1, pp. 622-633, Jan.-Feb. 2022, doi: 10.1109/TIA.2021.3120971.

Additional peer-reviewed journal and conference proceedings papers have been published and are listed in the following:

- **E. S. Jones**, O. M. Akeyo, K. Waters and D. M. Ionel, “Electric Power System Studies for a Multi-MW PV Farm and Large Rural Community with Net Zero Energy and Microgrid Capabilities” 2020 IEEE Industry Applications Society Annual Meeting, Detroit, MI, USA, 2020, pp. 1-4, doi: 10.1109/IAS44978.2020.9334740.

- **E. S. Jones**, H. Gong and D. M. Ionel, “Optimal Combinations of Utility Level Renewable Generators for a Net Zero Energy Microgrid Considering Different Utility Charge Rates,” 2019 8th International Conference on Renewable Energy Research and Applications (ICRERA), Brasov, Romania, 2019, pp. 1014-1017, doi: 10.1109/ICRERA47325.2019.8996529.
- D. D. Lewis, A. Patrick, **E. S. Jones**, R. E. Alden, A. Hadi, M. D. McCulloch, and D. M. Ionel, “Decarbonization Analysis for Thermal Generation and Regionally Integrated Large-Scale Renewables Based on Minutely Optimal Dispatch with a Kentucky Case Study,” *Energies*, Vol. 16, No. 4, 1999, doi:10.3390/en16041999, 23p (2023)
- Y. Zhang, Y. Liao, **E. S. Jones**, N. Jewell and D. M. Ionel, “ZIP load modeling for single and aggregate loads and CVR factor estimation,” in *International Journal of Emerging Electric Power Systems*, vol. 23, pp. 839-858, 2022, doi: 10.1515/ijeeps-2022-0052.
- R. E. Alden, H. Gong, **E. S. Jones**, C. Ababei and D. M. Ionel, “Artificial Intelligence Method for the Forecast and Separation of Total and HVAC Loads With Application to Energy Management of Smart and NZE Homes,” in *IEEE Access*, vol. 9, pp. 160497-160509, 2021, doi: 10.1109/ACCESS.2021.3129172.
- H. Gong, **E. S. Jones**, A. H. M. Jakaria, A. Huque, A. Renjit and D. M. Ionel, “Generalized Energy Storage Model-In-the-Loop Suitable for Energy Star and CTA-2045 Control Types,” 2021 IEEE Energy Conversion Congress and Exposition (ECCE), Vancouver, BC, Canada, 2021, pp. 814-818, doi: 10.1109/ECCE47101.2021.9595892.
- H. C. Anderson, A. Al Hadi, **E. S. Jones** and D. M. Ionel, “Power Factor and Reactive Power in US Residences – Survey and EnergyPlus Modeling,” 2021 10th International Conference on Renewable Energy Research and Application (ICRERA), Istanbul, Turkey, 2021, pp. 418-422, doi: 10.1109/ICRERA52334.2021.9598561.
- Y. Zhang, Y. Liao, **E. S. Jones**, N. Jewell and D. M. Ionel, “Kalman Filter Based Approach for ZIP Load Modeling for Aggregate Loads,” 2021 IEEE Kansas Power and Energy Conference (KPEC), Manhattan, KS, USA, 2021, pp. 1-6, doi: 10.1109/KPEC51835.2021.9446202.
- H. Gong, **E. S. Jones**, R. E. Alden, A. G. Frye, D. Colliver and D. M. Ionel, “Demand Response of HVACs in Large Residential Communities Based on Experimental Developments,” 2020 IEEE Energy Conversion Congress and Exposition (ECCE), Detroit, MI, USA, 2020, pp. 4545-4548, doi: 10.1109/ECCE44975.2020.9235465.
- H. Gong, **E. S. Jones** and D. M. Ionel, “An Aggregated and Equivalent

Home Model for Power System Studies with Examples of Building Insulation and HVAC Control Improvements,” 2020 IEEE Power & Energy Society General Meeting (PESGM), Montreal, QC, Canada, 2020, pp. 1-4, doi: 10.1109/PESGM41954.2020.9281438.

Chapter 2

Planning and Optimization for Electric Power Distribution Systems

2.1 Introduction and Main Problem

Capacitor banks (CBs) are typically employed in power distribution systems to increase system load capacity and overall power factor correction. This is achieved by providing voltage support and reactive power control functions, which also yields improved power losses and energy savings. Resulting harmonic effects and switching transients from control over time are considered secondary to these main benefits.

CBs have long been considered a popular technology due to their lower cost and maintenance requirements when compared to other reactive power compensating devices. The traditional and currently most common method for CB installation relies on intuitive rules of thumb supported by multiple powerflow studies to manually determine location and reactive power rating [1, 37]. Such techniques can be arduous to perform and likely to provide sub-optimal solutions, especially for larger power distribution systems.

The yielded benefits of CBs are directly determined by both their placement and rating [2]. Therefore, the application of an Optimal CB Planning (OCP) procedure, such as the one proposed in this work and illustrated in Fig. 2.1, offers the opportunity

for improved savings and system performance. Such optimization is typically multi-objective in nature since costs from system power losses, capital investment, and voltage quality may compete.

A comparative study of multi-objective CB planning methods is presented, which includes novel approaches that may employ three concurrent objectives, a penalty constraint upon voltage violations during optimization, and the automatic adjustment of Load-Tap-Changing (LTC) transformer tap settings to ensure peak system performance based upon proposed CB re-configurations. For the optimization algorithm, multi-objective versions of differential evolution (DE) and a Genetic Algorithm (GA) are considered and compared in performance and Pareto set quality.

Optimal CB installation bus locations and ratings are simultaneously determined for three sub-circuits corresponding to transformers of a substation within a large 48MW, 9Mvar example power distribution system, which is made possible through an automated model conversion procedure of actual large-scale utility distribution systems. The circuits are simulated at their peak loads since this scenario represents the most extreme condition of the circuit and the best opportunity for savings. Maximum load demand causes minimum voltage, and the most need is experienced for voltage support and reactive power compensation. With CBs being switchable and becoming more easily controllable, those having been installed may be turned off for lower load situations to maintain operational compliance.

An initial sensitivity analysis is employed to improve computation time and maintain Pareto set quality, as the example real circuit is very large in scale with approximately 4,000 buses, which is a major contribution. A pseudo-weight vector approach

is utilized to select optimal configurations based on provided weights, including the most extreme cases with respect to the considered objectives. A systematic procedure is proposed to analyze the extreme and existing reference configurations for each sub-circuit to inform configuration selection from among the corresponding Pareto sets.

The main objective of the work described in this chapter is to improve operation through the optimal placement and rating of CBs in power distribution systems. Independent variables are identified and include CB rating at the most sensitive bus locations. Different studies involve various combinations of objectives, which include minimization of power losses, voltage standard deviation, and investment.

This chapter is substantially based on the following journal publication: **E. S. Jones**, *et al.*, “Optimal Capacitor Placement and Rating for Large-Scale Utility Power Distribution Systems Employing Load-Tap-Changing Transformer Control,” *IEEE Access*, vol. 11, pp. 19324-19338, 2023, doi: 10.1109/ACCESS.2023.3244572.

In section 2.2, a literature review is provided with primary focus upon existing CB planning methods that employ computational optimization. Section 2.4 establishes the power distribution system modeling and simulation procedure. Section 2.5 formulates the CB planning problem and provides the sensitivity analysis for bus location installation candidacy, which corresponds to optimization decision variables. Considered optimization algorithms are explained in section 2.6, and the methods which employ them are compared in section 2.7 to establish their individual merits. Finally, a sub-circuit analysis to inform configuration selection is provided in section 2.8 with conclusions in section 2.10.

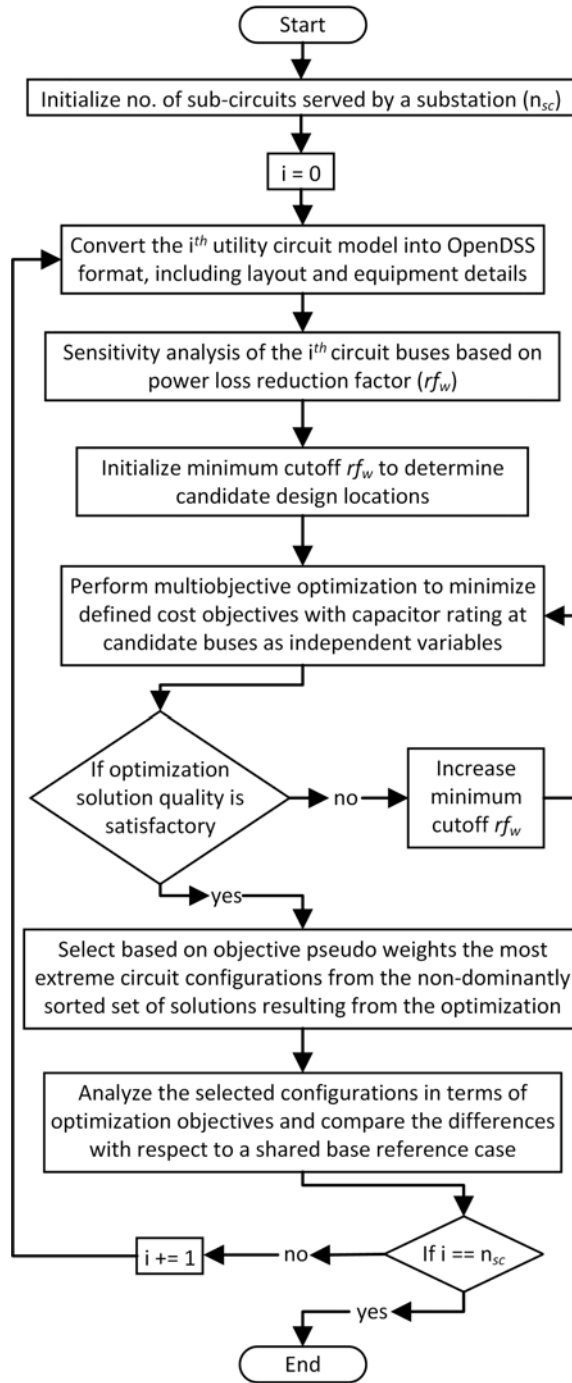


Figure 2.1: Flowchart for the overall proposed OCP procedure with five main processes, including circuit modeling, candidate bus location determination, multi-objective optimization, solution selection considering objective priority, and selected configuration analysis.

2.2 Conventional Approaches

Upon review of relevant literature, special attention was placed on the selection of optimization objectives and algorithms employed in such studies. Additional constraints and the stage during which they were applied were also considered as well as example test power systems and modeling methods for both the networks and loads.

Proposed by A. Noori *et al.* is a hybrid allocation of CBs and distributed static compensators in power distribution systems through multi-objective improved golden ratio optimization method (MOIGROM) and a fuzzy decision making process [18]. In this case, the MOIGROM has two objectives, including voltage violations and total installation cost corresponding to the equipment and related active power losses. A power loss reduction factor method is applied to determine buses most sensitive to reactive resource installation to reduce the decision variables considered by the MOIGROM. The procedure was applied to the IEEE 13, 69, and 118 bus test systems, resulting in solutions that improved both total active power losses and voltage violations on the example circuits.

Two optimal methodologies that both employ an epsilon multi-objective genetic algorithm (ϵ -MOGA) for the allocation of both fixed and switching CBs in a simulated real utility 162-bus power distribution network are explored by M. Ahmadi *et al.* [19]. Optimization objectives include minimization of total installation cost and switching frequency. The first method is a two-step process where installation location is determined by sensitivity analysis and the CB sizes by ϵ -MOGA, whereas the second method utilizes ϵ -MOGA for both. The two-mechanism approach with

an additional sensitivity analysis yielded better results, but both methods showed significant improvement in voltage profile, power losses, and financial investment.

Post-optimization constraints may also be applied as employed by Onaka *et al.* for the IEEE 34-bus test system to consider total harmonic distortion (THD) [21]. Optimal solutions are determined initially through the Non-Dominated Sorting Genetic Algorithm II (NSGA-II) for two objectives in which the maximum bus voltage violations and total system costs considering CB installation as well as active power losses at both fundamental and harmonic frequencies are to be minimized. Solutions among the Pareto set, or optimal solution set of best compromise, that violate the THD constraint are removed from consideration.

Optimal placement and sizing of CBs is determined by A. A. Eajal *et al.* for the IEEE 13-bus test system through a discrete Particle Swarm Optimization (PSO) with a single objective of minimizing total system cost considering active power losses and CB installation [20]. A total Harmonic Distortion (THD) constraint is applied during the optimization instead of in the post-optimization stage as in [21].

An ant colony search optimization algorithm is proposed by C. F. Chang for both network reconfiguration and CB placement with the minimization of power losses as the only objective [22]. Voltage quality and other operating conditions are considered as constraints. It is also proposed that the method could be extended to automated control of distribution system devices over time.

Other optimization approaches have been applied to this CB placement and sizing problem, such as plant growth-based and multi-objective PSO or NSGA-II algorithms with differing objectives [7–12, 38, 39]. Some reported methods involve the hybrid

utilization of different multi-criteria algorithms at different levels of a power system simulation, and comparisons of algorithm types have been provided [13–17].

It was found that typical objectives for CB planning generally include the minimization of active power losses and investment [18–20]. Constraints were also sometimes applied concurrently with the optimization or afterward upon the resulting Pareto set to ensure power system operational compliance for proposed CB configurations by limiting voltage violations and THD [20–22, 39].

The reconfiguration of other circuit elements to accommodate new CB arrangements has also been considered in literature, including by system topology alterations through changes in tie states and sectionalizing switches [40, 41]. Other studies have incorporated Distributed Generators (DGs) with their CB planning approaches, as renewable DGs like local solar PV are becoming more prevalent in modern power distribution systems [42–45].

Optimal CB planning for circuits with different load model scenarios have been studied [41, 46–48]. Such scenarios include different percentages of the peak load, variation in load based on customer types, or cases that model load voltage dependency. To study such cases on larger utility circuits, there is a need for enhanced load modeling methods with improved granularity, such as those that may employ data from Advanced Metering Infrastructure (AMI) programs currently being deployed by utilities [49].

In addition to natural loadshapes, power distribution systems can experience considerable change in load demand and bus voltages due to operational events of typical control devices, such as LTC transformers and voltage regulators. A literature gap

exists with respect to the readjustment of such devices upon reconfiguration of CBs during the optimization process. LTC settings control the voltage profile of a power system and must be considered for a fair comparison to a base reference case.

Although comparative studies of optimization algorithms for OCP methods are available in current literature, the direct comparison of different methods in full, including their formulations, are insufficiently reported. The consideration or evaluation of CB efficacy over time as well as application of OCP on real large-scale power distribution systems are both limited in literature, as current studies usually only employ the IEEE test systems at their peak load instances.

The original contributions of this work are framed within the development and proposal of a novel OCP procedure (Fig. 2.1). These include a comparative study of multi-objective optimization approaches for a power system specific problem by employing computational intelligence methods and readjustment of LTC transformers, a new multi-step procedure for optimal power system configuration selection that utilizes a pseudo weight vector approach based on objective priority and a systematic analysis of the most extreme configuration types, and the application of OCP to three actual large-scale utility circuits, which was achieved through a custom-developed software to translate utility distribution system models into open-source OpenDSS versions for considerably improved accessibility.

2.3 Electric Power Distribution System Modeling

The modeling of PDSs may be achieved through the determination of power flow and associated values at all defined nodes, which include real power (P), reactive

power (Q), voltage magnitude ($|V|$), voltage phase angle (σ), and current (I) [50].

The apparent power at node i may be defined by:

$$S_i = P_i + jQ_i = V_i I_i^*. \quad (2.1)$$

For a power system with n nodes, the network equation is given by the matrix equation:

$$\mathbf{I} = \mathbf{Y}\mathbf{V}, \quad (2.2)$$

where \mathbf{I} is n vectors of current injections; \mathbf{Y} , $n \times n$ bus admittance matrix; \mathbf{V} , n vectors of node voltages.

The current injected into node i may be obtained from 2.2:

$$I_i = \sum_{k=1}^n Y_{ik} V_k = Y_{i1} V_1 + Y_{i2} V_2 + \dots + Y_{in} V_n. \quad (2.3)$$

Solving 2.3 and 2.1 provides:

$$S_i = P_i + jQ_i = \sum_{k=1}^n V_i V_{ik}^* V_k^*, \quad (2.4)$$

By rewriting $V_k = |V_k| \angle \delta_k$, $Y_{ik} = |Y_{ik}| \angle \theta_{ik}$, 2.4 becomes:

$$S_i = \sum_{k=1}^n |V_i| \angle \delta_i |Y_{ik}| \angle -\theta_{ik} |V_k| \angle -\delta_k = |V_i| |Y_{ik}| |V_k| \angle \delta_i - \theta_{ik} - \delta_k. \quad (2.5)$$

The real and reactive power at node i can determined by:

$$P_i = \text{Re}(S_i) = \sum_{k=1}^n |V_i| |Y_{ik}| |V_k| \cos(\delta_i - \theta_{ik} - \delta_k) \quad (2.6)$$

$$Q_i = \text{Im}(S_i) = \sum_{k=1}^n |V_i| |Y_{ik}| |V_k| \sin(\delta_i - \theta_{ik} - \delta_k) \quad (2.7)$$

The power at the nodes of network consisting of n buses from 2.4 is described by:

$$\begin{aligned} S_i &= P_i + jQ_i = \sum_{k=1}^n V_i Y_{ik}^* V_k^* \\ &= V_i Y_{ii}^* V_i^* + V_i \sum_{k=1, k \neq i}^n Y_{ik}^* V_k^*, \quad i = 1, 2, \dots, n \end{aligned} \quad (2.8)$$

Rewriting 2.8:

$$Y_{ii}^* V_i^* = \frac{S_i}{V_i} - \sum_{k=1, k \neq i}^n Y_{ik}^* V_k^* \quad i = 1, 2, \dots, n \quad (2.9)$$

Dividing both sides of 2.8 by Y_{ii}^* :

$$V_i^* = \frac{1}{Y_{ii}^*} \left[\frac{S_i}{V_i} - \sum_{k=1, k \neq i}^n Y_{ik}^* V_k^* \right] \quad i = 1, 2, \dots, n \quad (2.10)$$

The complex conjugate of 2.10 is solved as:

$$V_i = \frac{1}{Y_{ii}} \left[\frac{S_i^*}{V_i^*} - \sum_{k=1, k \neq i}^n Y_{ik} V_k \right] \quad i = 1, 2, \dots, n \quad (2.11)$$

OpenDSS, an open-source software by the Electric Power Research Institute (EPRI) for the modeling of electric power distribution systems, employs the primitive admittance matrix approach. A two-phased coupled impedance example may be defined as:

$$\begin{bmatrix} I_1 \\ I_2 \\ I_3 \\ I_4 \end{bmatrix} = \begin{bmatrix} Z^{-1} & -Z^{-1} \\ -Z^{-1} & Z^{-1} \end{bmatrix} \begin{bmatrix} V_1 \\ V_2 \\ V_3 \\ V_4 \end{bmatrix}, \quad (2.12)$$

where the impedance characteristics, Z , are defined as:

$$Z = \begin{bmatrix} z_{11} & M_{12} \\ M_{12} & z_{22} \end{bmatrix} \quad (2.13)$$

In OpenDSS, power lines are defined by impedance matrix. For a three phase bus example, impedance matrices may be represented by:

$$Z = R + jX = \begin{bmatrix} Z_{11} & Z_{12} & Z_{13} \\ Z_{21} & Z_{22} & Z_{23} \\ Z_{31} & Z_{32} & Z_{33} \end{bmatrix} \quad (2.14)$$

The series resistance and reactance matrices are respectively defined in ohms per unit length:

$$R = \begin{bmatrix} R_{11} & & \\ R_{21} & R_{22} & \\ R_{31} & R_{32} & R_{33} \end{bmatrix}, \quad (2.15)$$

$$X = \begin{bmatrix} X_{11} & & \\ X_{21} & X_{22} & \\ X_{31} & X_{32} & X_{33} \end{bmatrix}. \quad (2.16)$$

The shunt nodal capacitance matrix is defined in nanofarads per unit length:

$$C = \begin{bmatrix} C_{11} & & \\ C_{21} & C_{22} & \\ C_{31} & C_{32} & C_{33} \end{bmatrix}. \quad (2.17)$$

Power flow of circuit models is solved in OpenDSS by iterative loop. The main system admittance matrix is constructed by the small nodal admittance matrices of each line. The source currents and node voltages are updated at each iteration until it converges based on a provided tolerance, which is typically 0.0001p.u.

Ohm's Law for the main system admittance matrix may be expressed as:

$$\mathbf{I}_s = \mathbf{YV}, \quad (2.18)$$

where \mathbf{I}_s is the source currents; \mathbf{V} , the node voltages. OpenDSS adopts the "flat start" method where all voltage angles and magnitudes are initialized to 0 and 1.0p.u., respectively. For each iteration, \mathbf{V} is calculated by the sparse matrix solver, denoted by:

$$V_i^{(k+1)} = \frac{1}{Y_{ii}} (I_{si} - \sum_{j \neq i} Y_{ij} V_j^k). \quad (2.19)$$

Updates are applied to 2.18 with the newly determined $\mathbf{V}^{(k+1)}$:

$$\mathbf{I}_s^{k+1} = \mathbf{YV}^{k+1}. \quad (2.20)$$

The new \mathbf{I}_s^{k+1} and \mathbf{V}^{k+1} are employed in 2.19, and the procedure repeats until the calculated voltages converge.

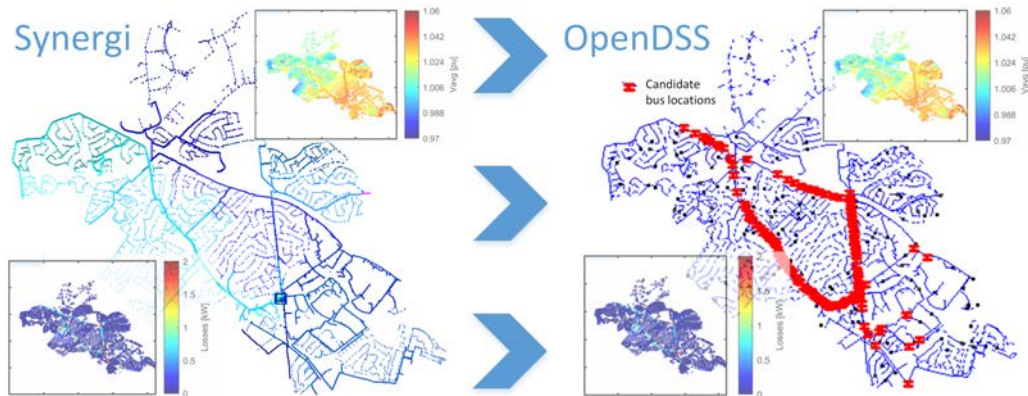


Figure 2.2: Comparison of the Synergi and converted OpenDSS circuit model line and component mappings for the original configuration of the actual 48MW, 9Mvar power distribution system KUs1. Also included for comparison are both individual bus voltage and line loss analyses for the peak load instance. The OpenDSS circuit diagram is labeled with the top candidate bus locations for CB installation. Candidacy is determined by a sensitivity analysis in terms of power loss reduction factor (rf_w) as discussed in section 2.5. Change in voltage for buses with high rf_w causes relatively significant change in power losses for connected lines. Such buses typically cluster near the main distribution feeder lines.

2.4 Large-Scale Utility Circuit Model Conversion

The example circuit, henceforth referred to as KUs1, utilized in the following study is a large 48MW, 9Mvar distribution system with AMI and is considered a candidate by its utility for implementing Conservation Voltage Reduction (CVR) and volt-var optimization (VVO) programs (Fig. 2.2). KUs1 is significant in complexity, boasting 3,839 buses and 6,854 nodes, which serves approximately 5,000 homes in the U.S.

A software tool to convert power distribution system models from Synergi, a utility power system simulation software, to OpenDSS [51] was developed with Python to enable the application of the OCP procedure on such circuits. This modeling procedure can also enable future CVR and VVO testing and benefit evaluation [5, 23, 24, 52].

The KUs1 circuit OpenDSS model is a full copy of its Synergi counterpart which

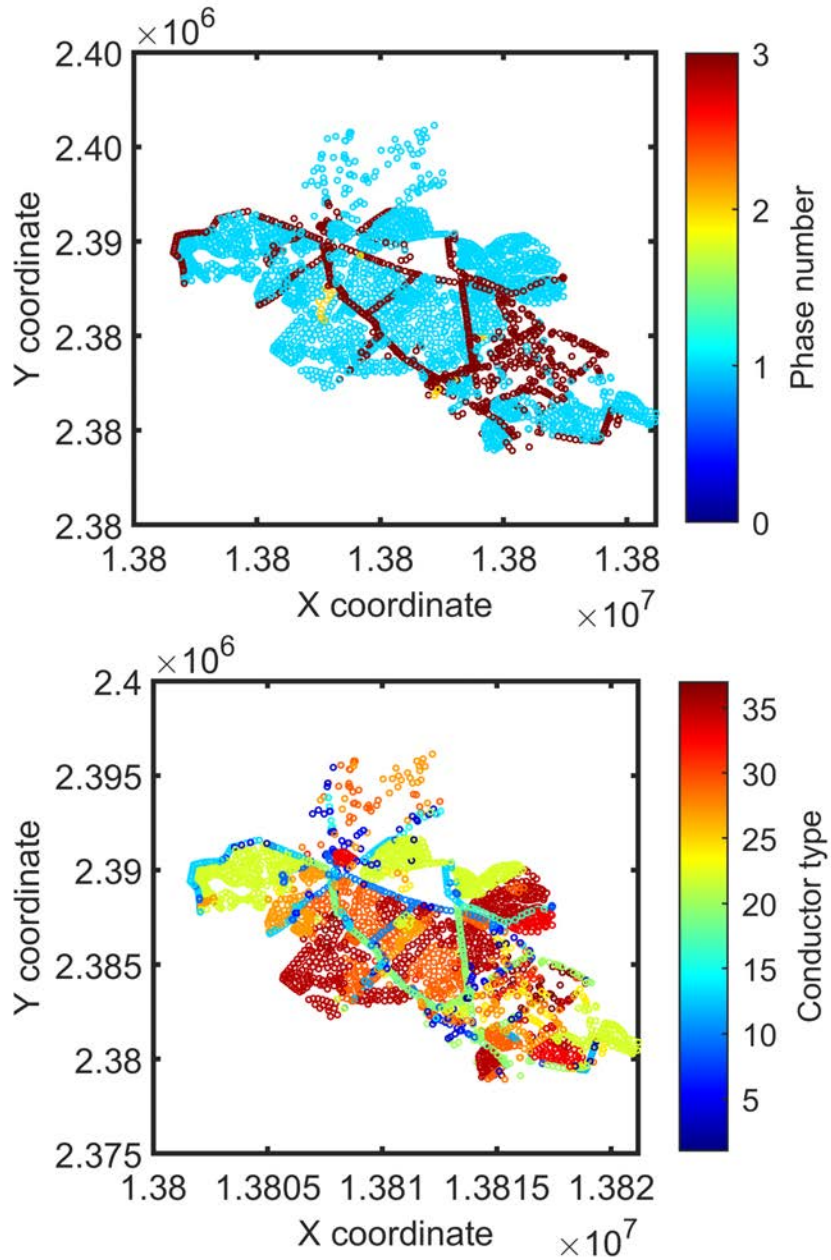


Figure 2.3: Geographical circuit schematics of different characteristics for KUs1, including number of phases and conductor type for the line associated with the buses.

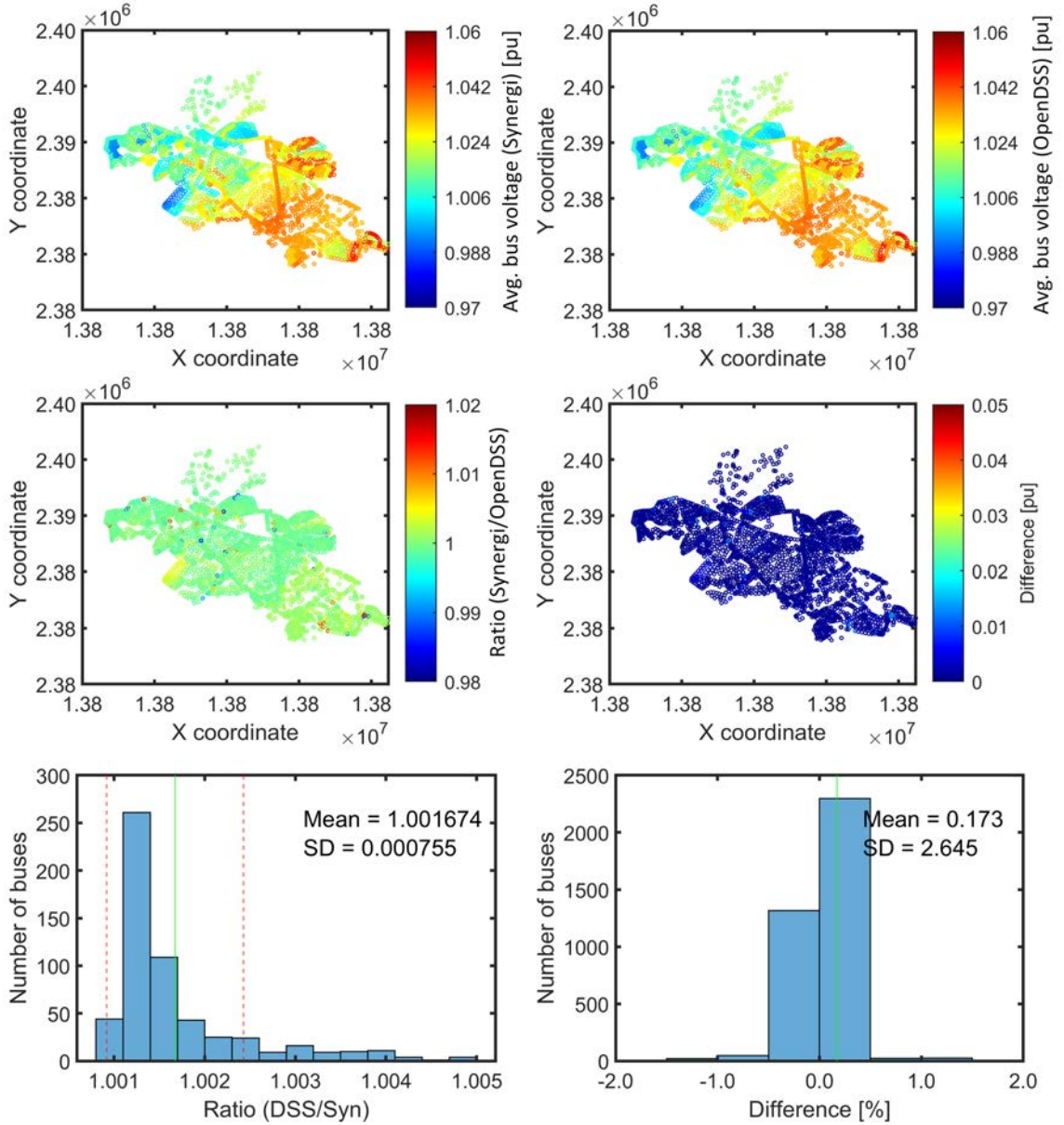


Figure 2.4: Summary of circuit conversion for KUs1 in terms of individual bus voltage, including Synergi and OpenDSS average bus voltages as well as the ratio and difference of Synergi to OpenDSS average bus voltages.

Table 2.1: Global circuit conversion summary

	Active power [MW]	Reactive power [Mvar]	Losses [Mw]
Synergi	47.67	9.39	0.55
OpenDSS	47.90	9.94	0.50
Absolute diff.	0.23	0.55	0.05
(relative diff.)	(0.48%)	(5.86%)	(9.09%)

includes the matching of line mapping, impedances, and power losses, spot load demand, active and reactive powerflow, and bus voltages. Synergi requires two database files as input to produce circuit models, including the network and equipment files. The equipment file provides important parameters and descriptions of circuit components, such as cables, transformers, switches, and CBs, typically employed by the utility. The network file describes the line mapping, component placement, peak load allocation, and operating details for the full circuit.

With the model conversion tool, circuit information is imported from the Synergi database input files and rewritten into OpenDSS format. To confirm accurate conversion, circuit model definitions and simulation results from both versions are compared at the global and individual component-level (Table 2.1). Line lengths, positive and zero sequence components, and connection node mapping as well as the peak active and reactive powers of loads connected at each bus matched exactly. Simulated average voltages of the 3,839 buses yielded minimal percent difference with a mean of 0.17% and standard deviation of 2.65%.

A smaller, more urban circuit with 2,409 buses, 4,829 nodes, 1 LTC transformer, 13 CBs, a peak power of 27.69MW/4.22Mvar was also successfully converted and referred to as LGEs1 (Fig. 2.5). In Figs. 2.3 and 2.6, the significant complexity of



Figure 2.5: Circuit schematic of LGEs1, indicating the location of its 13 CBs.

these circuit models are illustrated through geographical schematics of different circuit characteristics. Conversion summaries in terms of individual bus voltages after the transformer LTC tap settings were calibrated are also provided in Figs. 2.4 and 2.7.

Additional software for OCP has also been developed with Python by directly interfacing with the OpenDSS open-source software to employ as the modeling and simulation engine (Fig. 2.1). This tool set is utilized for the simulation of KUs1 at the peak load time instance for OCP and may be employed for time series simulation based upon a provided loadshape.

Such accurate circuit modeling and the prospective incorporation of AMI data to improve granularity in load modeling offers improved evaluation accuracy of effects from optimal planning and control. As an alternative to AMI, advanced load modeling

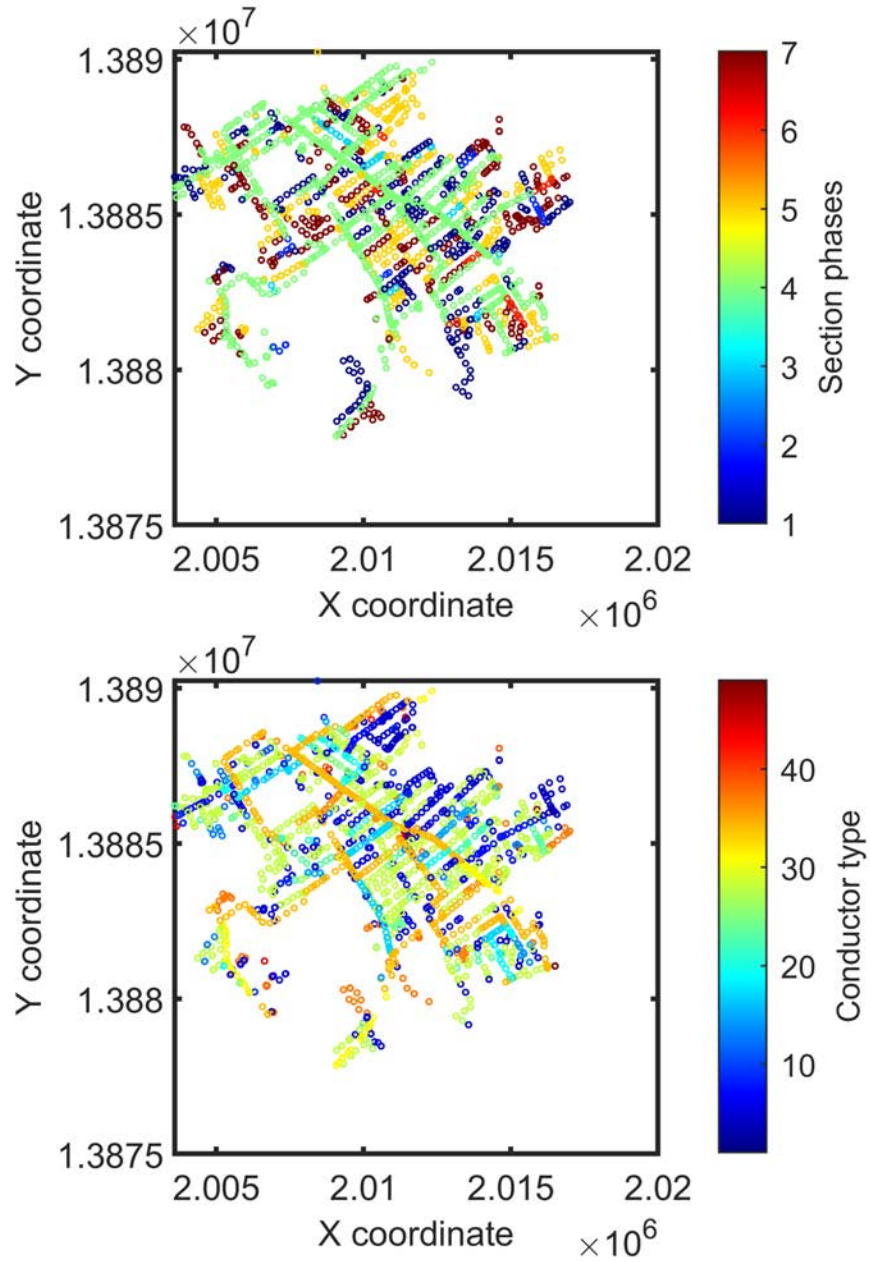


Figure 2.6: Geographical circuit schematics of different characteristics for LGEs1, including number of phases and conductor type for the line associated with the buses.

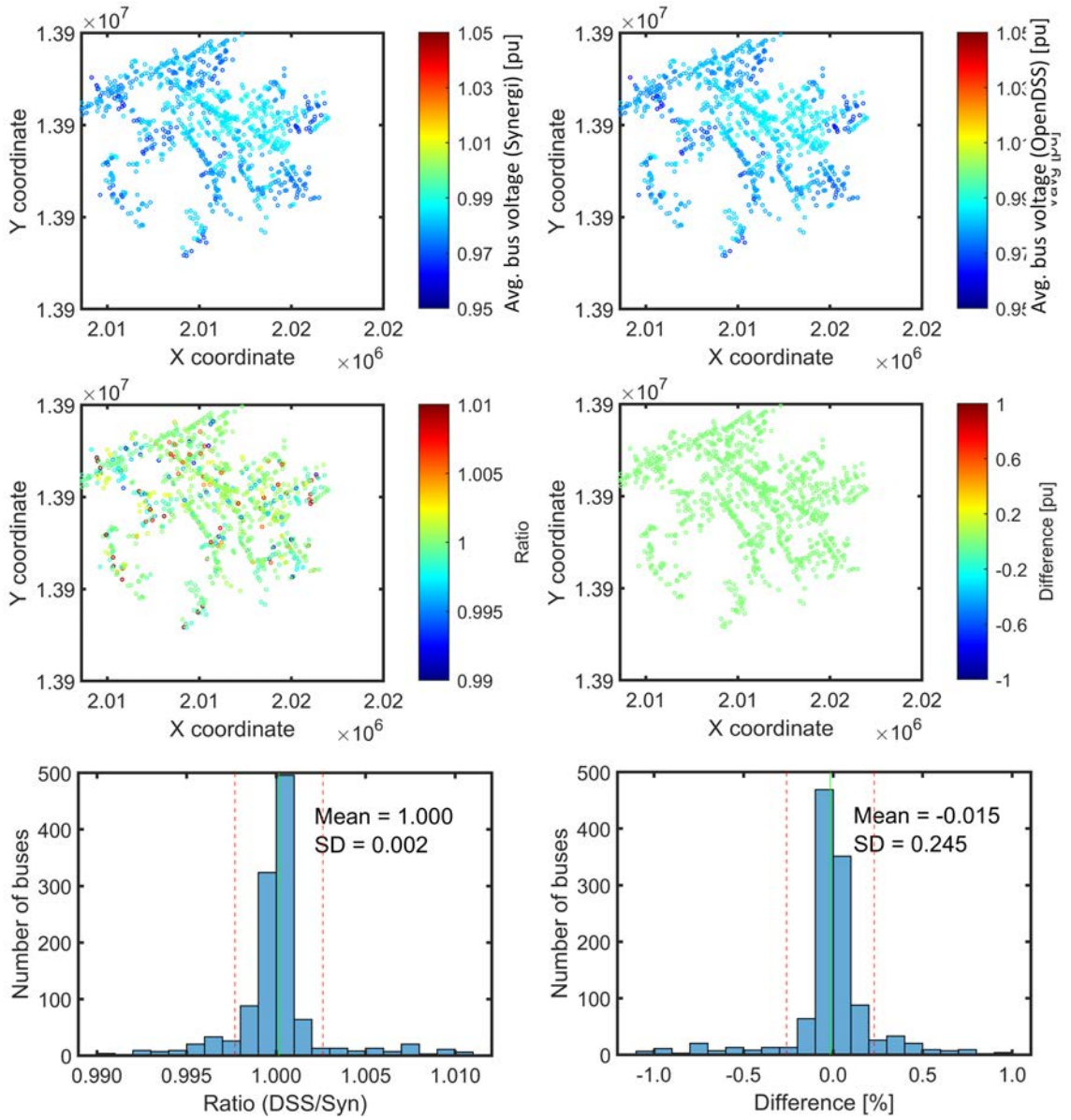


Figure 2.7: Summary of circuit conversion for KUs1 in terms of individual bus voltage, including Synergi and OpenDSS average bus voltages as well as the ratio and difference of Synergi to OpenDSS average bus voltages.

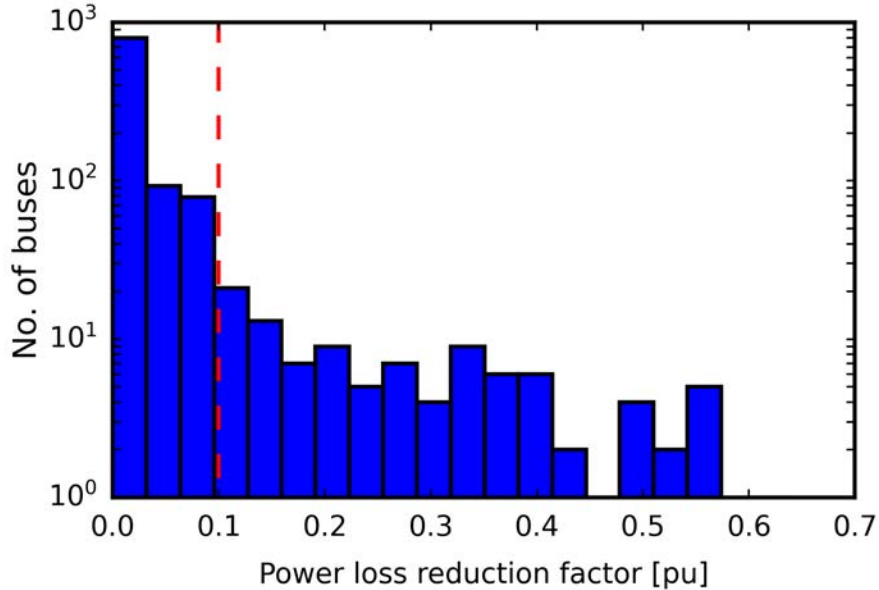


Figure 2.8: Histogram for rf_w of all buses in the KUs1 circuit with no. of occurrences on a logarithmic scale. Buses with higher rf_w correspond to those most sensitive to CB installation. The red line marks the minimum cutoff rf_w for consideration of candidacy.

through energy simulation of buildings and weather-dependent appliances is also of consideration [31, 53–56].

2.5 Problem Formulation and Sensitivity Analysis for Candidate Installation Buses

Multi-objective optimization for OCP is proposed to determine the Pareto set of optimal CB configurations at the peak load instance. Two formulations are considered, each with four optimization method variations, resulting in eight sets of results for the example T1 sub-circuit of KUs1, which corresponds to a single transformer (Table 2.2). An analysis is performed and provided in section 2.7 to establish the relative merits of each of the formulations and optimization methods in terms of resulting Pareto sets and possible configurations.

Both problem formulations consider the installed CB reactive power ratings [kvar] for candidate CB installation bus locations as independent variables, which are determined by a sensitivity analysis discussed later in this section (Fig. 2.8). They share the same discrete range of 0 to 1,200kvar in increments of 300kvar, which corresponds to typically available CB sizes at the distribution system level. Both placement and rating are optimized simultaneously through the inclusion of 0kvar as a rating option.

The common objectives for the two formulations are to minimize total active power losses ($w_{a,t}$) and investment represented by total installed CB rating ($c_{r,t}$):

$$\min \left[w_{a,t} = \sum_{i=1}^{n_l} (w_{a,l,i}) + \sum_{j=1}^{n_t} (w_{a,x,j}) \right], \quad (2.21)$$

$$\min \left[c_{r,t} = \sum_{i=1}^{n_c} (v_{r,i}) \right], \quad (2.22)$$

where n_c is the total number of CBs to be installed; $c_{r,i}$, the reactive power [kvar] rating of CB number i ; n_l , the total number of lines; $w_{a,l,i}$, the active power losses [kW] at line number i ; n_t , the total number of transformers; $w_{a,x,j}$, the active power losses [kW] at transformer number j ; n_b , the total number of buses; v_i , the average voltage of all phases at bus number i ; v_r , the reference voltage of 1.0pu.

For the second formulation, a third objective defined in equation (2.23) is proposed that minimizes the voltage variation throughout the circuit to improve distribution of CB installation locations and possibly reduce voltage violations over time, which is different from the typical approach that employs only two objectives. Lower voltage variation offers the prospect of reduced control operations and slower equipment degradation, which is being further explored in continued work. The function directly

minimizes standard deviation of node voltages ($v_{n,d}$) and is defined as:

$$\min \left[v_{n,d} = \sqrt{\frac{\sum_{i=1}^{n_n} (v_{n,i} - v_{n,a})^2}{n_n}} \right], \quad (2.23)$$

where n_n is the total number of nodes in the circuit; $v_{n,i}$, the voltage at node number i ; $v_{n,a}$, the mean voltage of all nodes.

To improve OCP performance and optimal configuration quality, a sensitivity analysis was performed to determine the best candidate bus locations for CB installation (Fig. 2.1). This effectively reduces the search space for the optimization algorithm and eliminates from consideration many buses that are not appropriate for CB installation by employing a power loss reduction factor (rf_w), defined as:

$$rf_w(i) = \frac{(\Delta w_i - \Delta w_{min})}{(\Delta w_{max} - \Delta w_{min})}, \quad (2.24)$$

where Δw_i , the difference in active power loss of the lines connected to bus i between two KUs1 simulation cases with transformer LTC tap settings set to 1.0pu and 1.05pu; w_{min} , the difference in minimum active power loss among the lines of the system; w_{max} , the difference in maximum active power loss among the lines on the system. rf_w captures the effectiveness of CB installation at a specific bus by determining the degree to which the change in active power losses of lines connected to the considered bus are dependent upon the change in voltage at that bus.

The list of candidate buses was further narrowed by excluding buses with fewer than three phases to comply with typical utility practices for CB installation. This effectively reduced the number of possible bus locations from approximately 4,000 to around 120. The bus candidate vector corresponds to the number of decision

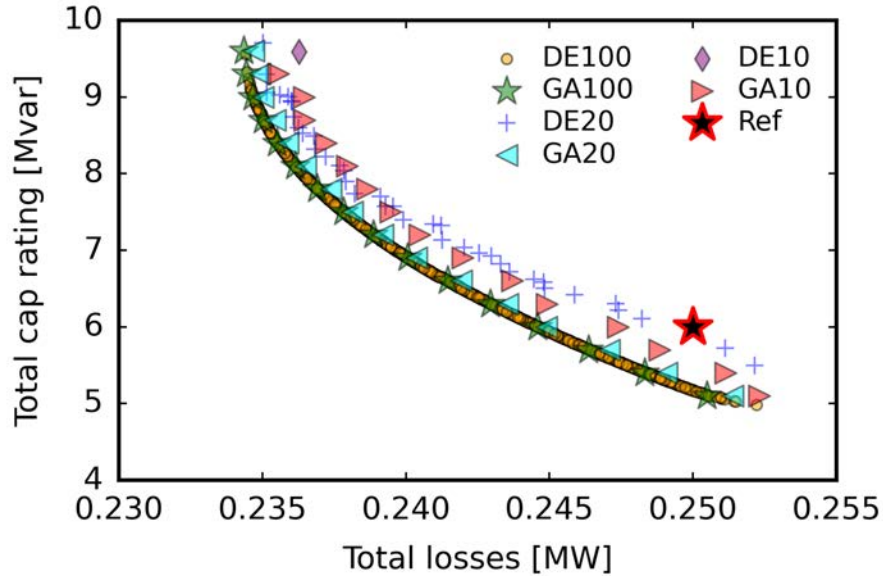


Figure 2.9: Comparison of resulting example Pareto sets for the KUs1 T1 sub-circuit from the most basic NM2 optimization employing the two considered optimization algorithms, NSDE (DE) and NSGA-III (GA), at different numbers of allowed generations as indicated legend labels.

variables in the multi-objective optimization and directly relates to simulation time. This is important as future work with time series simulation will rely upon such an optimization to apply controls as the load changes.

2.6 Optimization Algorithms

For the OCP methods, two optimization algorithms are considered, including a Non-Dominated Sorting Differential Evolution (NSDE) variant and the Non-Dominated Sorting Genetic Algorithm III (NSGA-III) (Fig. 2.9). DE was originally designed for single-objective scalar optimization and has been adapted with a non-dominated sorting function to solve the OCP multi-objective problem due to its efficiency and effectiveness [57].

NSGA-III is an extension of the NSGA-II algorithm that is tailored to optimization

problems that may have multiple objectives, which is innately suitable for OCP when coupled with a discrete independent variable set [58, 59].

Since typically available CB ratings are limited to larger units of 300kvar, an initial advantage of NSGA-III is the ability to employ a discrete independent variable set, whereas the NSDE variant may only utilize continuous variable ranges. This requires the NSDE method to incorporate an additional step to glean solutions with ratings that closely match what is actually available.

Algorithm 1 Pseudo-code for the OCP optimization algorithm with continuous independent variable ranges based on the differential evolution concept.

```

Generate initial population vector  $PC_{1,p}$ 
while termination criteria is not satisfied do
  for each population of power system configurations,  $p$ , in  $PC_{g,p}$  do
    Generate permutation of random indices,  $R$  ▷ Mutation
     $PC_{M,g,p} \leftarrow PC_{g,p}[R[0]] + SF(PC_{g,p}[R[1]] - PC_{g,p}[R[2]])$ 
    if  $RAND(0, 1) \leq CR$  then ▷ Crossover
       $PC_{U,g,p} \leftarrow PC_{M,g,p}$ 
    else
       $PC_{U,g,p} \leftarrow PC_{g,p}$ 
    end if
    if  $f(PC_{U,g,p}) \leq f(PC_{g,p})$  then ▷ Selection
       $PC_{g+1,p} \leftarrow PC_{U,g,p}$ 
    else
       $PC_{g+1,p} \leftarrow PC_{g,p}$ 
    end if
  end for
   $g \leftarrow g + 1$  ▷ Increment to next generation
end while

```

For initialization of the NSDE method, the configurations of selected ratings for the candidate installation bus locations within an initial population vector of the first generation are determined by use of uniform random number as follows:

$$PC_{g,p} = B_l + (B_u - B_l) * RAND_p(0, 1), \quad (2.25)$$

where g is the generation index and is equal to 1 to indicate the first generation; p , the population index and is equal to 1 to indicate the first population; B_u , the set of upper bounds; B_l , the set of lower bounds; $RAND_p(0, 1)$, a function that produces a set of random values between 0 and 1 equal in size to population p .

The configurations within the population $PC_{g,p}$ as defined in equation (2.25) are then mutated to create a new population ($PC_{M,g,p}$), which expands the search space:

$$PC_{M,g,p} = PC_{g,p} * R_0 + SF * [(PC_{g,p} * R_1) - (PC_{g,p} * R_2)], \quad (2.26)$$

where R is a random permutation of distinct configurations and sf is a scaling factor that produces more population diversity as it is increased. sf is a positive value and is typically set within the range of $[0,2]$ [57]. Based on the configurations from the target ($PC_{g,p}$) and mutated ($PC_{M,g,p}$) vectors, the cross-over procedure produces a population vector of trial configurations ($PC_{U,g,p}$) as follows:

$$PC_{U,g,p} = \begin{cases} PC_{M,g,p} & \text{if } RAND(0, 1) \leq cr \\ PC_{g,p} & \text{otherwise} \end{cases} \quad (2.27)$$

where cr is the cross-over probability. A random value for each of the individual configuration variables is generated as denoted by the $RAND(0, 1)$ function. Finally, the selection step compares the evaluations of the objective function for $PC_{U,g,p}$ and $PC_{g,p}$ to improve or maintain the quality of $PC_{g,p}$ for the next generation, $PC_{g+1,p}$:

$$PC_{g+1,p} = \begin{cases} PC_{U,g,p} & \text{if } f(PC_{U,n,p}) \leq f(PC_{n,p}) \\ PC_{g,p} & \text{otherwise} \end{cases} \quad (2.28)$$

This multi-step optimization procedure is repeated until the termination criteria is satisfied. The Pareto set, or epsilon non-dominated sorted solution set of best compromise, is then determined as the set of optimal configurations.

Since this variant of DE is multi-objective, the process will terminate once a maximum number of generations is reached. This maximum value is determined by trial and comparison as illustrated in Fig. 2.9. The flow of the NSDE algorithm is further illustrated in Alg. 1. Sets included in Algs. 1 and 2 are indicated by their capitalization.

Algorithm 2 Pseudo-code for the OCP optimization algorithm with discrete independent variable ranges based on the concept of NSGA-III.

Randomly generate initial population vector of power system configurations $PC_{g,c}$ of size n_{pop} where g is generation number
Define a set of distributed reference points RP
 $g \leftarrow 1$
while termination criteria is not satisfied **do**
 $PC_{g,S} \leftarrow \emptyset, i \leftarrow 1$
 $PC_{g,r} \leftarrow PC_{g,p} \cup PC_{g,c}$
 $F \leftarrow$ non dominated sorting of $PC_{g,r}$
 while $|PC_{g,S}| < N_{pop}$ **do**
 $PC_{g,S} \leftarrow PC_{g,S} \cup PC_{g,s}[i]$
 $i \leftarrow i + 1$
 end while
 $PC_{g,S} \leftarrow PC_{g,s}[i]$
 if $|PC_{g,S}| = N_{pop}$ **then**
 $PC_{g+1,p} \leftarrow PC_{g,S}$
 Criteria satisfied, break here
 else
 $P_{g+1,p} \leftarrow \cup_{j \leftarrow 1}^{l-1} PC_{g,s}[j]$
 Determine K number of points to be chosen from $PC_{g,s}$: $K \leftarrow N_{pop} - |P_{g+1}|$
 Normalize objectives
 Associate each member of $PC_{g,S}$ with a reference point $d \in H$
 Compute niche count of reference point j , where j is associated with member
 $k \in P_{g+1} \cap PC_{g,S}$
 Choose K members from $PC_{g,S}$ to construct P_{g+1}
 end if
 $g \leftarrow g + 1$ ▷ Increment generation
end while

Fundamentally, NSGA-II and NSGA-III follow the same process but with a different selection mechanism. In NSGA-II, new parent populations $PC_{g+1,p}$ are determined from a combined population $PC_{g,r}$, which is the union of the parent and child population sets ($PC_{g,p}$ and $PC_{g,c}$, respectively) ordered by their rankings. Let the set $PC_{g,s}$ be the non-dominated sorting of $PC_{g,r}$. For each configuration, i , in a population of size n_{pop} , let the set $PC_{g,S}$ having been initialized as an empty set be the union of itself $PC_{g,S}$ and $PC_{g,s}[i]$. If the size of $PC_{g,S}$ becomes greater than n_{pop} , then only those members with the largest crowding distances among the last non-dominated front $PC_{g,s}$ are selected.

In NSGA-III, the best members from $PC_{g,s}$ are, instead, selected from the supplied reference points RP . In this work, the set RP was determined based on the Das and Dennis procedure [60]. Next, with $PC_{g,S}$ and RP , each objective's values are normalized based on $PC_{g,S}$. Then, reference lines are constructed on a hyper-plane by joining the points of RP with the origin. The population members of $PC_{g,S}$ and $PC_{g,s}$ are then associated with a member of RP based on their closeness to the reference lines in the now normalized objective space.

The number of members from $PC_{g+1,p}$ that are in $PC_{g,S}$ which are associated with the members of RP are counted. If there is a reference point, or member of RP , that has no member associated with it and at least one of the members of $PC_{g,s}$ are associated with that member of RP , then the member of $PC_{g,s}$ with the shortest perpendicular distance to the corresponding reference line is added to PC_{g+1} . If all members of RP associate with at least one member of the population, then the member to be added to $PC_{g+1,p}$ is, instead, randomly selected from $PC_{g,s}$.

This procedure, starting from the initialization of $PC_{g,S}$ inclusive, is repeated until a termination criteria, such as the desired population size or maximum number of generations, is satisfied. The flow of the NSGA-III algorithm is further illustrated in Alg. 2.

In comparing NSDE and NSGA-III at maximum generation numbers of 10, 20, and 100, it is evident that NSGA-III yields Pareto sets of better quality with fewer required generations than NSDE (Fig. 2.9). This is an additional advantage of NSGA-III, which already employs a discrete independent variable range that eliminates the need for removing configurations with invalid CB ratings as in the NSDE case with continuous ranges.

The proposed OCP procedure is being adapted in on-going work to act as an optimal control function, which would occur at each timestep of a simulation (Fig. 2.1). The number of required generations directly determines computation speed, as each generation requires the same amount of time and produces the same number of configurations in the design space. Although a practically identical Pareto set is reached by the optimization algorithms eventually, the computation speed is an important aspect in enabling real-time operation of the optimal control functionality. Therefore, all considered multi-objective OCP formulations in the following study employ NSGA-III.

2.7 Multi-objective Optimization Methods

For each of the the two problem formulations defined in section 2.5, four optimization methods are considered. The methods are compared based on results from

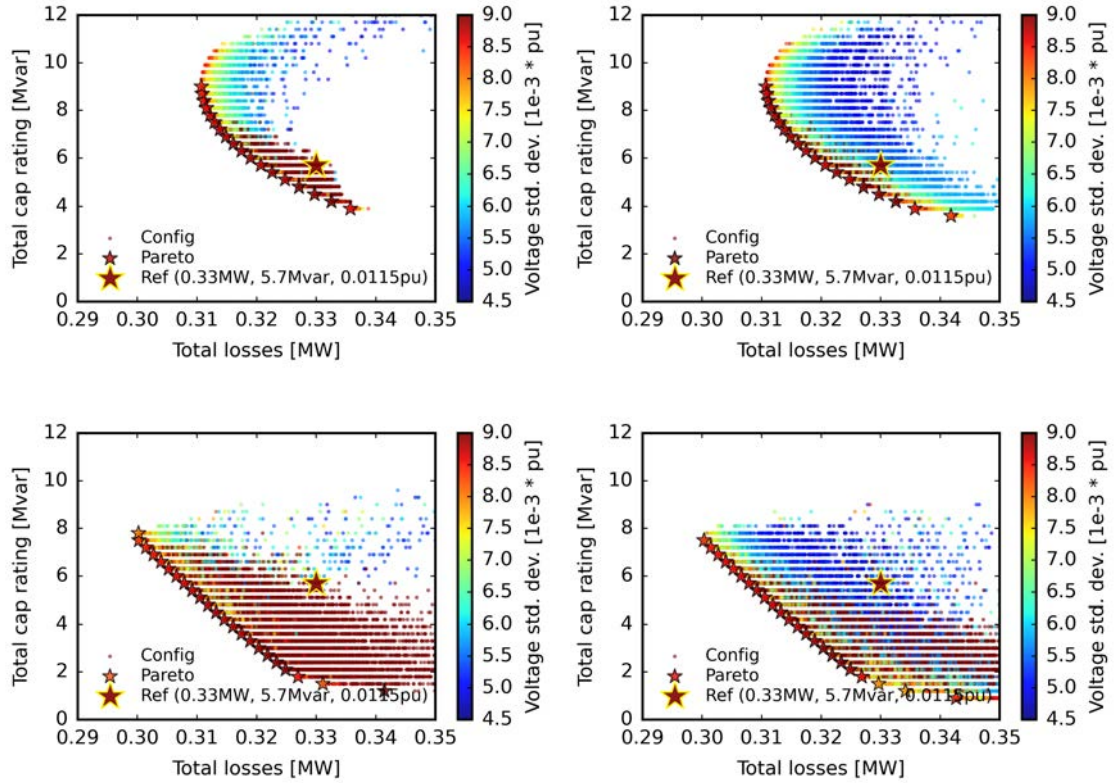


Figure 2.10: Possible configurations and Pareto sets for the (a) NM2, (b) PM2, (c) NA2, and (d) PA2 methods. Configurations with voltage violations of more than 0 are not considered and not illustrated within any of the plots. Introducing the penalty constraint as illustrated with PM2 and PA2 increases the breadth of the search space. It also provides additional valid configurations along the Pareto sets that require less investment. Incorporating automatic LTC tap setting adjustment within the optimizer, as in NA2 and PA2, improves overall $w_{a,t}$ and $c_{r,t}$.

Table 2.2: Characteristics of the eight (8) considered optimization methods.

Optimization method	NM2	PM2	NA2	PA2	NM3	PM3	NA3	PA3
$w_{a,t}$ objective	Y	Y	Y	Y	Y	Y	Y	Y
$c_{r,t}$ objective	Y	Y	Y	Y	Y	Y	Y	Y
$v_{n,d}$ objective	N	N	N	N	Y	Y	Y	Y
Penalty constraint on voltage violations	N	Y	N	Y	N	Y	N	Y
Automatic LTC tap setting adjustment	N	N	Y	Y	N	N	Y	Y

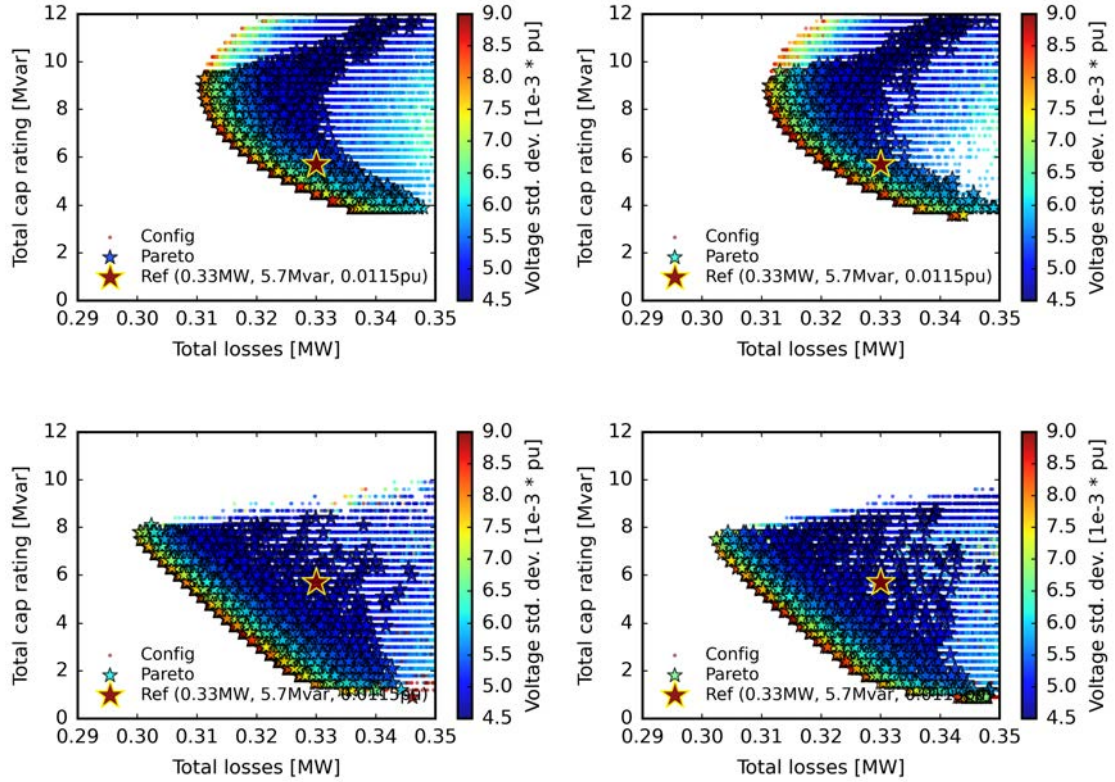


Figure 2.11: Possible configurations and Pareto sets for the three-objective (a) NM3, (b) PM3, (c) NA3, and (d) PA3 methods. Configurations with voltage violations of more than 0 are not considered and not illustrated within any of the plots. Effects observed in Fig. 2.10 remain present. The additional third objective increases focus by the optimizer in the region of increased $c_{r,t}$ and yields configurations with improved $v_{n,d}$, including some with penalty to $w_{a,t}$ and $c_{r,t}$, which indicates it's independence as a third objective.

the KUs1 T2 sub-circuit simulation. Corresponding merits are established in terms of Pareto set results and possible configurations. The differences in the four approaches include the incorporation of a penalty constraint for configurations with voltage violations and the method of adjusting the tap settings at the corresponding LTC transformer (Tab. 2.2).

The voltage violation penalty constraint is enacted by counting the the number of voltage violations experienced in each configuration considered by checking whether any nodes within the circuit have a voltage greater than 1.05pu or less than 0.95pu. When voltage violations are detected, $w_{a,t}$ is heavily penalized such that the configuration is no longer considered valid by the optimizer (Fig. 2.15).

For LTC transformer tap setting adjustment, two methods are considered. In the first, the LTC tap settings are manually adjusted in 1/32 increments, which corresponds to 32 possible settings, within a band of +/- 5% for the existing reference circuit such that bus voltages are as low as possible without causing any voltage violations (Fig, 2.15). Then, the tap settings are left unchanged for all configurations proposed by the optimizer.

Tap settings are determined and controlled by the optimizer in the second method so that power distribution system effects due to new CB configurations are considered concurrently. This is achieved by adding the tap settings as additional independent variables with a discrete range of 32 tap settings as applied in the manual adjustment technique.

The assigned optimization type names identify whether the penalty constraint is

employed (no penalty (N) or with penalty (P)) as well as the method of tap setting adjustment (manual, M, or automatic, A) and the number of objectives (2 or 3) considered (Table 2.2). The most basic optimization method, NM2, yields an anticipated Pareto set of optimal CB configurations illustrated in Fig. 2.10a. Such configurations are favorable with respect to the reference case, which operates with relevantly average $c_{r,t}$.

For this case in the T2 sub-circuit, many options exist through which $w_{a,t}$ may be improved, even with reduced $c_{r,t}$. Configuration quality is very similar for PM2 as in NM2 with an expanded solution set throughout the lower region of reduced $c_{r,t}$, which is due to the penalty constraint against voltage violations (Fig. 2.10b). The expansion in search space by penalty constraint is also evident between NA2 and PA2 (Figs. 2.10c and 2.10d).

Introducing the automatic LTC transformer tap adjustment function in cases NA2 and PA2 considerably improves both the $w_{a,t}$ and $c_{r,t}$ across the set of possible solutions. Additionally, configurations of lower $c_{r,t}$ have especially improved $w_{a,t}$, as indicated by the steeper slope of the Pareto set (Fig. 2.12). Minimal $w_{a,t}$ is achieved by enabling the power system to operate at the highest voltage without violating standard limits. In the NA2 and PA2 cases, the optimizer is able to adjust the voltage of the entire system through LTC transformer tap control as well as increase the voltage of targeted nodes with particularly high rf_w .

The additional penalty constraint against voltage violations increases the size of the search space but more generally and without such focus in the lower $c_{r,t}$ region, especially for PA3 (Figs. 2.11 and 2.12). As anticipated, $v_{n,d}$ is mostly dependent upon

CB placement with some correlation to increased $c_{r,t}$ since more CBs are available to improve voltage uniformity. (Fig. 2.13).

The optimizer shifts in focus to the higher $c_{r,t}$ region for three-objective methods, since such optimal configurations can now also offer reduced $v_{n,d}$, sometimes with penalty to $w_{a,t}$. This adjusted focus is more so evident in methods NA3 and PA3, since configurations produced with these techniques can provide additional loss mitigation from higher tap settings without voltage violations through improved voltage uniformity (Fig. 2.14).

Three-objective methods also provide additional configurations among the Pareto set with improved $v_{n,d}$ that do not necessarily correlate with the other two objectives. This contribution enables analysis of the trade-offs between all three without losing quality in configurations that focus more upon $w_{a,t}$ and $c_{r,t}$. Across methods, it may be observed that the relationship between $w_{a,t}$ and $c_{r,t}$ inverts at very high $c_{r,t}$ due to over-correction and the addition of too much reactive power into the system such that flow reverses. The implementation of the investment objective, represented by total CB power rating, may be further developed as the total number of individual CBs as well as their geographical location can also contribute.

Additionally, the application of these methodologies to CB switching and LTC settings for time-series optimal control of established devices is being considered to reduce total distribution system power by activating CVR and VVO functions without voltage violations. The evaluation of benefits yielded by these functions is enabled through ZIP parameter modeling of the distribution system loads to capture their voltage dependency. Advanced load modeling techniques, such as the incorporation

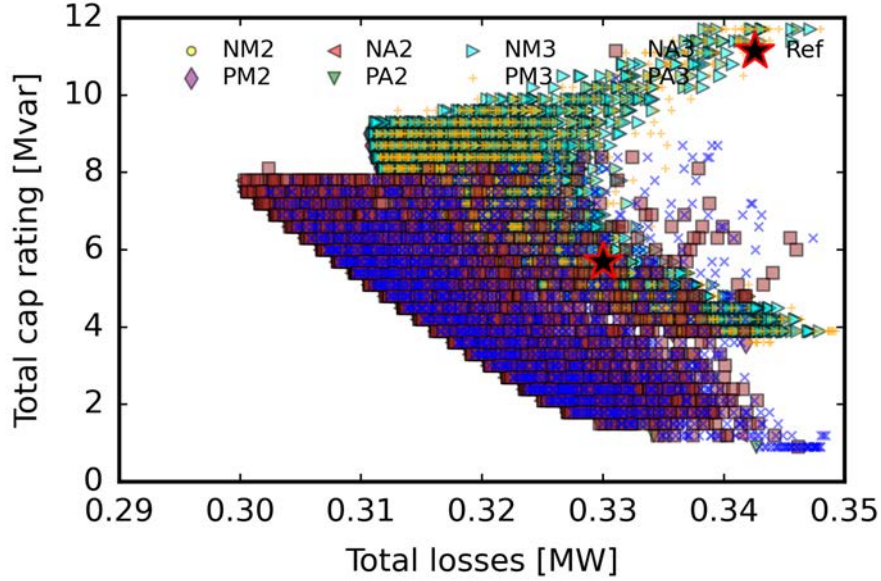


Figure 2.12: Pareto sets of $w_{a,t}$ and $c_{r,t}$ for all eight (8) optimization methods. The introduction of automatic LTC tap adjustment improves overall $w_{a,t}$ and $c_{r,t}$, especially for configurations of lower $c_{r,t}$.

of AMI data as it becomes more available from utilities, can improve the accuracy of such evaluation as it becomes more available in emerging smart grids [49].

2.8 Optimal Configuration Selection through Sub-circuit Analysis

The PA3 optimization technique was also applied to the other two sub-circuits of KUs1 (T1 and T3, Figs. 2.16 and 2.17). A decision-making procedure is proposed for configuration selection through the pseudo-weight vector approach [61]. Since the multi-objective optimization of PA3 minimizes three objectives, three weights with the requirement that they must sum to one are provided to the decision-making function to return a solution. For each solution s among the entire solution set S , this selection method calculates a pseudo weight for each objective obj by determining the normalized distance to the worst solution corresponding to each obj through the

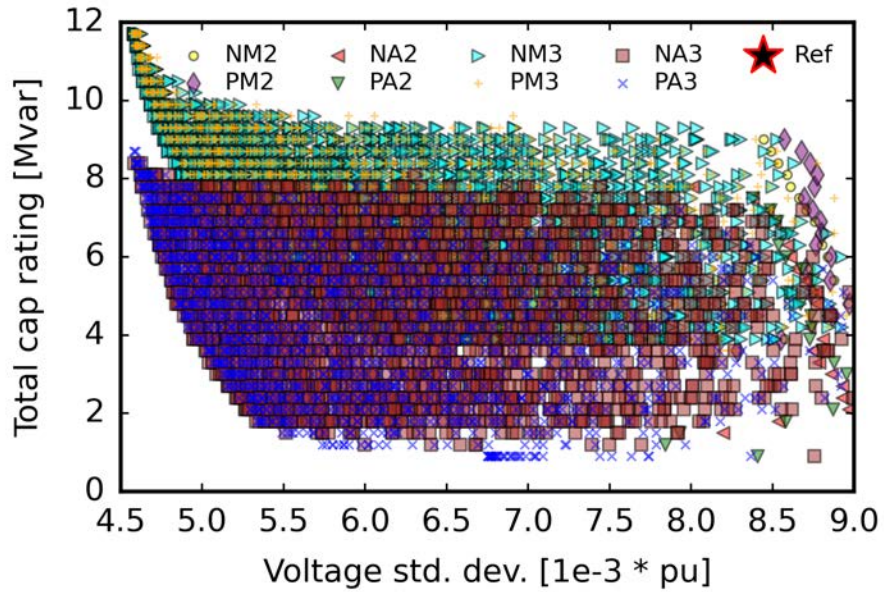


Figure 2.13: Pareto sets of $c_{r,t}$ and $v_{n,d}$ for all eight (8) optimization methods. $v_{n,d}$ is mostly dependent upon CB placement with some correlation to increased $c_{r,t}$ since more CBs are available to improve voltage uniformity.

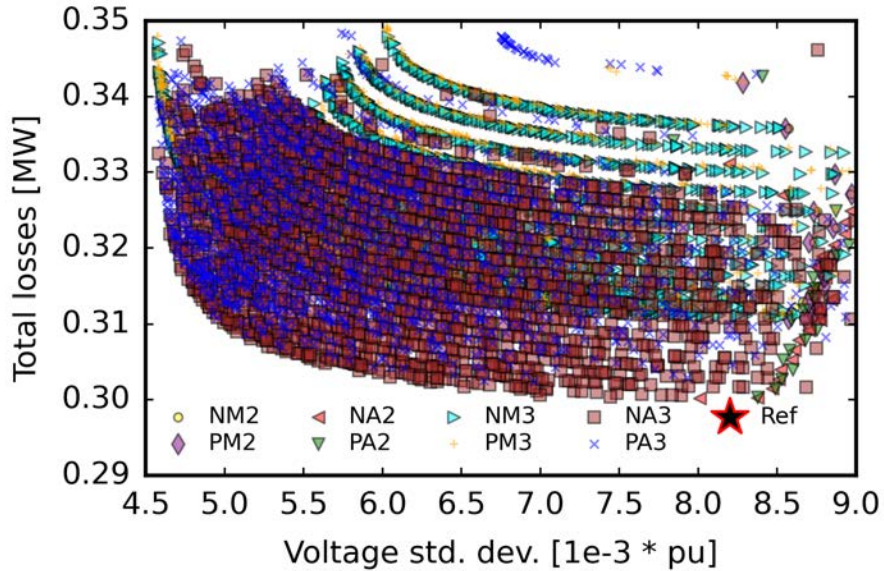


Figure 2.14: Pareto sets of $w_{a,t}$ and $v_{n,d}$ for all eight (8) optimization methods. Higher tap settings in the LTC tap function-enabled NA3 and PA3 methods further reduce $w_{a,t}$, which was made possible in part by improved $v_{n,d}$.

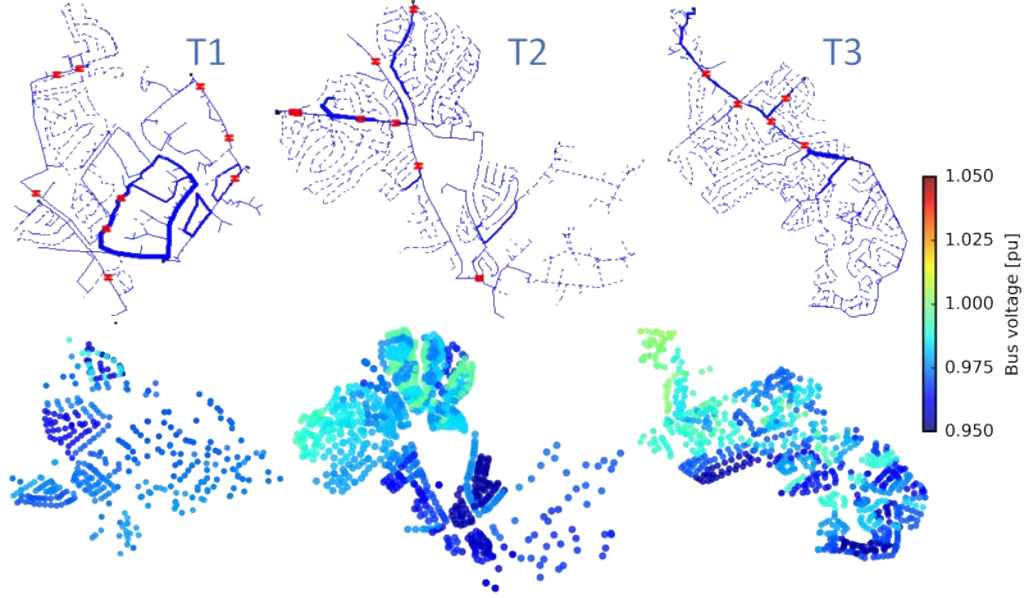


Figure 2.15: Circuit diagrams with reference CB locations and bus voltages for the three KUs1 sub-circuits corresponding to substation transformers with manually calibrated tap settings such that voltages operate as low as possible without any voltage violations.

equation:

$$pw_{obj} = \frac{(f_{obj}^{max} - f_{obj}(s))/(f_{obj}^{max} - f_{obj}^{min})}{\sum_{n=1}^N [((f_n^{max} - f_n(s))/(f_n^{max} - f_n^{min}))]} \quad (2.29)$$

where f_{obj}^{max} is the maximum result of obj among the solutions in S ; $f_{obj}(s)$, the result of obj for s ; f_{obj}^{min} , the minimum result of obj among the solutions in S ; N , the set of objectives for each s of the set S ; f_n^{max} , the maximum result of objective n for all of S ; $f_n(s)$, the result of objective n for s ; f_n^{min} , the minimum result of objective n for all of S .

Four unique circuit configuration types from among the Pareto sets of the three sub-circuits of KUs1 (T1, T2, and T3) were selected for comparison. The three circuits are simulated at their respective peak load instances, and their actual reference CB configurations are provided as "Ref" (Fig. 2.15).

Table 2.3: Percent change to circuit characteristics applied by selected optimal configurations with respect to reference ("Ref") configuration and compromise factors as defined in Eq.2.30

Sub-circuit	T1				T2				T3			
Configuration	C	W	Q	D	C	W	Q	D	C	W	Q	D
δ_w	-2	-7	15	10	-2	-8	5	4	-7	-10	-3	-2
δ_q	40	30	-70	155	5	10	-42	90	130	120	70	210
δ_d	-3	-6	9	-11	-50	-36	-32	-63	-26	-21	-15	-33
$cf_{w,q}$	0.05	0.23	0.21	0.06	0.40	0.80	0.12	0.04	0.05	0.08	0.04	0.01
$cf_{d,q}$	0.08	0.20	0.13	0.07	10.00	3.60	0.76	0.70	0.20	0.18	0.21	0.11
$cf_{w,q}$	0.67	1.17	1.67	0.91	0.04	0.22	0.16	0.06	0.27	0.48	0.20	0.06

Among the selected solutions are the three most extreme cases with the objectives of $w_{a,t}$, $c_{r,t}$, and $v_{n,d}$, which are respectively defined in equations (2.21), (2.22), and (2.23), weighted at 100% and labeled as cases "W", "Q", and "D". The fourth configuration, "C", is an equal compromise of the objectives with weights of 33% each.

To further enable comparison of sub-circuits and capture compromise between objectives for the selected configurations in terms of improvement from the reference cases, compromise factors between the three objectives are proposed and calculated as follows:

$$cf_{w,q} = \left| \frac{\delta_w}{\delta_q} \right|, \quad cf_{d,q} = \left| \frac{\delta_d}{\delta_q} \right|, \quad cf_{w,d} = \left| \frac{\delta_w}{\delta_d} \right| \quad (2.30)$$

where $cf_{w,q}$ is the compromise factor between active power losses ($w_{a,t}$) and total CB power rating ($c_{r,t}$); $cf_{d,q}$, between voltage standard deviation ($v_{n,d}$) and $c_{r,t}$; $cf_{w,d}$, between $w_{a,t}$ and $v_{n,d}$; δ_w , the absolute percent change in $w_{a,t}$ between the reference and selected configuration; δ_q , the absolute percent change in $c_{r,t}$; δ_d , the absolute percent change in $v_{n,d}$.

Among the three sub-circuits, T1 has exceptionally low δ_d across the selected

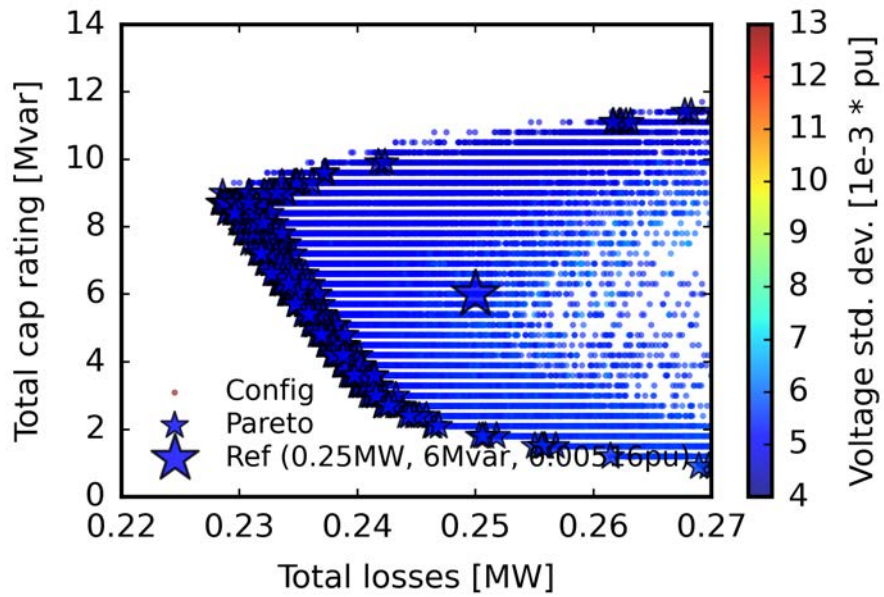


Figure 2.16: Possible configurations and Pareto set for T1. $v_{n,d}$ is exceptional for all configurations, including Ref, in comparison to T2 and T3. Improved $w_{a,t}$ is achieved with less $c_{r,t}$ with respect to Ref.

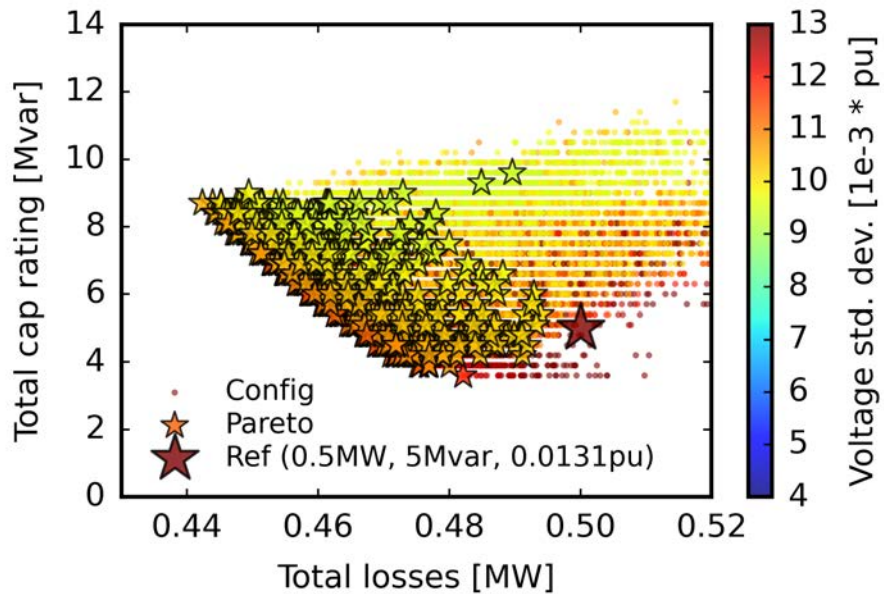


Figure 2.17: Possible configurations and Pareto set for T3. Considerable improvement of $v_{n,d}$ possible with reduced $c_{r,t}$ and $w_{a,t}$ compared to Ref.

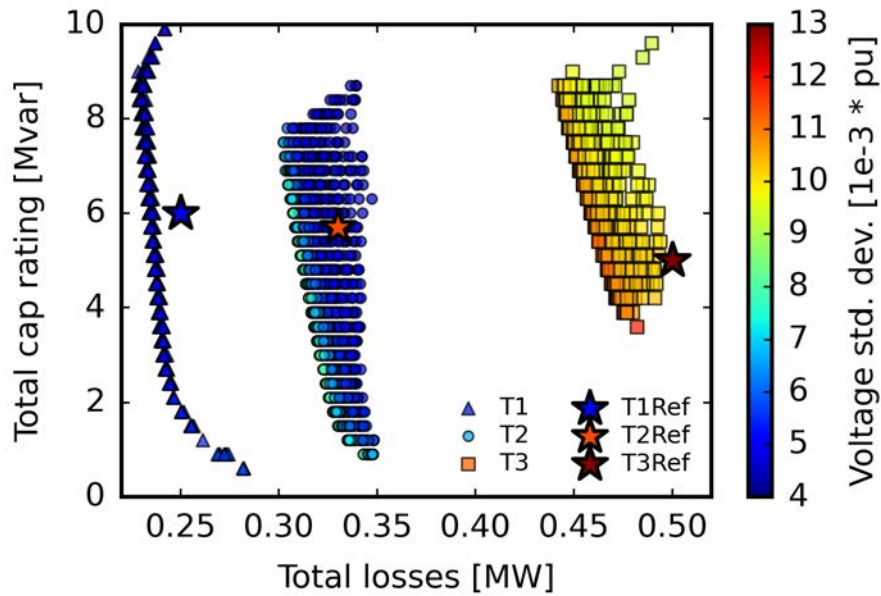


Figure 2.18: Comparison of the three Pareto sets with shared axes to illustrate how each sub-circuit may benefit from OCP with respect to their corresponding reference configurations and to each other in terms of the three objectives. T1 can experience similar $w_{a,t}$ with much less $c_{r,t}$ than Ref and no penalty to $v_{n,d}$. Opportunity exists for T2 and T3 to improve in $v_{n,d}$ with less $w_{a,t}$. T2 can achieve this with even less $c_{r,t}$ than Ref, whereas T3 would require more to yield similar benefits.

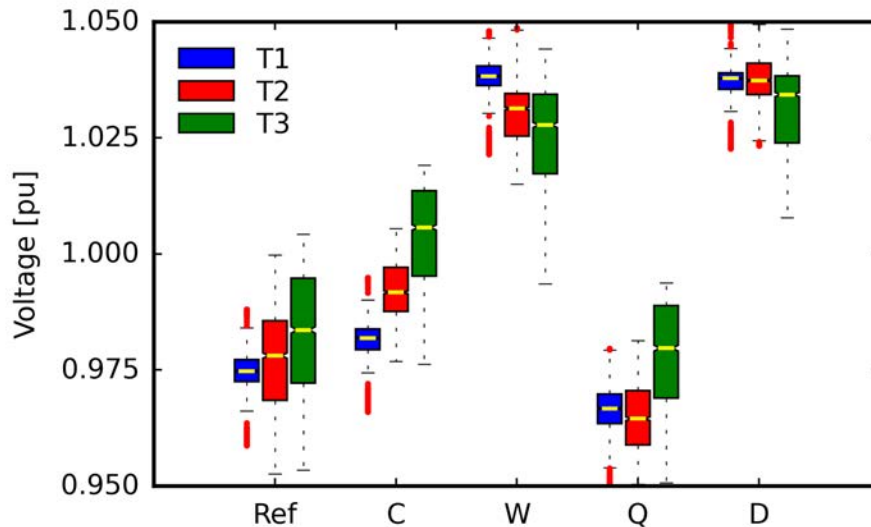


Figure 2.19: Circuit bus voltages of the three sub-circuits for each selected configuration type. As anticipated, D reduces $v_{n,d}$ more than the other configurations. Both T2 and T3 experience more $v_{n,d}$ than T1 and have the most opportunity for improvement in that regard.

configuration types and a low $cf_{d,q}$. This indicates that the base circuit excels in voltage uniformity regardless of CB configuration (Table 2.3 and Fig. 2.18). Such stable voltage along with higher $cf_{w,q}$ suggests that the compromise between $w_{a,t}$ and $c_{r,t}$ be of primary focus for configuration selection. Based on configuration Q, reducing the $c_{r,t}$ by 70% would yield a δ_w of only 15%. So, the CBs in the T1 sub-circuit could be reconfigured with similar $w_{a,t}$ and $v_{n,d}$ with much less $c_{r,t}$.

For T2, δ_d has the most range with all configuration types, boasting reductions of up to 63% as well as very high values of $cf_{d,q}$. This indicates that the system is most sensitive to CB placement in terms of voltage variation (Fig. 2.19). Similar to T1, T2 could also be reconfigured with better δ_q , as much as -42%, at a small δ_w of up to 5%. The more favourable selection for T2 would considerably improve $v_{n,d}$ with a small penalty to $w_{a,t}$ at much lower $c_{r,t}$.

The T3 sub-circuit is different from T1 and T2 in that it requires considerably more $c_{r,t}$ to achieve similar improvements in $w_{a,t}$ and $v_{n,d}$. The W configuration offers the best δ_w of -10%, but at a high δ_q of 120% and with a very low $cf_{w,q}$ of 0.08. δ_q increases further to 210% for the D configuration, yielding a significant δ_d of -33% at a low $cf_{d,q}$ of 0.11. Therefore, reconfiguration of T3 based upon the corresponding Pareto set would require more $c_{r,t}$ of at least a 70% increase to begin realizing improved δ_w and δ_d as in T1 and T2.

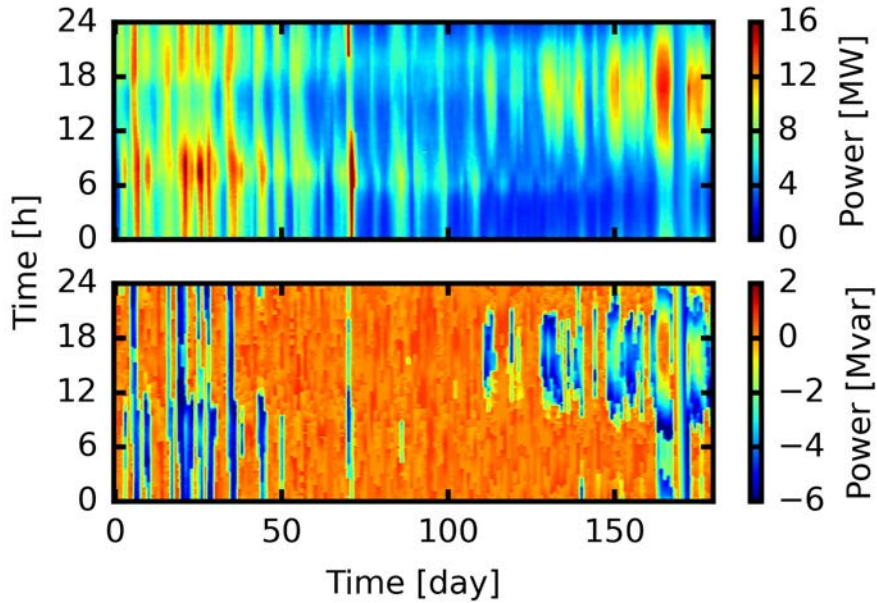


Figure 2.20: Example six month loadshape from January to June 2022 for total active (top) and reactive (bottom) power measured at the KUs1 T2 substation transformer every minute.

2.9 Time Series Evaluation of Circuit Configurations

Traditionally, the effectiveness of CBs may be considered only at peak load as this is usually the most extreme case for energy use and lower voltage. Since power distribution systems typically do not operate at this level of load, the effects of the installed CBs may not be adequately captured. An evaluation procedure through stochastic analysis extended from [52] is proposed to capture and compare the performance of different CB configurations in a power distribution system over an example six month period for the KUs1 T2 sub-circuit as illustrated in Fig. 2.20.

To enable time series simulation, global multipliers for total active and reactive power are calculated based on the measured peak load of the circuit and minutely loadshape data captured at the corresponding substation transformer (Fig. 2.21).

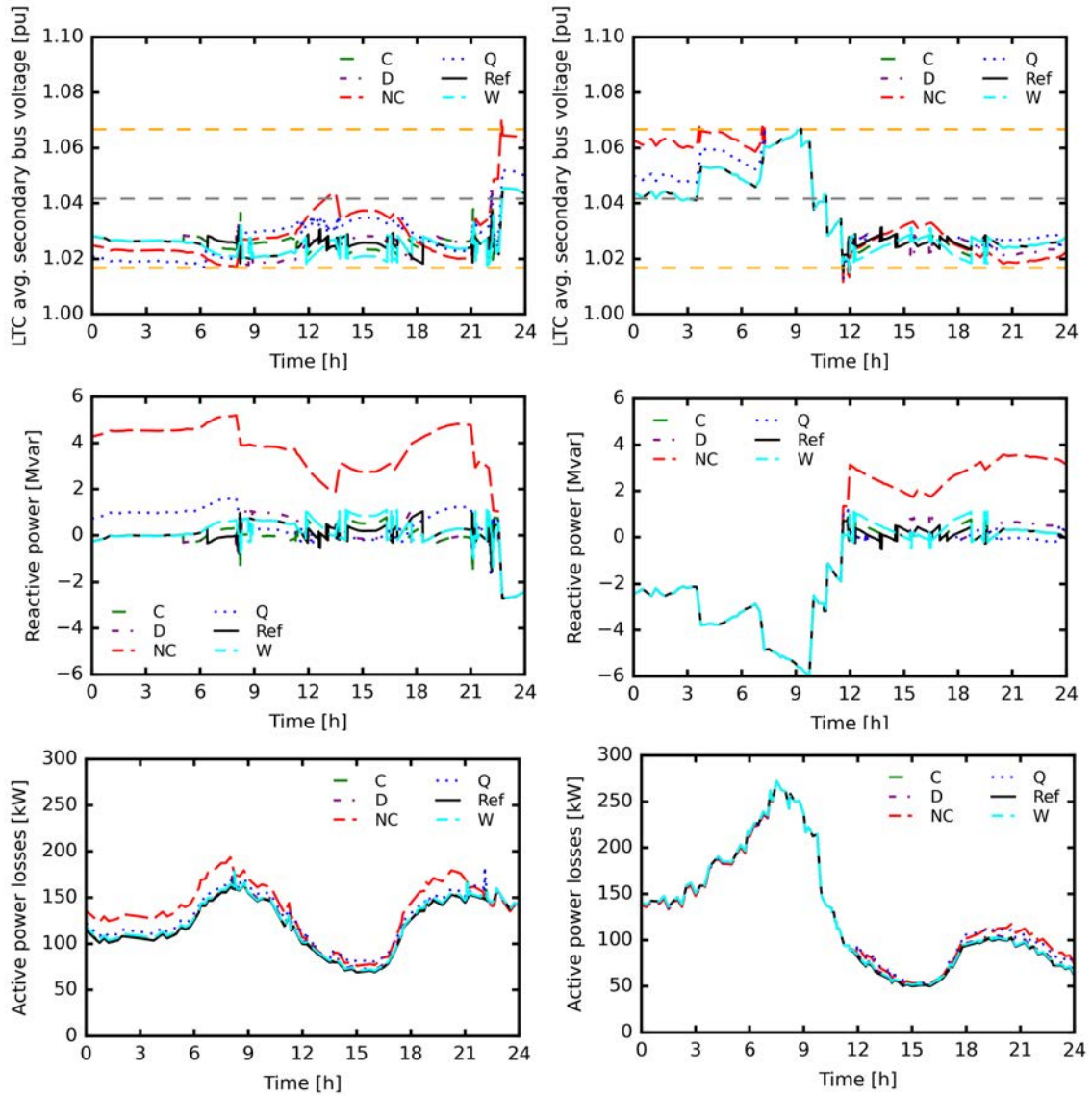


Figure 2.21: Two consecutive example days (left and right columns) from the full 180-day minutely simulations of KUs1 T2 in all considered configurations with results for LTC secondary bus voltage (top row) as well as total reactive power (middle row), and total active power losses (bottom row).

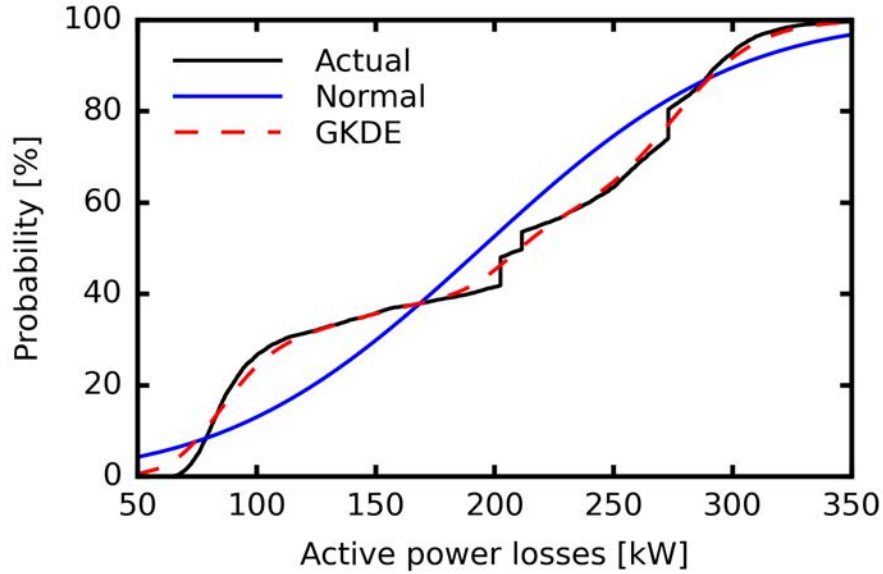


Figure 2.22: Comparison of distribution fits through CDFs of active power losses over an example week-long period.

These multipliers are applied to the individually connected loads at each timestep with the assumption that the global loadshape is representative [23]. The prospective application of local AMI data to improve granularity of the simulated individual load behavior may also be incorporated in the circuit simulation framework as it becomes more available.

A controller was implemented during the time series simulation that mimicked conventional control of LTC transformers and CB switching. The LTC tap adjustment control is described in detail in CB5. The CB switching control was issued such that they would remain on as long as corresponding bus voltages remained below 1.05pu. The CBs also individually trip if total system reactive power flows in reverse back into the substation (Fig. 2.21). A five minute control limit is set after a trip command to ensure full discharge before executing the next close command.

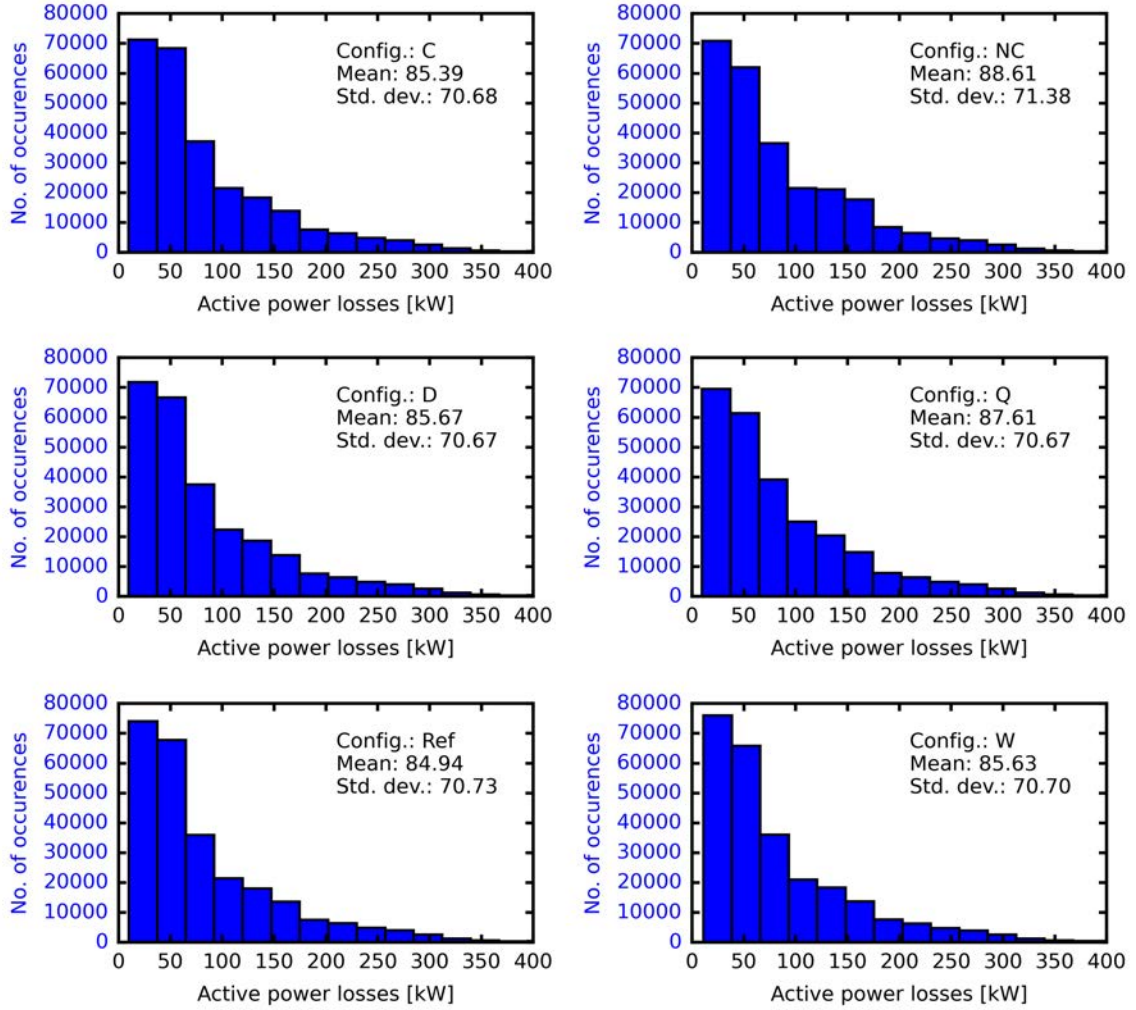


Figure 2.23: Histograms and resulting PDFs assuming a normal distribution for each of the considered configuration types in terms of total active power losses.

The procedure may consider any representative value for the total circuit performance per timestep. Considering active power losses and average voltage of all individual buses as examples for the evaluation procedure due to their association with the OCP main objectives, respective histograms are illustrated in Figs. 2.23 and 2.24 for all configuration types considered in previous sections.

Gaussian Kernel Density Estimation (GKDE) may also be employed to determine the shape of the distribution, and is described as:

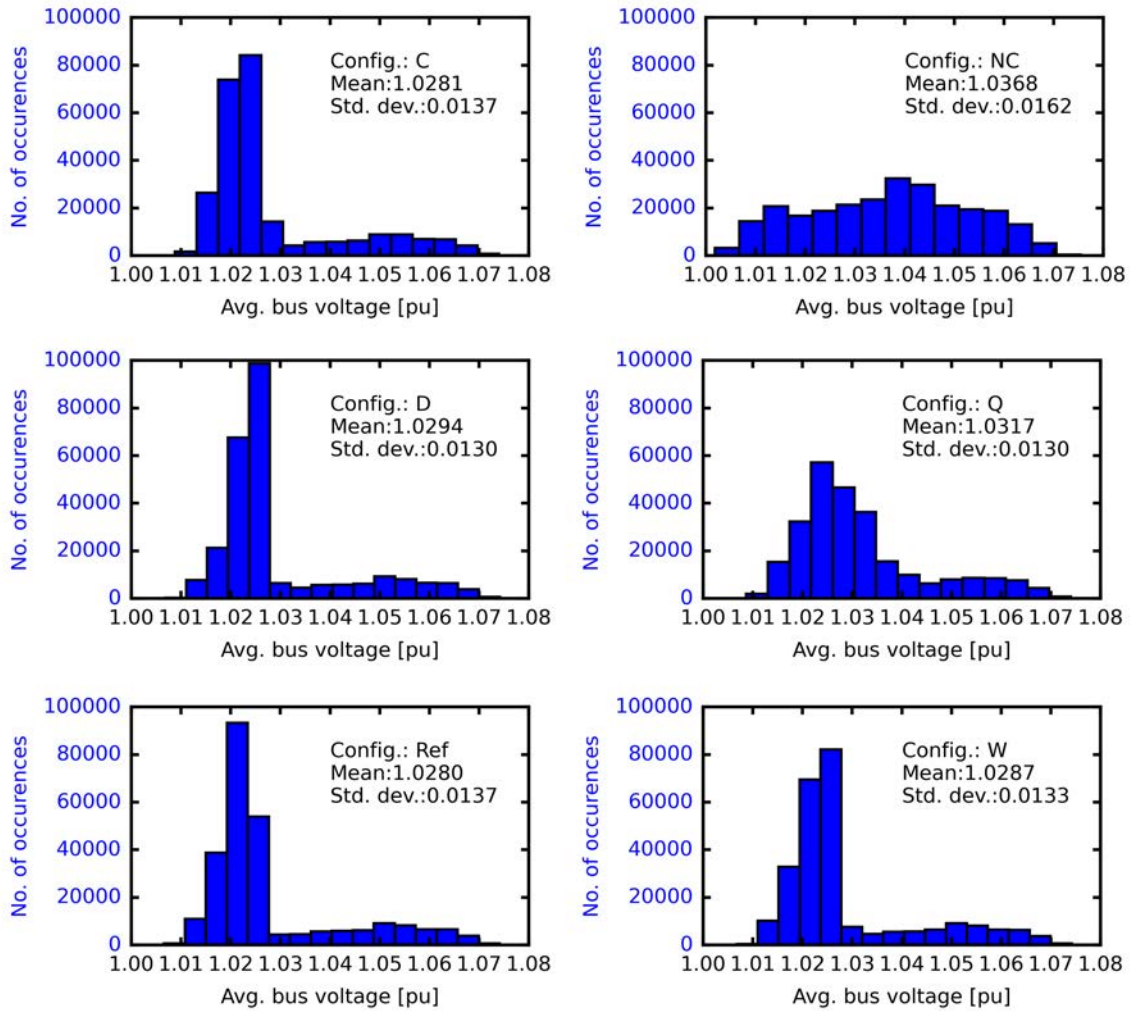


Figure 2.24: Histograms and resulting PDFs assuming a normal distribution for each of the considered configuration types in terms of average voltage for all power system buses.

$$\widehat{f}_G(x; h) = \frac{1}{n} \sum_{i=1}^n K(x - x_i; h), \quad (2.31)$$

where a PDF data set $X = \{x_1, x_2, \dots, x_n\}$, K , the kernel function, which is defined as:

$$K(x - x_i; h) = \frac{1}{\sqrt{2\pi}h} e^{-\frac{(x-x_i)^2}{2h^2}}, \quad (2.32)$$

where h is the bandwidth [53]. Scott's rule is employed to determine the bandwidth such that it is large enough to reduce the variance of the PDF and small enough to mitigate the bias [62].

Employing GKDE to determine the circuit-specific PDF for performance metrics allows for the inferencing and general capture of probable circuit behavior based upon limited observed data. The PDFs may be translated into a cumulative distribution function (CDF) for direct comparison of performance over time (Fig. 2.22).

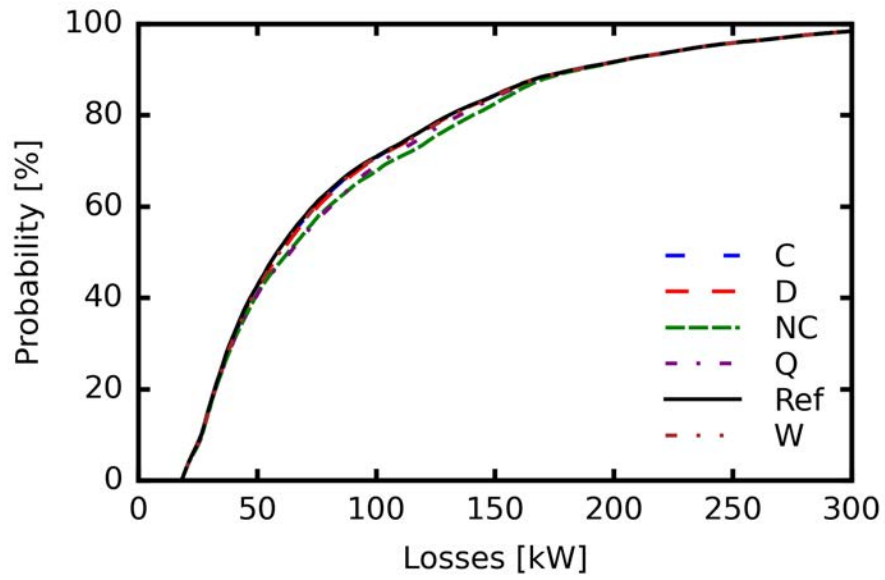
Since a substantial amount of data was employed in this study, including 259,200 minutes of active and reactive power measurements, the CDFs for final comparisons are based on the resulting simulation data directly rather than incorporating a statistical estimation procedure. It was found that none of the configurations offer substantial reduction in losses with respect to the NC case of no CBs considering loss reduction rarely exceeds 0.1% of the approximate 18MW total peak active power of KUs1 T2 (Fig. 2.25). This is in part due to the relatively high reactive power of loads and frequent reversal of flow back into the substation, which disables CBs from operation since they would only further contribute to this flow and a worsening power factor (Fig. 2.21). As illustrated in Fig. 2.26, considerable improvements are

realized in voltage stability. The Q configuration with 42% less total CB rating than Ref maintains operational compliance by remaining within the acceptable voltage range of 0.95pu and 1.05pu for almost 90% of the time, which is the same as all other configurations with CBs.

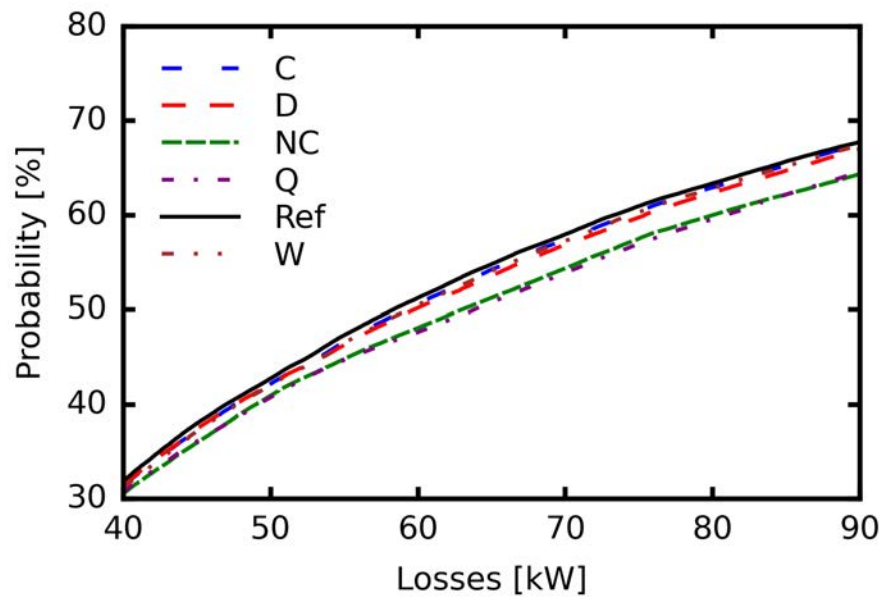
2.10 Summary

Multi-objective optimization for CB placement and rating of large-scale utility circuits is achieved through a multi-step Optimal Capacitor Planning (OCP) procedure developed through a comparison of methods, which include different formulations and optimization algorithms. The novel PA3 three-objective technique with both penalty constraint on voltage violations and automatic Load-Tap-Changing (LTC) transformer tap setting adjustment was determined to be the most effective. A solution selection method through a pseudo-weight vector approach that considers objective priority was developed and employed to determine the three most extreme cases of the KUs1 sub-circuits as well as an even compromise configuration. The efficacy evaluation for CB configurations over time in addition to the peak load scenario may be enabled by future enhanced load modeling methods as utilities deploy Advanced Metering Infrastructure (AMI).

Based on a systematic sub-circuit analysis of the selected configurations, significant improvements with respect to the base reference case were concluded. The T1 and T2 sub-circuits could be reconfigured to perform similar to the reference case with 70% and 42% less total installed CB rating, respectively. T2 was found to be most sensitive in voltage variation change and could be improved in this regard by up



(a)



(b)

Figure 2.25: CDFs of total active power losses for each circuit configuration in (a) full and (b) zoomed in views.

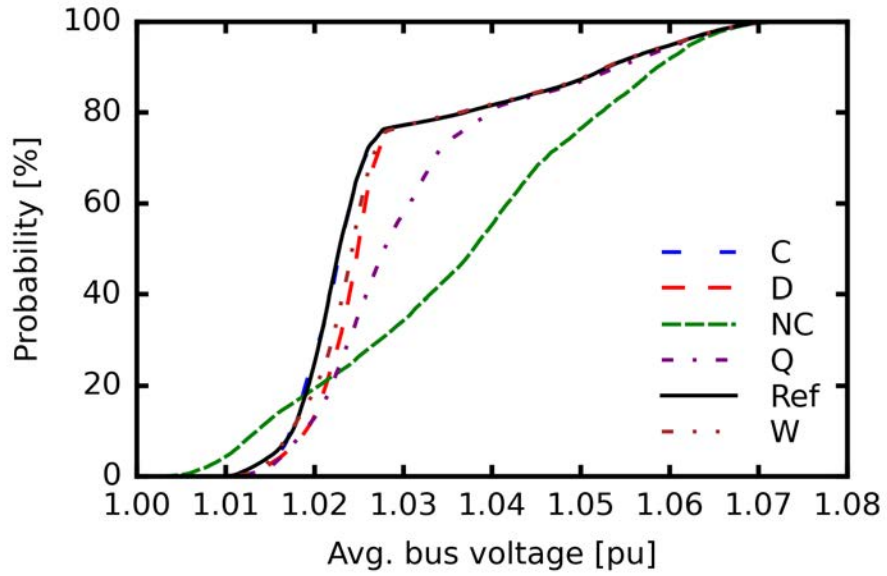


Figure 2.26: CDF for average bus voltage of each circuit configuration case.

to 63%. T3 was unique in that the reference case had a relatively low total installed CB rating and would require more investment to yield similar benefits in reduced power losses and voltage deviation as in T1 and T2.

Chapter 3

Optimal Operation of Voltage-Controlling Devices in Distribution Systems

3.1 Introduction and Main Problem

Power Distribution Systems (PDSs) experience constant change in load over time due to weather effects and occupant behavior. Voltage at individual buses change as well with an inverse relationship to corresponding loads. Therefore, voltage-controlling devices, including Capacitor Banks (CBs), Automatic Voltage Regulators (AVRs), and Load-Tap-Changers (LTCs) for transformers, are required to maintain operational compliance [24].

CBs are a popular reactive power compensating and power factor correcting technology that stabilizes bus voltages. They are typically employed at bus locations farther from the source bus due to more significant voltage drop. LTCs and AVRs are similar in their utility as they are conventionally placed to maintain voltage of feeders.

The improved control and management of such devices are currently of great interest for grid modernization and are typically associated with the concepts of Conservation Voltage Reduction (CVR) and Volt-Var Optimization (VVO) [3]. CVR has long been studied in PDSs and is now commonly considered as a function of VVO to cost-effectively reduce energy use and peak power [4]. Savings are realized

through CVR by operating within the lower half of the American National Standards Institute (ANSI) standard C84.1 recommended voltage band (114V-120V) without harming residential appliances or utility assets [26].

The evaluation of CVR and VVO effects may be performed through measurement and verification (M&V) methods that should consider load effects from typical causes, such as weather, time of day, and occupant behavior. Such M&V methods may be categorized as comparison, regression, or simulation-based [5, 26]. Comparison-based M&V utilizes two feeders of very similar configurations, topologies, and loads that are in close proximity to one another. CVR/VVO is applied to one, while the other feeder serves as a baseline. Although the most straightforward, finding two feeders that are similar enough is often not possible and external effects, such as weather, can be significantly different.

In regression-based implementations, loads are modeled as functions of impact factors, such as outdoor temperature. The linear regression models are solved over an example day with a reference voltage and with CVR applied. Simulation-based methods employ power system models that include the full network and connected loads. This enables simulated control of power system components with the challenge of considering voltage-dependency, which can be captured through constant impedance, constant current, and constant power (ZIP) modeling [23, 24, 27].

Various utility and national laboratory demonstrations of CVR/VVO have been performed through pilot programs and test cases of differing M&V types [5]. It has been determined based on such field implementations that PDS energy use may be reduced by 0.3% to 1.0% for every 1% of reduction in system voltage [6]. A

range of 1% to 4% in total energy use savings is expected based upon circuit-specific characteristics.

As smart grid technologies and Advanced Meter Infrastructure (AMI) become increasingly more prevalent in modern distribution systems, the improved control of these devices offers significant opportunity for savings in both energy use and costs due to equipment degradation. Extensive modeling for PDS networks, equipment, and loads, including their voltage dependency, enables the development and evaluation of advanced control methodologies through simulation-based M&V. Proposed in the following are both an optimal control case of best operational performance with unlimited adjustments to control settings that employs computational intelligence to perform CVR and VVO functions as well as an improved method that also considers equipment degradation by dispersing adjustments over time through machine learning clustering and day-ahead forecasting. The advanced control cases are compared with a baseline conventional case through exemplification upon an actual large-scale utility circuit model of approximately 2,000 nodes, henceforth referred to as circuit KUs1T1.

The main objective of this chapter is to develop a control optimization for voltage-controlling devices in PDSs to minimize both energy use and equipment degradation from setting adjustments over time. Independent variables are identified and include the settings of individual devices, including LTCs and CBs, as well as settings for the controller over time to leverage the expected trade off between the two main minimization objectives. Three control methods, which are illustrated in Fig. 3.9, are compared to evaluate effectiveness of the proposed cluster-based method.

This chapter is substantially based on the following journal publication: **E. S. Jones**, *et al.*, “A Cluster-based Method for Optimal Operation of Power Distribution Systems with Minimal Utility Asset Degradation”, 10p, 2023, *prepared for journal submission (April 2023)*.

The formulation presented includes the general methods proposed in: Y. Zhang, Y. Liao, **E. S. Jones**, N. Jewell and D. M. Ionel, “ZIP load modeling for single and aggregate loads and CVR factor estimation,” in International Journal of Emerging Electric Power Systems, vol. 23, pp. 839-858, 2022, doi: 10.1515/ijeeps-2022-0052.

In section 3.2, the modeling for the PDSs and associated loads as well as the method for time series simulation are established. Section 3.3 introduces a simulation case with conventional control of voltage-controlling devices to be employed as a baseline. Section 3.4 formulates and provides results for the optimal control method with unlimited setting adjustments to be considered as a benchmark case. The formulation and results of the improved control case that achieves best performance with consideration of equipment degradation are discussed in section 3.5. Having simulated three control cases, section 3.6 provides a comparative study and discussion with conclusions in section 3.7.

3.2 Time Series Power Distribution System Simulation with ZIP Load Modeling

A framework for the translation of actual large-scale PDSs from Synergi to OpenDSS [51], an open source circuit simulator provided by the Electric Power Research Institute (EPRI), was developed and applied to KUs1T1 by utilizing the OpenDSS Python

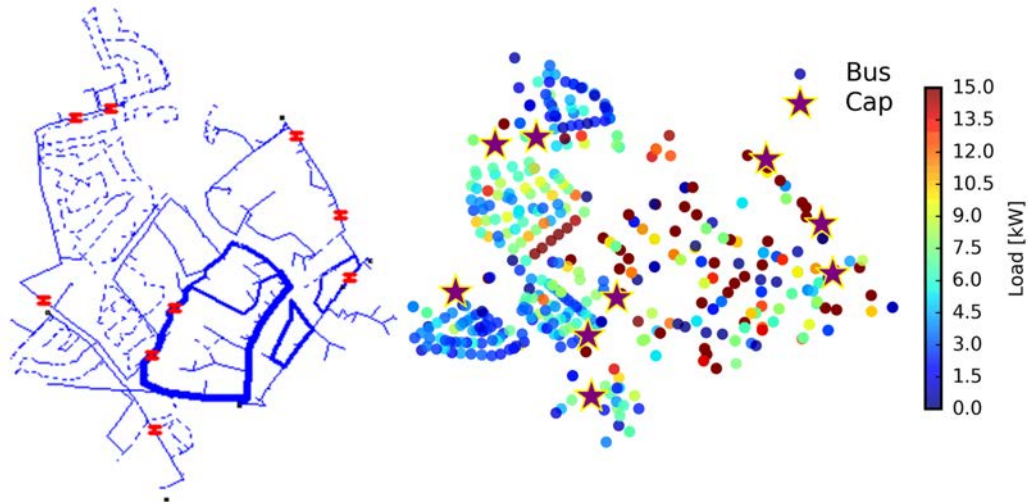


Figure 3.1: Circuit diagram of KUs1T1 with load at associated buses for an example time instance.

API (Fig. 3.1). Employing OpenDSS as the base simulation engine and accessing the model through the framework enables its use as a testbed for custom control and optimization methodologies. Components of the OpenDSS model, which originate from the Synergi version developed by the partner utility, include the network of lines, installation locations of devices, and specific definitions for equipment. The network lines are defined by their lengths, endpoint connection nodes, and sequences components. Extensive information for the substation transformer and nine three-phase capacitors is also explicitly defined.

The original load models are that of constant active and reactive power with the peak values experienced by the circuit based on historical data. Time series simulation is achieved by assuming each load experiences the same power-time profile, and by applying equivalent loadshape ratios for both active and reactive power that are based on measured data at the substation transformer. This ties simulation granularity to the timestep of available measured data, which is minutely for KUs1T1. To evaluate

Table 3.1: The simulation results for the reference case from the equivalent ZIP parameter estimation as well as for the minimum and maximum cases from the sensitivity analysis. Percent change for the latter two cases is also indicated with respect to the reference case.

Case	Reference	Minimum	Maximum
Active power [kW]	15,408	15,300 (-0.70%)	15,515 (+0.69%)
Reactive power [kvar]	3,079	2,992 (-2.83%)	3,165 (+2.79%)
Power losses [kW]	251	248 (-1.20%)	255 (+1.59%)
Avg. system-wide bus voltage [pu]	0.9675	0.9668 (-0.07%)	0.9681 (+0.06%)

control methodologies that leverage voltage to reduce energy use, either by reducing losses or the demand of loads, a more complex load model type is required to capture dependency of power upon voltage for certain residential loads. The ZIP load model is a popular method for capturing such voltage dependency [27, 63–65]. The individual ZIP load active and reactive power are respectively defined as:

$$p = p_0 \left[a_p \left(\frac{|v|}{v_0} \right)^2 + b_p \left(\frac{|v|}{v_0} \right) + c_p \right], \quad (3.1)$$

$$q = q_0 \left[a_q \left(\frac{|v|}{v_0} \right)^2 + b_q \left(\frac{|v|}{v_0} \right) + c_q \right], \quad (3.2)$$

where p is the active power demand of the load; a_p , b_p , c_p , the first, second, and third ZIP parameters that must sum to 1; $|v|$, the voltage magnitude; v_0 , the base voltage; q , the reactive power demand of the load; a_q , b_q , c_q , the fourth, fifth, and sixth ZIP parameters that must also sum to 1.

Equivalent ZIP load parameters for KUs1T1 were determined based on measured data from the substation transformer, and each individual load model was updated to the ZIP type. To determine the degree of effect on circuit model accuracy from possible estimation error of ZIP parameters, a parametric sensitivity analysis was

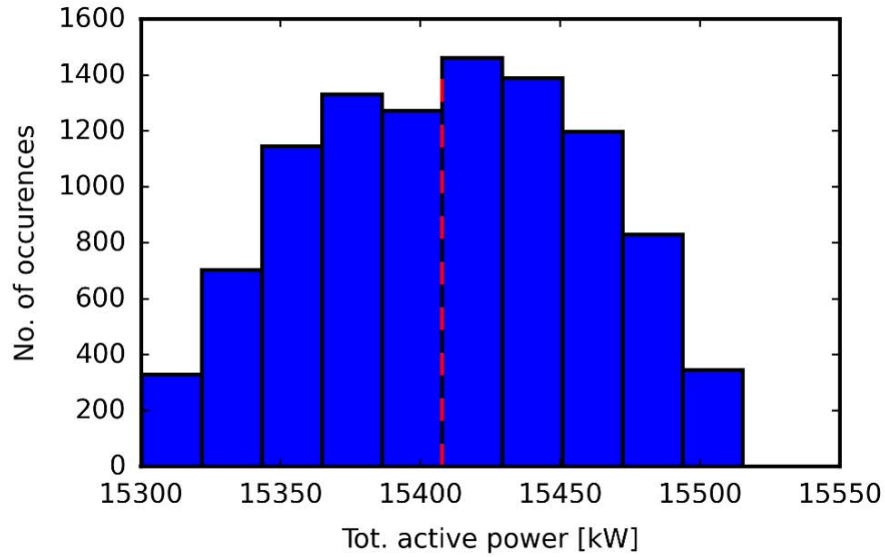


Figure 3.2: Sensitivity analysis results of all 10,000 simulation case in term of total active power.

performed. Ten thousand sets of all six ZIP parameters were randomly generated within a range of $\pm 15\%$ in increments of 1% from the reference estimation values. The analysis results, provided in Table 3.1 and illustrated in Fig. 3.2, show that the estimation methodology is relatively very stable in that the most extremely erroneous cases yielded resulting simulation changes of only 0.06% to 2.83%.

The assumptions that the individual loads would experience the same load profile and have the same ZIP parameters limits the accuracy for the time series simulation and voltage dependencies to the substation transformer level. As AMI meters are deployed and data for individual loads becomes available, this time series circuit simulation testbed may be updated to employ individual time-power profiles. Additionally, voltage dependency of each individual load may be captured through the ZIP parameter regression method utilized in this work, or by machine learning model training directly upon the measured data.

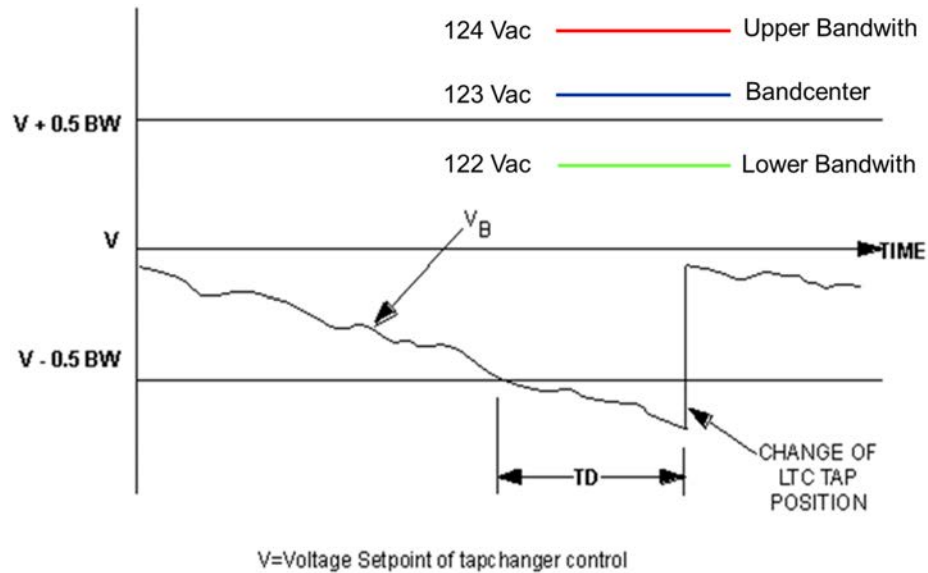


Figure 3.3: Conventional control of LTC transformer taps from Beckwith Electric technical documents [1].

3.3 Baseline Case with Conventional Controls

The KUs1T1 PDS is a sub-circuit of a larger system and is fed from a single substation transformer. This transformer is outfitted with an LTC, and the sub-circuit contains nine CBs throughout as illustrated in Fig. 3.1. The baseline case with conventional control is simulated over an example summer day based on minutely active and reactive power data that is applied as ratios with respect to peak load. For equivalent comparison, the following control cases are simulated in the same way.

Conventional control is enacted by adjustment of LTC tap settings and CB on/off status based on typical control practices provided by the partnering utility [1]. Traditionally, LTCs operate based on four primary settings: voltage setpoint, block raise, block lower, and a time delay to reduce unnecessary adjustments caused by brief transients. As voltage at the bus monitored by the LTC deviates from the setpoint,

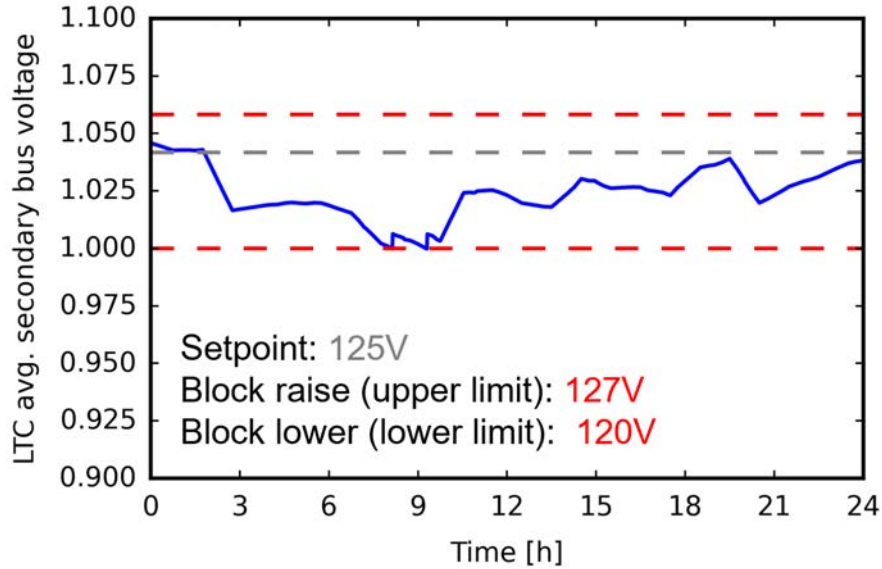


Figure 3.4: Bus voltage at the secondary side of the KUs1T1 LTC transformer with simulated conventional control.

the tap setting will be adjusted within a discrete range of -32 to 32 taps, which corresponds to ± 0.1 pu voltage in increments of 0.003125pu. As shown in Fig. 3.3, if voltage exceeds either the upper or lower limits for longer than the time delay, which is usually thirty to sixty seconds, tap adjustment occurs.

The simulation results for the KUs1T1 under conventional control are provided in Fig. 3.4 with resulting voltage at the LTC-monitored bus and specific limits for the circuit. With a time delay of thirty seconds, two tap adjustments occur as voltage dips below the lower limit between 7:00-11:00. Based on data from the partnering utility, the typical number of LTC operations per day for a circuit like KUs1T1 is 7.5 on average and can peak to 25.

Conventional control of switchable CB follows a trip/close logic. For KUs1T1, a trip limit of 1.05pu and close limit of 1.00pu are applied for all nine CBs. The resulting simulation results of voltages at the bus monitored by these CBs are provided in Fig.

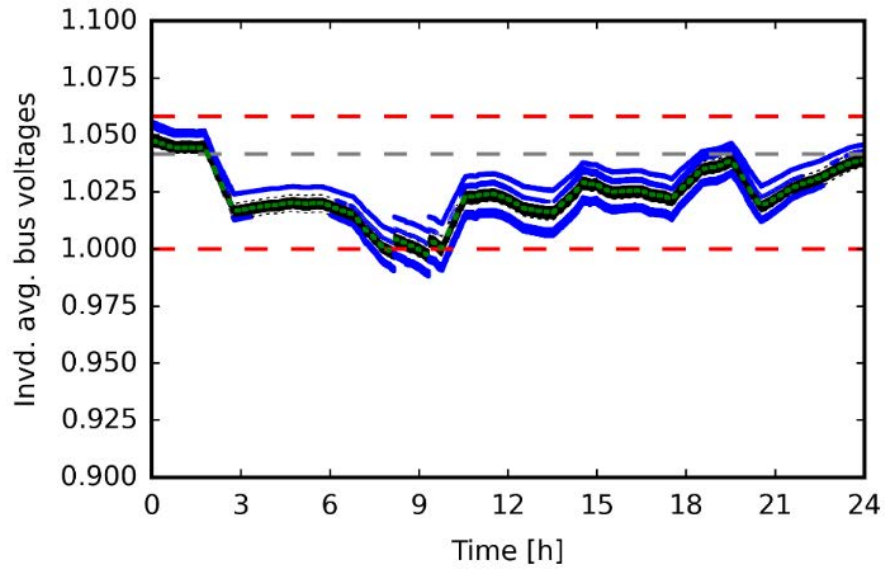


Figure 3.5: Conventional control simulation results with voltage for each individual bus in KUs1T1.

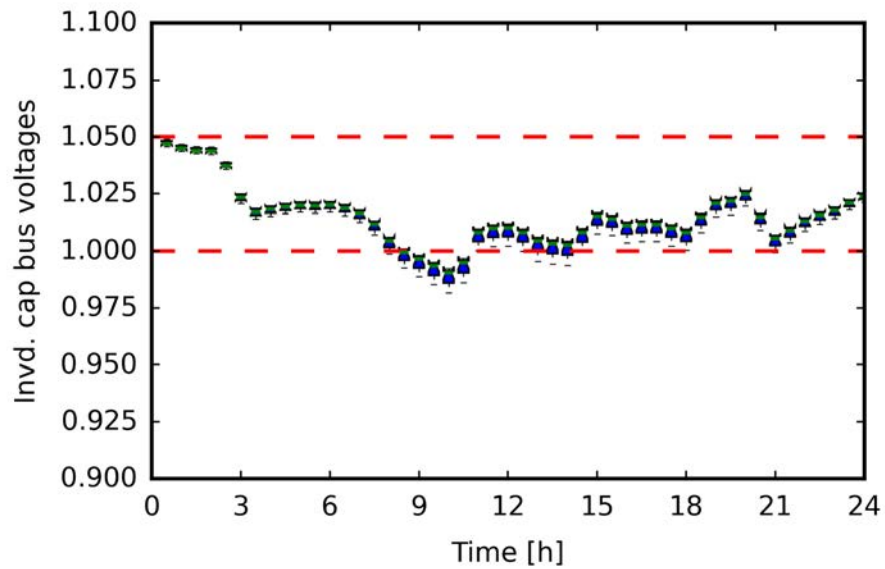


Figure 3.6: Individual bus voltages monitored by the nine CBs of KUs1T1 for switching control.

3.6. Since all CBs were assumed to be closed upon initialization and the voltages remain beneath the trip limit, no CB adjustments occur during the example day.

The results in terms of individual bus voltages in Fig. 3.5 illustrate well the limitations of conventional control strategies, as voltages must operate in the upper half of the acceptable 0.95pu to 1.05pu range to avoid violations. Monitoring only the bus near the LTC for tap adjustment requires a higher block lower setting to account for voltage drop throughout the circuit as it is very close to the source bus. Opportunity for savings exists through CVR and VVO functions, which glean energy use by reducing system-wide voltage and intelligently controlling devices to maintain operational compliance. The effectiveness of CVR and VVO depends upon the voltage dependency of residential loads, which contributes to the importance of accurate ZIP modeling as discussed in section 3.2.

3.4 Best Performance Case with Optimal Operation and Unlimited Adjustments

Through the circuit simulation testbed discussed previously in section 3.2 and chapter 2, optimization of control for voltage-controlling devices is achieved with utilization of the non-dominated sorting genetic algorithm II (NSGA-II) [58]. The optimization is formulated for a single simulation timestep t with the objective of minimizing total distribution system active power ($p_{a,t}$) at that moment, including network losses (w_a) and load demand ($p_{a,d,t}$), which is formally defined as:

$$\min \left[p_{a,t} = \sum_{i=1}^{n_l} (w_{a,l,t,i}) + \sum_{j=1}^{n_x} (w_{a,x,t,j}) + \sum_{k=1}^{n_d} (p_{a,d,t,k}) \right], \quad (3.3)$$

where n_l is the total number of lines; $w_{a,l,t,i}$, the active power losses at time t over line number i ; n_x , the total number of transformers; $w_{a,x,t,j}$, the active power losses at time t over transformer number j ; n_d , the total number of loads; $p_{a,d,t,k}$, the active power demand at at time t for load number k .

Targeting $p_{a,t}$ as the only minimization objective accounts for the trade-off that can occur between reduction in $w_{a,t}$ and voltage-dependent $p_{a,d,t}$ based on the ZIP parameters of the circuit model. The independent variables include the trip/close settings for the nine switching CBs and the LTC tap setting that may be within a discrete range of -32 to 32. A constraint is built into the optimization that imposes a five-minute time limit for CBs after a trip command to ensure full discharge before the next close command. Another constraint is incorporated that penalizes designs with bus voltages below a provided minimum target voltage ($v_{t,m}$).

During time series simulation, this optimization is called every timestep after the application of the load profile scalars and ZIP parameters. The optimal LTC tap settings and trip/close statuses of the CBs for that moment are then determined and applied. The $v_{t,m}$ is set to be a constant 0.975pu to account for secondary voltage drop over distribution transformers. Since calling the optimization every timestep in this control case leads to purposefully unlimited adjustments, the devices of KUs1T1 receive control commands on a minutely basis to ensure minimum power and number of violations of the $v_{t,m}$ limit.

Aspects of the resulting optimal designs and allowed number of generations for the NSGA-II to run were compared to determine the best setting for solution quality and total simulation time (Fig. 3.7). Running the optimization for all 1440 timesteps

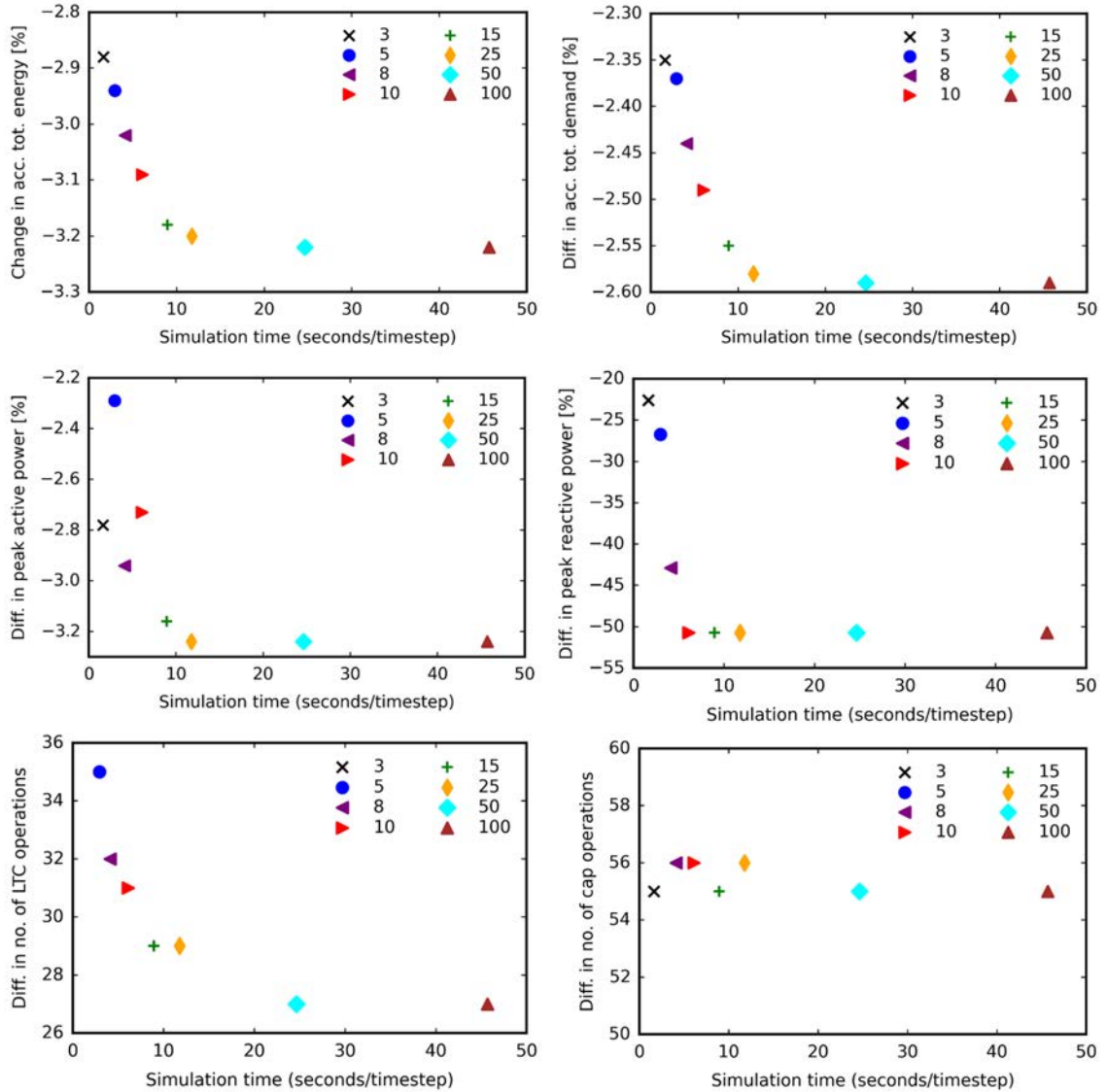


Figure 3.7: Solution quality of various PDS characteristics and simulation time at different allowed no. of generations as indicated by the legend for the control optimization with unlimited adjustments. The simulation results are determined for an example day with respect to another simulation of no control.

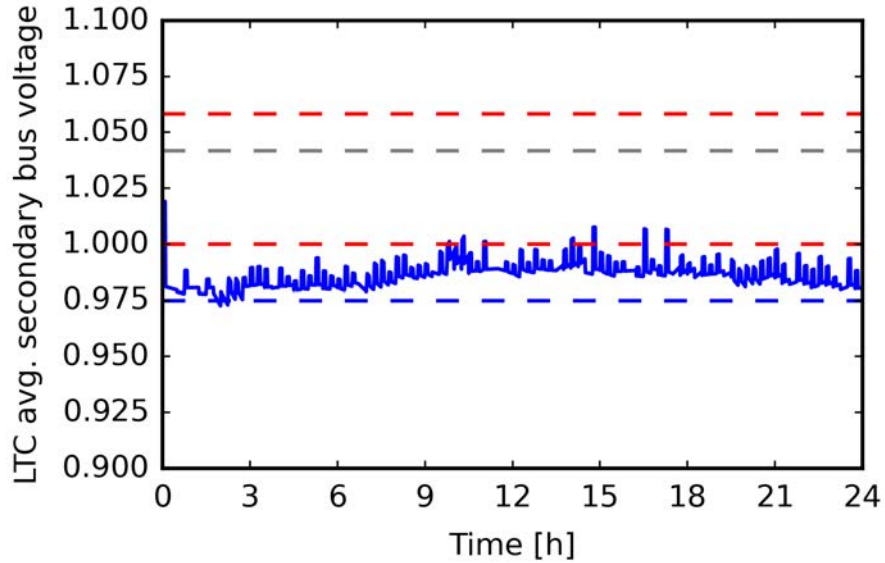


Figure 3.8: Final LTC voltage results having run the control optimization with 20 generations for every timestep and with no limits to adjustments aside from the built-in CB discharge time limit.

over the simulated day at a setting of 20 generations was accepted to be the point of “best compromise” by considering the change in total energy as the highest priority. Resulting optimal operation with unlimited adjustments, which is shown through the LTC voltage in Fig. 3.8, reduces total energy use over the day from 229.85MWh to 226.85MWh, which is a reduction of 1.3% and is in-line with expectations based on review of relevant literature and previous implementations.

3.5 New Cluster-based Method for Improved Optimal Controls

To achieve similarly optimal performance while also considering equipment degradation by limiting the number of device adjustments, a new method for improved optimal control is proposed (Fig. 3.9). This improved control case employs machine learning and load forecasting to disperse operations over time such that the PDS performs optimally and adjustment frequency is minimized. A k-means clustering

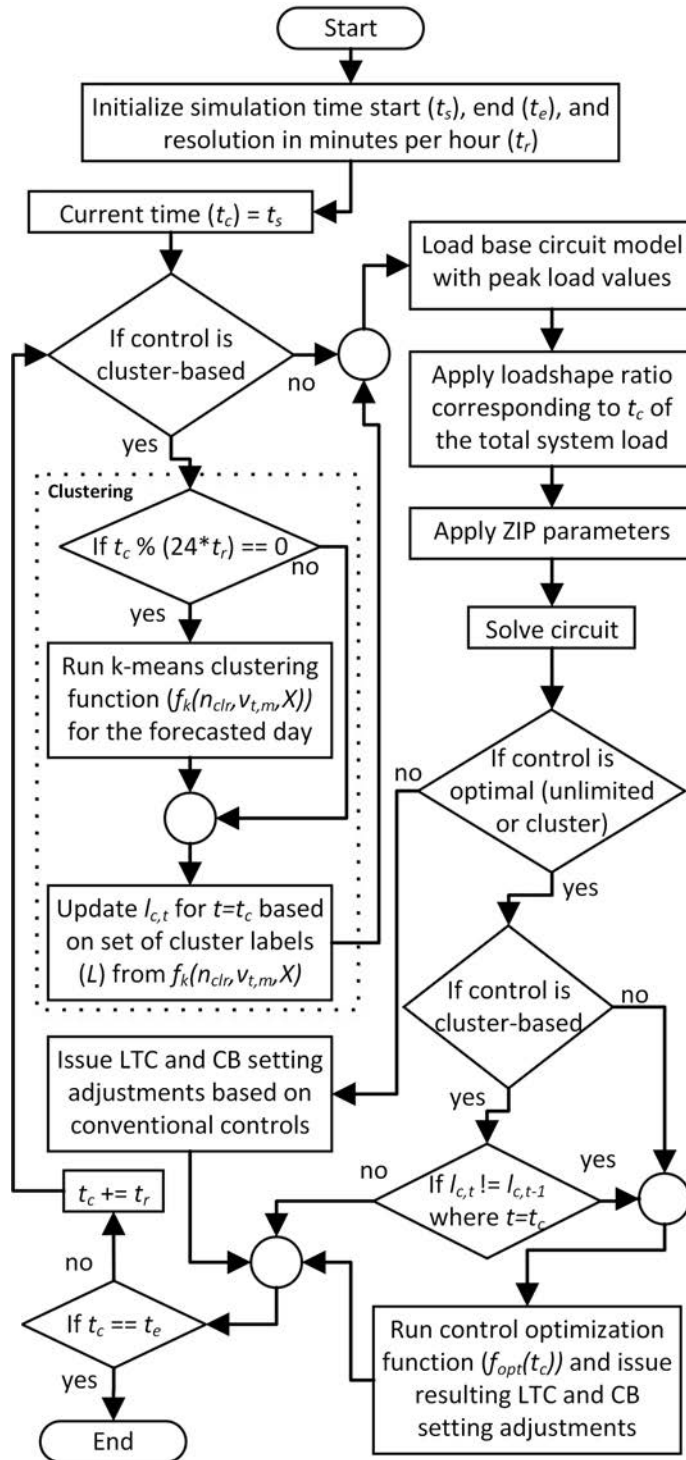


Figure 3.9: Flowchart of time series PDS simulation with ZIP load modeling and the three considered control types.

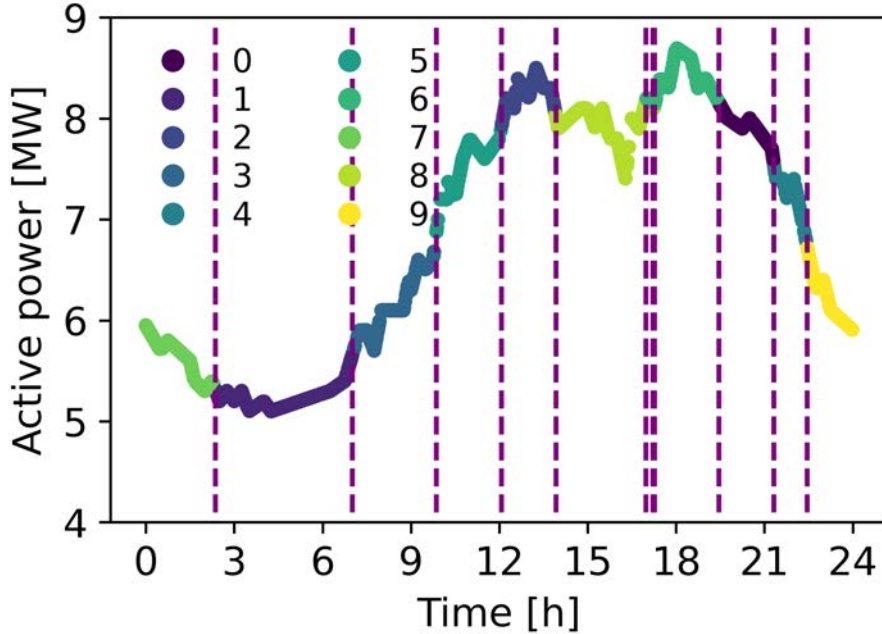


Figure 3.10: The example day time-load profiles measured minutely at the substation transformers for KUs1T1 with the clusters of time most similar in total power determined by the machine learning K-means clustering algorithm.

algorithm is employed to determine periods of time that are most similar to each other in terms of total PDS power. The algorithm partitions n_o observations into n_k , which must be less than or equal to n_o , sets such that the variance of each cluster set K_i is minimized. This objective is formally defined by:

$$\min \left[\sigma_{k,t} = \sum_{i=1}^{n_{clr}} \left\{ \sum_{x \in K_i} (\|x - \mu_i\|^2) \right\} \right], \quad (3.4)$$

where n_{clr} is the number of k-means clusters to determine; x , the observation elements of cluster set K_i ; μ_i , the mean of the observation values in cluster set K_i .

Assuming that control settings remain optimally applicable for all timesteps within each of the resulting clusters, adjustments are then only required once per cluster. The application of clustering creates another opportunity for optimization with multiple

objectives, including the minimization of total day energy use e_d as well as total number of device adjustments n_{adj} and voltage violations n_{vio} , which are formally defined as:

$$\min \left[e_d = \sum_{i=1}^{n_t} (p_{a,t}) \right], \quad (3.5)$$

$$\min \left[n_{adj} = \sum_{i=1}^{n_t} \left\{ \sum_{j=1}^{n_{ltc}} (n_{ltc,i,j}) + \sum_{k=1}^{n_{cap}} (n_{cap,i,k}) \right\} \right], \quad (3.6)$$

$$\min \left[n_{vio} = \sum_{i=1}^{n_t} \left\{ \sum_{j=1}^{n_b} (n_{vio,i,j}) \right\} \right], \quad (3.7)$$

where n_t is the total number of timesteps; n_{ltc} is the total number of LTCs; $n_{ltc,i,j}$, the total number of tap adjustments for time i at LTC j ; n_{cap} , the total number of CBs; $n_{cap,i,k}$, the total number of switching adjustments for time i at CB k ; n_b is the total number of buses; $n_{vio,i,j}$, the total number of voltage violations for time i at bus j , which can only be 0 or 1;

The number of clusters (n_{clr}) for the k-means algorithm to determine is an independent variable for the optimization and has a discrete range of 2 to 25. The $v_{t,m}$ setting is no longer considered constant as in section 3.4 and is adapted to be another independent variable with a discrete range of 114V to 120V in 0.1V increments. The n_{clr} and $v_{t,m}$ are directly associated with the objectives defined in 3.6 and 3.7 as n_{clr} determines when the optimization to minimize is called and $v_{t,m}$ sets how low the per-cluster optimization is to reduce PDS bus voltages.

When the per-cluster optimization in this improved control case is called, the

objective defined in 3.3 is updated to be the average total PDS power for each of the timesteps within the corresponding cluster ($p_{\mu,c}$), which is defined as:

$$\min \left[p_{\mu,c} = \frac{\sum_{i=1}^{n_{t,c}} (p_{a,i})}{n_{t,c}} \right], \quad (3.8)$$

where $n_{t,c}$ is the total number of timesteps within cluster c ; $p_{a,i}$, the total distribution system active power at time t . This updated objective improves applicability of the issued adjustments for the entire time period.

Having formulated the optimization problem to determine best settings for the cluster-based control method, 1,380 simulations were performed based on the control setting combinations established by the independent variable ranges, which include 23 and 60 different n_{clr} and $v_{t,m}$ options, respectively. Though the problem formulation is an opportune application of computational optimization, an algorithm was not applied and results for each possible case were produced since each simulation required only 0.5s to complete with parallel processing. The set of simulation results allows for the determination of relationships between the input control settings of n_{clr} and $v_{t,m}$ and resulting objective evaluations, which include e_d from 3.5, n_{adj} from 3.6, and $n_{vio,a}$, which is n_{vio} from 3.7 averaged over the day.

From the simulations, design inputs of n_{clr} and $v_{t,m}$ may be compared with resulting e_d as illustrated in Fig. 3.11. It is evident that lower $v_{t,m}$ directly correlates to lower e_d , whereas n_{clr} produces minimal improvement, which is in-line with expectations. The n_{clr} setting influences n_{adj} for both LTCs and CBs and prevents increased n_{vio} for cases of lower $v_{t,m}$ that enable improved e_d reduction. This effect, shown in Figs. 3.12 and 3.12, is most evident when comparing cases with n_{clr} of less than 11

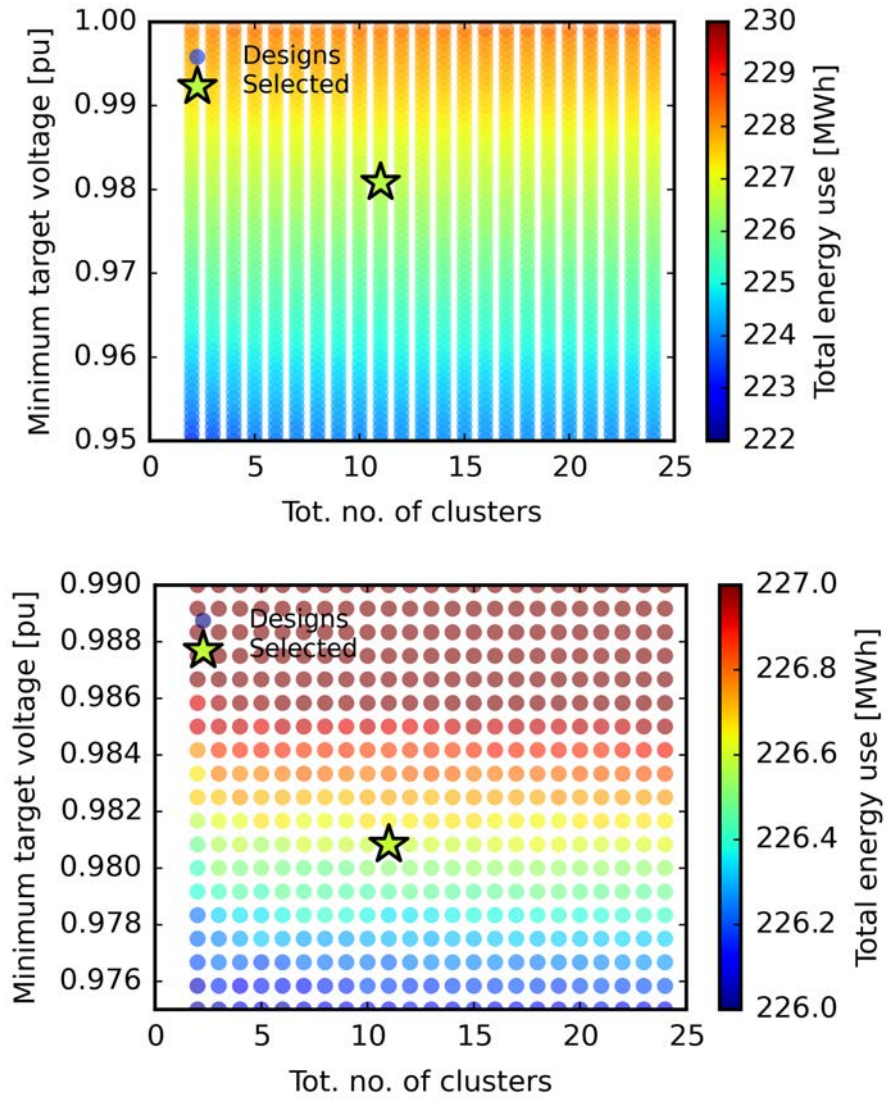


Figure 3.11: Relationship between results for (top) total energy use and the control settings n_{clr} and $v_{t,m}$ over the example day for KUs1T1 with a (bottom) zoomed view of the case with the best selected settings.

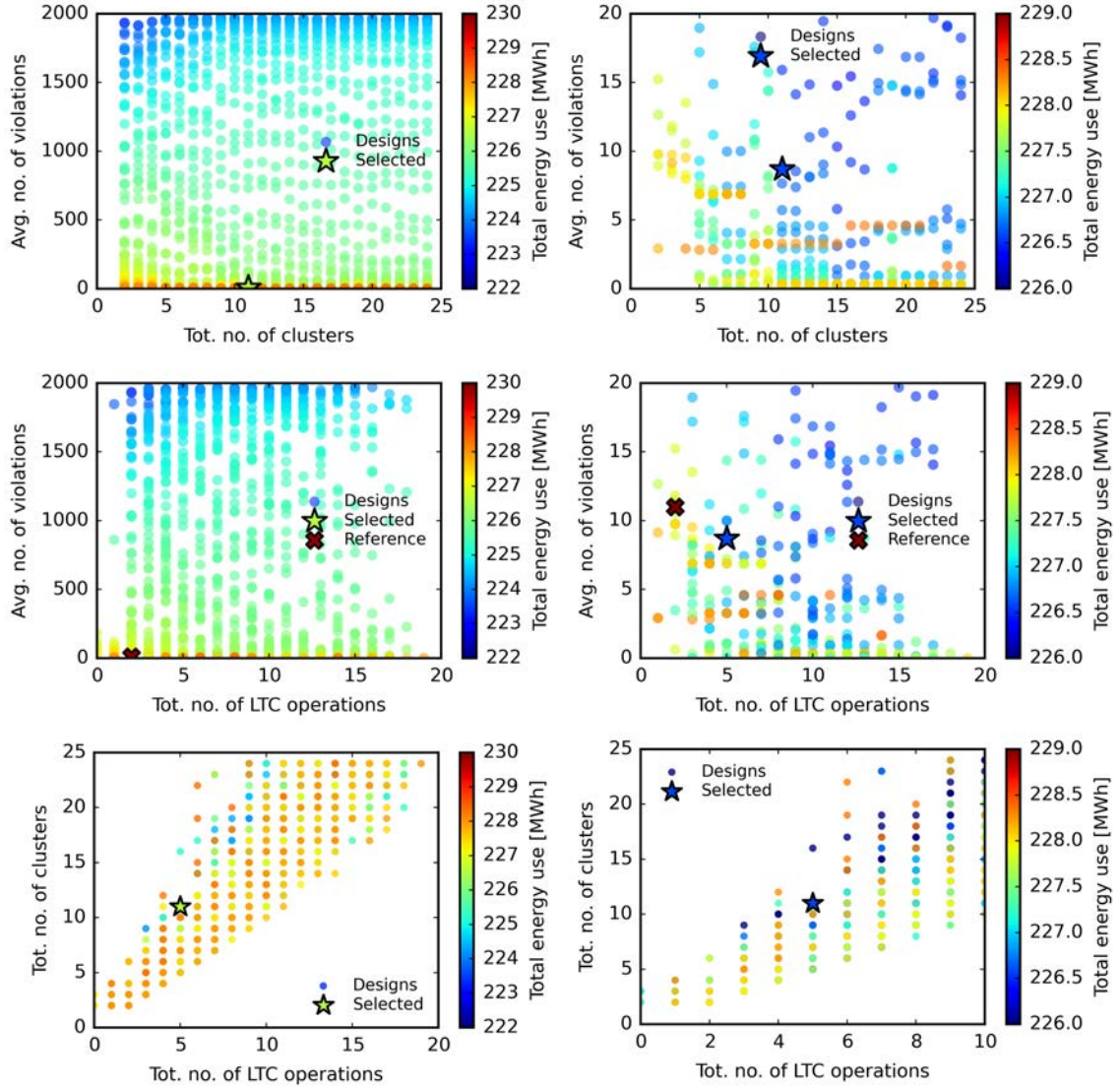


Figure 3.12: Relationship between n_{clr} and resulting e_d , n_{adj} for LTC taps only, and $n_{vio,a}$ over the example day for KUs1T1 with (left) full-scale and (right) zoomed views. Although n_{clr} does not directly correlate to e_d as $v_{t,m}$ does, a minimum n_{clr} of around 11 is required to access cases with much lower e_d and $n_{vio,a}$ of less than 11.

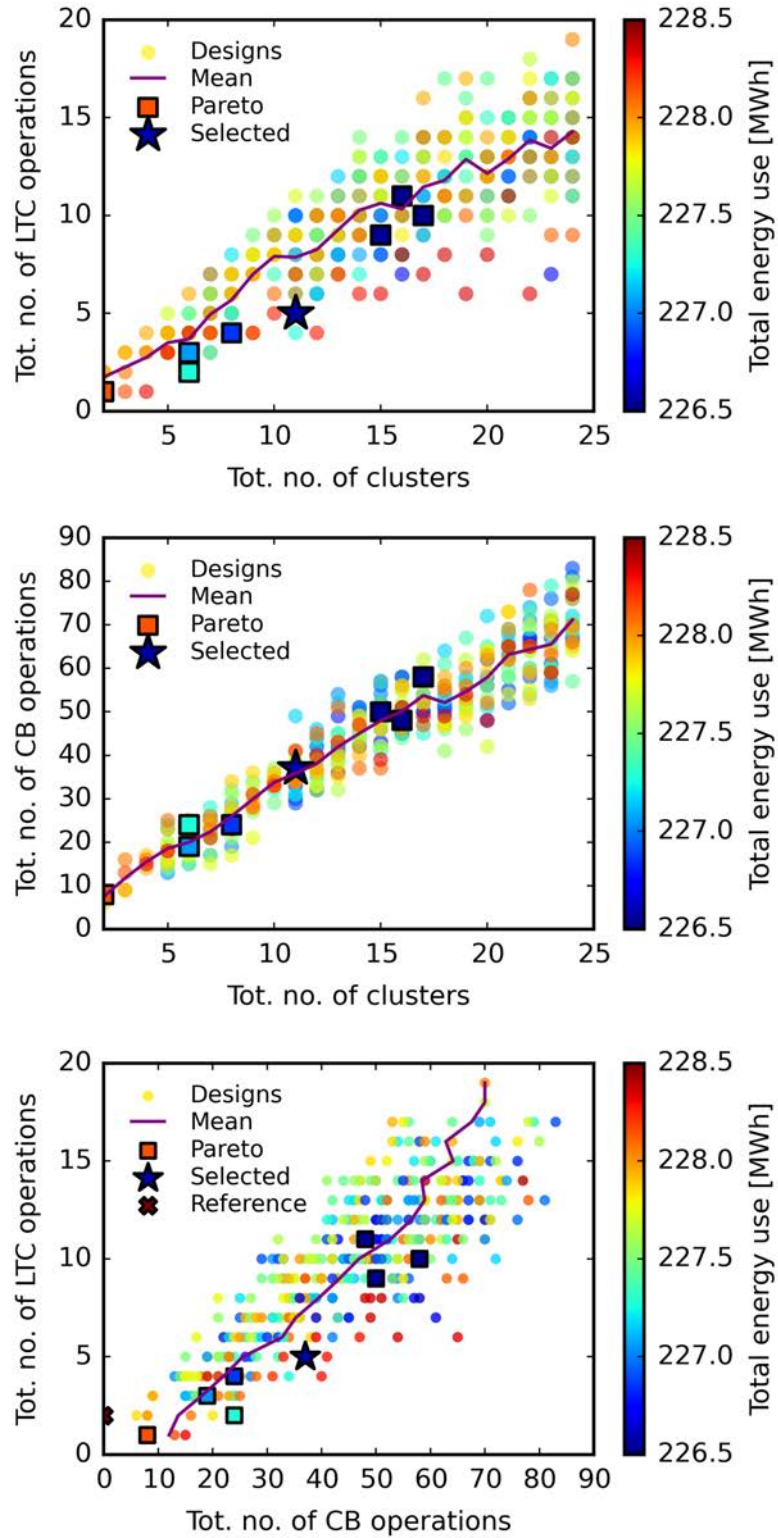


Figure 3.13: Relationships between control setting n_{clr} and resulting n_{adj} for LTCs and CBs. Increased n_{clr} correlates to increased mean and variance of n_{adj} for LTCs and CBs. For designs with greater than 60 CB n_{adj} , CB unavailability is observed due to more frequent timer activation.

and cases with n_{clr} greater than or equal to 11. Those with less than 11 are unable to enact enough n_{adj} to accommodate lower $v_{t,m}$ settings without high n_{vio} .

It may also be observed that greater “operational freedom” from higher n_{clr} does not necessarily elicit lower e_d past approx. 10 LTC n_{adj} (Fig. 3.14). As illustrated in Fig. 3.13, the relationship between LTC n_{adj} and CB n_{adj} becomes less linear for cases of greater than approx. 60 CB n_{adj} . At this point, CBs start to become unavailable due to the more frequent activation of the built-in five-minute timer. CB unavailability can disallow lower $v_{t,m}$ with acceptable n_{vio} that is achieved by lower LTC tap settings that may rely upon CBs to prevent n_{vio} in especially low voltage regions.

With the 1,380 simulated combinations of n_{clr} and $v_{t,m}$, best settings are determined through a selection procedure. The first step is to limit the pool of designs to those with very few $n_{vio,a}$. To select settings for KUs1T1, only the 409 designs with less than or equal to 10 $n_{vio,a}$ were considered based on typical performance with conventional control that is discussed further in section 3.6.

From the remaining pool, a Pareto front of best designs is then calculated based on a non-dominated sorting of the objectives to minimize e_d and n_{adj} as shown in Fig. 3.14. This step further reduces the number of possible settings to 8 optimal designs. From this point, the best setting is dependent upon objective priority by the utility as the Pareto front represents a trade-off between the two objectives. For example, circuit specific cost ratios in units of \$/kWh and \$/adjustment may be applied to determine the cheapest option in terms of economic costs, or e_d may be weighed more heavily with n_{adj} having some maximally acceptable limit to avoid increased

Table 3.2: Simulation results for the four considered control cases.

Control case	Conv.	Opt. w/ unlmted. adjmts.	Opt. cluster w/ example settings	Opt. cluster w/ best settings
Tot. energy [MWh]	229.85	226.85	228.63	226.59
Tot. losses [MWh]	2.82	2.56	2.60	2.51
Tot. load [MWh]	227.02	224.30	226.03	224.08
Peak active power [MW]	13.41	13.28	13.34	13.24
Peak reactive power [Mvar]	7.39	3.98	6.63	7.00
Avg. no. of voltage violations	11.37	3.84	0	8.67
Tot. no. of LTC adjmts.	2	543	6	5
Tot. no. of CB adjmts.	0	1,417	33	37

equipment degradation.

In this case, the design with the e_d at the most reasonable resulting n_{adj} was selected having n_{clr} at 11 and a $v_{t,m}$ of 0.981pu. Compared to an example cluster-based improved optimal control case having example settings of 10 n_{clr} and 1.0pu $v_{t,m}$ inspired by the conventional control case, the method yields 169% more reduction in e_d and 76% fewer $n_{vio,a}$ with settings optimization. As illustrated in Fig. 3.15 for the case with optimal settings, the individual bus voltages remain just above the 0.975pu minimum and has enough clusters to ensure tap adjustments are available such that excessive $n_{vio,a}$ does not occur without having to operate at higher voltages as in the 15:00-18:00 time period for the case with example settings.

3.6 Comparative Studies and Discussion

Four cases based on three control methods were simulated over an example day at a minutely timestep for the KUs1T1 circuit, including conventional, optimal with

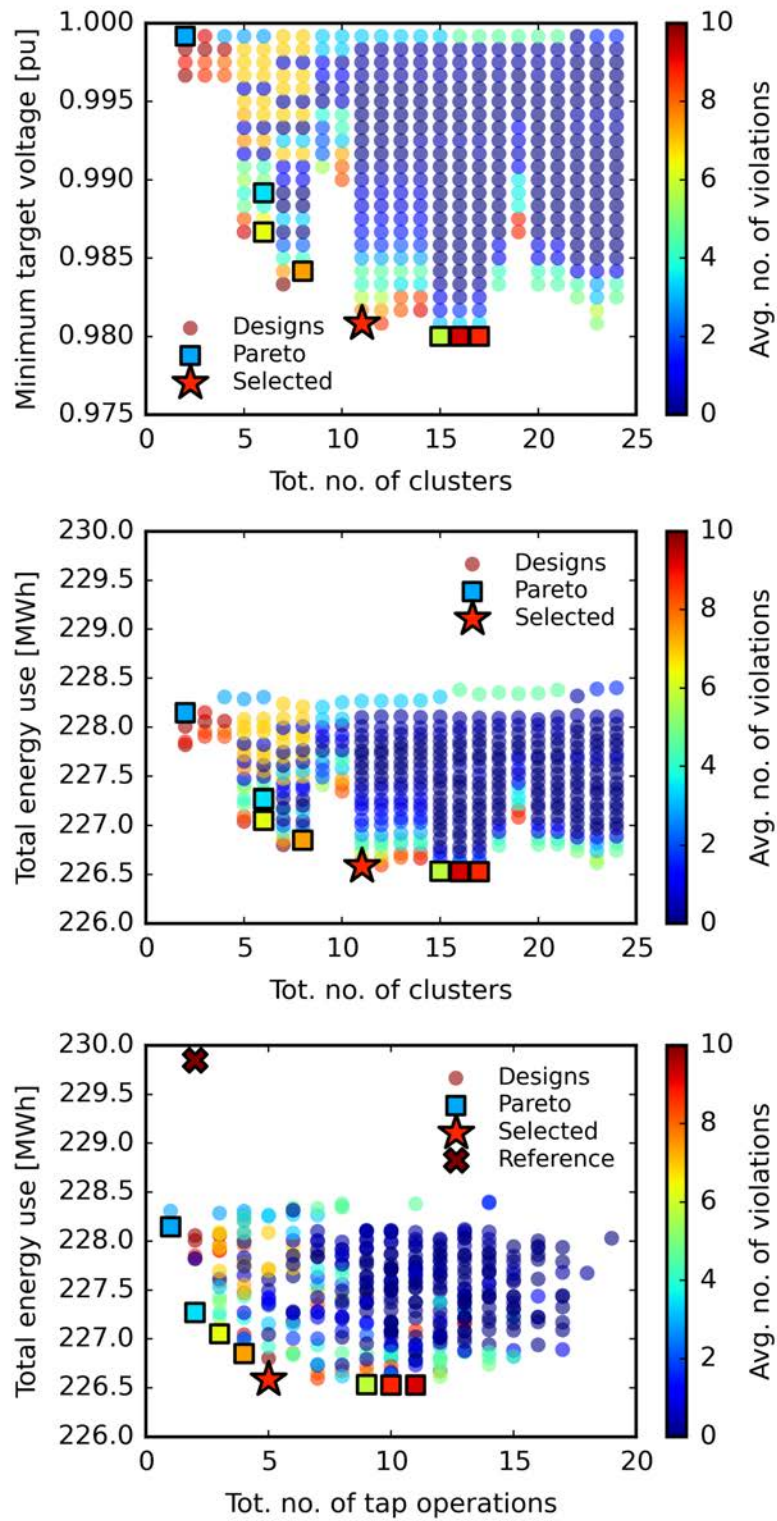


Figure 3.14: Resulting $n_{vio,a}$, e_d , and n_{adj} from different input control setting combinations of n_{clr} and $v_{t,m}$ for the 409 designs with less than or equal to 10 $n_{vio,a}$ along with the calculated Pareto front of 8 best designs and selected case.

Table 3.3: Resulting percent changes [%] for the control cases with respect to the conventional case.

Control case	Tot. energy	Tot. losses	Tot. load	Peak active power	Peak reactive power
Optimal w/ unlimited adjmts.	1.30	9.28	1.20	0.96	46.09
Optimal cluster-based w/ ex. settings	0.53	7.97	0.43	0.50	10.23
Optimal cluster-based w/ best settings	1.42	11.06	1.29	1.22	5.20

unlimited adjustments, and improved cluster-based optimal that has limited adjustments with both example and best control settings. The results of these simulations are illustrated in terms of individual bus voltages in Fig. 3.15 to illustrate how the controls affect the entire PDS over time. To evaluate effectiveness of the control methods, performance metrics related to objectives defined in sections 3.4 and 3.5, including e_d , $n_{vio,a}$, and n_{adj} for both LTCs and CBs separately, are provided in Table 3.2 as well as changes with respect to the conventional control case in Table 3.3.

The optimal case with unlimited adjustments yielded improvements of 1.30% in e_d with only 3.84 $n_{vio,a}$, which is less than that of the conventional 11.37 $n_{vio,a}$. This case is considered only as a benchmark though for best possible theoretical performance as adjustments are allowed for every timestep without limit, which results in excessive n_{adj} for LTCs and CBs. To achieve similar optimal performance without increasing equipment degradation compared to the conventional case by intelligently dispersing adjustments throughout the day, the improved cluster-based method is employed.

With example control settings of 10 n_{clr} and 1.0pu $v_{t,m}$ inspired by the conventional case, the cluster-based improved optimal method reduces e_d by 0.53% with 0 $n_{vio,a}$ due to the relatively high 1.0pu $v_{t,m}$. By optimizing these settings and changing them to 11 and 0.981pu, respectively, e_d reduction surpasses all other control cases at 1.42%

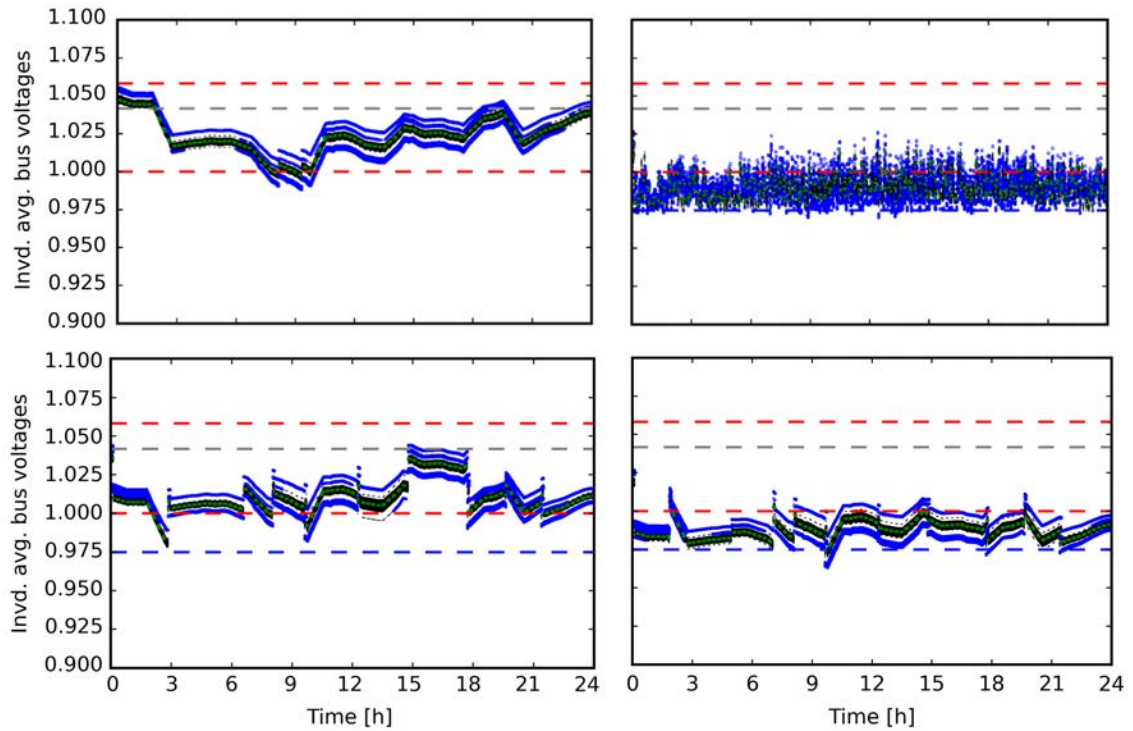


Figure 3.15: Comparison of control methodologies for KUs1T1 by individual bus voltages every simulation timestep, including the cases of conventional (top left), optimal with unlimited adjustments (top right), and improved cluster-based optimal that has limited adjustments with both example (bottom left) and best control settings (bottom right).

while still remaining beneath the conventional $n_{vio,a}$ at only 8.67. The ability to finely tune the settings n_{clr} and $v_{t,m}$ enables lower e_d by reducing $v_{t,m}$ until an acceptable limit for $n_{vio,a}$ is reached.

A minimum bus voltage of 0.975 was assumed to account for possible secondary voltage drop over distribution transformers as the employed circuit models capture only down to the primary side. The additional drop over the transformer and proceeding lines connected to customer loads can be added into the models, which could enable even lower $v_{t,m}$ and, therefore, more improvement in e_d reduction. Severity of voltage drop is dependent upon the length of the secondary side line, amount of load experienced, the transformer kVA rating, and distance from the source bus. These dependencies may be incorporated in future work either in OpenDSS models themselves or within the testbed simulator based on more generalized data provided by the utility. Additional studies to explore the effects of Distributed Generation (DG) [66] and the increasing prevalence of appliances with power electronics on CVR and VVO functions would also be of great interest and are possible through the circuit simulating testbed.

3.7 Summary

A comparative study of different Power Distribution System (PDS) control methods that employ voltage-controlling devices, including Capacitor Banks (CBs) and Load-Tap-Changing (LTC) transformers, was performed. The study was enabled by a time-series circuit simulation testbed and exemplified upon a comprehensive model of an actual 2,000-node utility PDS that captures load demand voltage-dependency

through an equivalent constant impedance, constant current, and constant power (ZIP) representation.

Included in the study were cases of conventional, best performance without limit to setting adjustment, and cluster-based optimal performance with dispersion of adjustments over time through load-forecasting. It was concluded that the new cluster-based control method achieved optimal performance with a total energy use reduction (e_d) of 1.42% while also minimizing equipment degradation by the tuning of control settings, which include number of clusters (n_{clr}) and minimum target voltage ($v_{t,m}$), such that number of CB and LTC adjustments (n_{adj}) and voltage violation ($n_{vio,a}$) are traditionally acceptable.

Chapter 4

Electric Power and Energy for Smart Buildings

4.1 Introduction and Main Problem

Improved Heating, Ventilation, and Air-Conditioning (HVAC) system and building technologies can considerably reduce total building energy use and enable Demand Response (DR) control, offering significant opportunity for savings and enhanced community-wide load malleability in Virtual Power Plant (VPP) scenarios. To simulate and study such scenarios at both the individual load and aggregated power system levels, controllable models of HVAC energy that sufficiently capture effects from weather are required.

To comprehensively model an HVAC system, it is necessary to consider the building within which it operates and its associated thermal loads. The link between HVAC systems and corresponding buildings is due to the significant relationship between HVAC system energy usage and the thermal behavior of the building, which is influenced by the local climate and the building's construction. EnergyPlus, a white-box, physics-based whole building energy simulation program was employed as a solution to simulate both indoor temperature and HVAC energy use.

The total energy usage of different appliances and end-user consumption share by different house types were also analyzed for insight into the energy makeup of

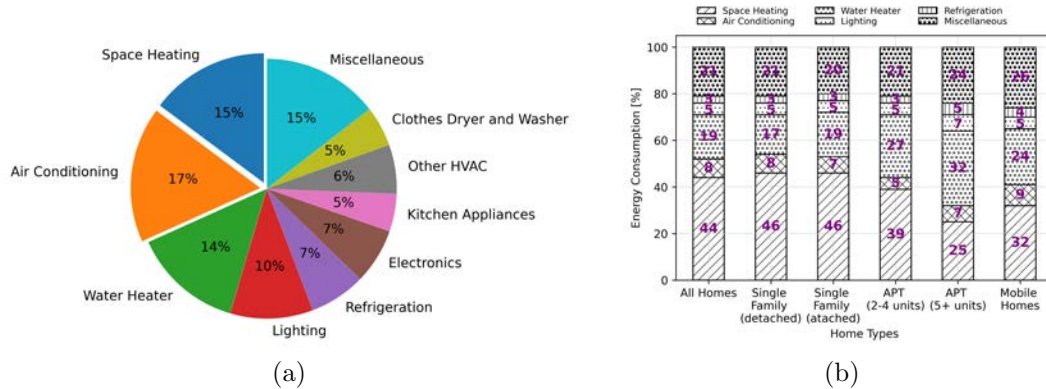


Figure 4.1: Residential energy use survey results for 2015 provided by the U.S. Energy Information Administration. Provided are (a) annual energy use by different appliances of a typical residential building in the U.S. and (b) end-user energy use distribution by different types of U.S. homes. Energy use excludes the losses in electricity generation and delivery.

typical residences (Fig. 4.1). Appliance technology is continually evolving, and more efficient HVAC systems are being installed or retrofitted in both recently developed and existing buildings [55].

Transmission and distribution losses account for approximately 5% of the total energy used in U.S. electric power systems with an estimated loss of over 206 TWh in 2019 alone [67, 68]. Since current is dependent upon Power Factor (PF), a higher PF load requires less current than that of the same active power with a lower PF. Therefore, change in energy use may be achieved through PF correction and reactive power compensation by reducing resistive losses that result in heat generation in conductive elements [69]. In addition to possibly significant energy savings, other benefits include lower electricity costs, improved power quality, and reduced utility grid (i.e. transformer) and residential equipment degradation.

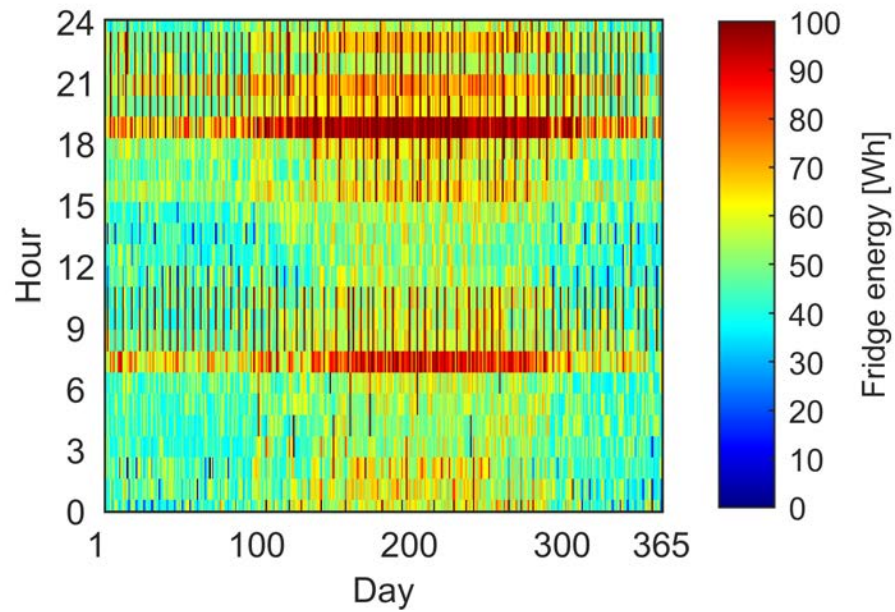
The effects of PF on energy use may warrant their consideration in modeling. Household appliances and equipment have different energy use behaviors based on

both the schedule of occupant use and power requirements during operation. So, it is also important to understand these factors in order to determine the reactive power contributions of appliances. The operation times of such appliances become more predictable at the aggregated level and may be represented by equivalent schedules as exemplified in Fig. 4.2.

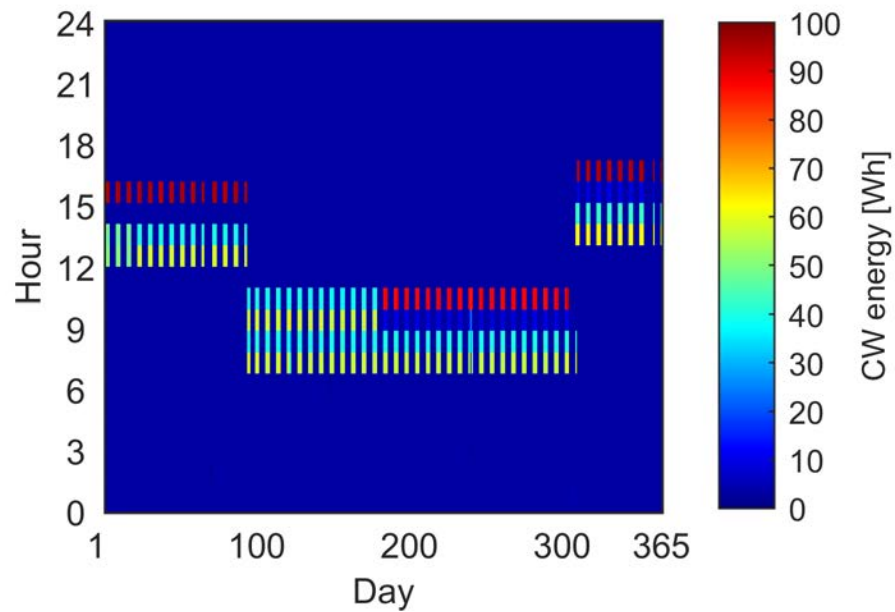
Typical household appliances and local solar Photo-Voltaic (PV) systems offer significant opportunity as Distributed Energy Resources (DERs) for improved power system operation and energy savings. Considering this, the main objectives of this chapter are to:

- Analyze typical residential loads based on measured data from buildings built to be representative of different energy efficiency classes
- Identify energy effects of HVAC system and building technologies
- Develop building energy and temperature models for the analysis of solar PV performance in different geographical locations and to employ in power system control studies.

This chapter is substantially based on the following publication: **E. S. Jones, et al.**, “The Effect of High Efficiency Building Technologies and PV Generation on the Energy Profiles for Typical US Residences,” 2020 9th International Conference on Renewable Energy Research and Application (ICRERA), 2020, pp. 471-476, doi: 10.1109/ICRERA49962.2020.9242665.



(a)



(b)

Figure 4.2: Typical operation schedule through energy use for (a) a refrigerator (Ref) and (b) clothes washer (CW) of a 3 bedroom, 2.5 bathroom house based on the Building America house simulation protocols.

4.2 Field Demonstrators

In 2008, the Tennessee Valley Authority (TVA) began a technology demonstration project with technical support from Oak Ridge National Laboratory (ORNL). Three houses were constructed side-by-side in Knox County, TN to represent three distinct energy profiles: conventional construction, retrofit efficiency, and Near Net-Zero-Energy (NNZE) design (Fig. 4.3). Human habitation was physically simulated within the houses through the operation of equipment and appliances by robots, emulators, and other typical interfaces, such as a programmable thermostat. Scheduling was based on the National Renewable Energy Laboratory (NREL) Building America house simulation protocols.

Four house models were developed based on the physical characteristics of the TVA robotic houses and calibrated against the measured data from the project (Fig. 4.4). These models included a conventional house with a Seasonal Energy Efficiency Rating (SEER) 13 single stage heat pump (Conv13S) and the same conventional house with a SEER 19 variable capacity heat pump (Conv19S). The other two models were of a retrofit house with improved insulation, better windows, and a highly efficient SEER 20.5 variable speed heat pump (RetroF) and a house built from the beginning to be near NZE on an annual basis with a SEER 16 dual stage heat pump (NNZE).

Data for weather, Domestic Hot Water (DHW) draw, and energy usage was collected hourly from 2009 to 2014. The project provided a basis for the analysis of technologies across a spectrum of energy efficiency, including HVAC systems, water heaters, construction, appliances, and residential solar PV systems.



Figure 4.3: The near net-zero-energy (NNZE) house front (a) and back (b). TVA robotic devices are controlled to mimic realistic human behavior. Also shown is a HPWH used in the retrofit house (c), a shower emulator (d), and a refrigerator with programmed arms (e) that operate according to automatic schedules.



Figure 4.4: Example BEopt simulation model for the typical construction house type. All models follow a very similar floor plan but different construction materials and techniques.

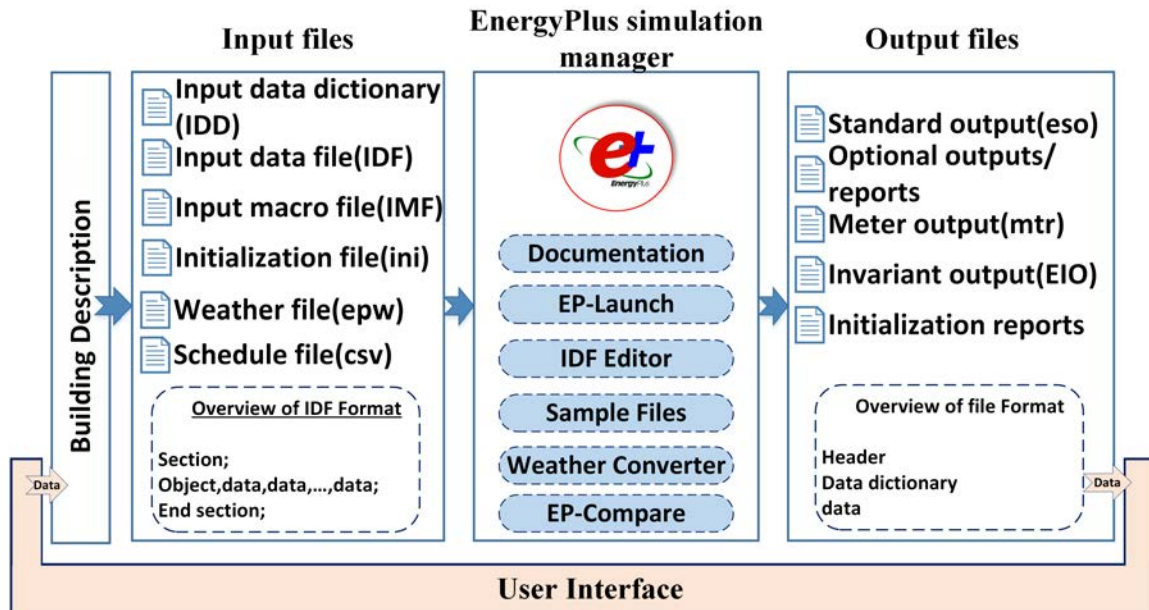


Figure 4.5: The overall system architecture of EnergyPlus, an open source whole building energy simulation program that models energy use for both HVAC system and plug and process loads.

4.3 Physics-based HVAC and Building Modeling with EnergyPlus

The residential building energy models were developed with a combined software process that utilized EnergyPlus and the Building Energy Optimization Tool (BEopt) and (Figs. 4.4 and 4.5). EnergyPlus is a widely used open-source Building Energy Model (BEM) simulation tool that models energy consumption for typical building loads (i.e. HVAC, lighting, and plug and process loads) and domestic water use [70]. EnergyPlus building models are initialized by three sets of data, which include building parameter and construction specifications, weather data, and a DHW usage schedule. The first version of the software was published in 2001 and has since been updated on a bi-annual basis.

NREL's BEopt software includes EnergyPlus as the base simulation engine [71].

BEopt accepts as input the geometry of the building and construction details, including attic and wall insulation, wall stud type, windows, and roofing as well as appliance and equipment efficiencies. BEopt also considers occupancy and geographical weather data to produce a detailed EnergyPlus Input Data File (IDF) [72].

Extensive building specifications can be provided to EnergyPlus through a user interface, which is bypassed by use of BEopt as previously discussed. All input files are written in a flat ASCII file that is fully readable and editable. The “InputProcessor” function utilizes the Input Data Dictionary (IDD) file to interpret the IDF file, which is then executed for simulation. The desired outputs are also generated by processing in a predefined manner of which the user has full control.

EnergyPlus simulates total energy use of the building as well as for individual appliances. The software may also interface with Python through a recently available internal plug-in or through third-party libraries and software, such as the Building Controls Virtual Testbed (BCVTB). This feature provides considerably improved functionality with the added prospect of automated building generation, model calibration, and co-simulation with other software. For example, in section 4.7, reactive power is calculated post-simulation within the Python environment by analyzing the provided energy results and applying an equivalent power factor.

The HVAC and building models developed in this work employed weather data collected from an onsite weather station during two example years. Data from 2010 was utilized for models Conv13S and NNZE, while 2013 data was for Conv19S and RetroF. It is important to have actual local weather data due to the HVAC system’s high sensitivity to climate. Accurate modeling of an HVAC system requires a small

timestep to capture highly transient behavior [73]. Considering this, the models were simulated at a timestep of one minute. The actual measured energy use and weather data were recorded with the resolution of one hour. This mismatch prevented model calibration at smaller timesteps and was satisfactory for the analysis of monthly energy usage.

Once the initial BEopt models for the robotic houses were converted into EnergyPlus models, a significant effort was made to minimize difference between actual measured and simulated energy usage of the HVAC components. A variety of factors were considered, including material thermal mass, attic and wall insulation, and HVAC Coefficient Of Performance (COP).

After various tests, the best versions of the models kept the same values as specified by TVA except for the COP ratings of the HVAC systems, which were adjusted to minimize error between measured and simulated HVAC system energy usage. For the two models that were based on 2013 data, monthly energy use was brought to within 15% difference of the measured values (tables 4.1 and 4.2), a limit that followed ASHRAE Guideline 14 [74].

It was notably challenging to reduce error for certain "shoulder" months such as April, May, and October due to their very low energy usage and mixture of both heating and cooling, especially for the building models based on the 2010 data (tables 4.3 and 4.4). It should also be noted that such error is exacerbated when increased solar heat gain and mild temperatures occur simultaneously, which is due to the underestimation of the solar heat gain effect by the models. This phenomenon occurred in 2010, which caused the other two models based in that year to have shoulder month

Table 4.1: Monthly and annual comparison of simulation results to measured data of Conv19S based on actual locally measured weather data in 2013.

Month	Measured tot. energy (kWh)	Simulated tot. energy (kWh)	Tot. energy error (%)	Portion of meas. annual energy use [%]	Ratio of meas. to sim. energy
Jan	922	932	-1	14	0.99
Feb	802	759	5	12	1.06
Mar	813	737	9	12	1.1
Apr	194	221	-14	3	0.88
May	188	199	-6	3	0.94
Jun	391	371	5	6	1.05
Jul	432	430	0	7	1
Aug	419	442	-6	6	0.95
Sep	302	270	11	5	1.12
Oct	247	260	-5	4	0.95
Nov	704	672	5	11	1.05
Dec	1,109	943	15	17	1.18
Total year	6,524	6,239	4	100	1.05

Table 4.2: Monthly and annual comparison of simulation results to measured data of RetroF based on actual locally measured weather data in 2013.

Month	Measured tot. energy (kWh)	Simulated tot. energy (kWh)	Tot. energy error (%)	Portion of meas. annual energy use [%]	Ratio of meas. to sim. energy
Jan	688	721	-5	14	0.99
Feb	592	588	1	12	1.06
Mar	613	559	9	12	1.1
Apr	144	159	-11	3	0.88
May	120	114	5	3	0.94
Jun	249	239	4	6	1.05
Jul	280	294	-5	7	1
Aug	273	304	-12	6	0.95
Sep	188	168	11	5	1.12
Oct	151	168	-11	4	0.95
Nov	473	502	-6	11	1.05
Dec	707	710	0	17	1.18
Total year	4,479	4,528	-1	100	1.05

Table 4.3: Monthly and annual comparison of simulation results to measured data of Conv13S based on actual locally measured weather data in 2010.

Month	Measured tot. energy (kWh)	Simulated tot. energy (kWh)	Tot. energy error (%)	Portion of meas. annual energy use [%]	Ratio of meas. to sim. energy
Jan	1,995	2,112	-6	17	0.94
Feb	1,609	1,642	-2	14	0.98
Mar	814	886	-9	7	0.92
Apr	196	352	-80	2	0.56
May	862	360	58	7	2.4
Jun	982	868	12	8	1.13
Jul	942	1,077	-14	8	0.87
Aug	947	1,047	-11	8	0.9
Sep	516	509	1	4	1.01
Oct	129	366	-185	1	0.35
Nov	528	504	4	4	1.05
Dec	2,298	1,970	14	19	1.17
Total year	11,818	11,694	1	100	1.01

energy use error outside of the 15% goal. In this study, the errors from the shoulder months were considered minimal because the energy usage of those months were only 1% to 7% of the annual total.

4.4 HVAC and Building Technologies and their Effect on Energy Usage

After each of the four HVAC system models were calibrated based on actual energy use and weather measurements, they were simulated for an entire year based on Knoxville, TN TMY3 weather data so that the technologies may be generally compared under the same weather conditions ([75]) (Fig. 4.6). Since Conv13S and Conv19S were the same building energy model, the effects of the HVAC component alone may be observed (Fig. 4.7).

The measured and calculated HVAC power for two example days is provided for Conv19S in Fig. 4.8. The February day had a measured total daily energy use of 51 kWh, and a total error of 1% when compared to the model. For the May day, 5 kWh and 45%, respectively. The higher error for the shoulder month is typical due to the

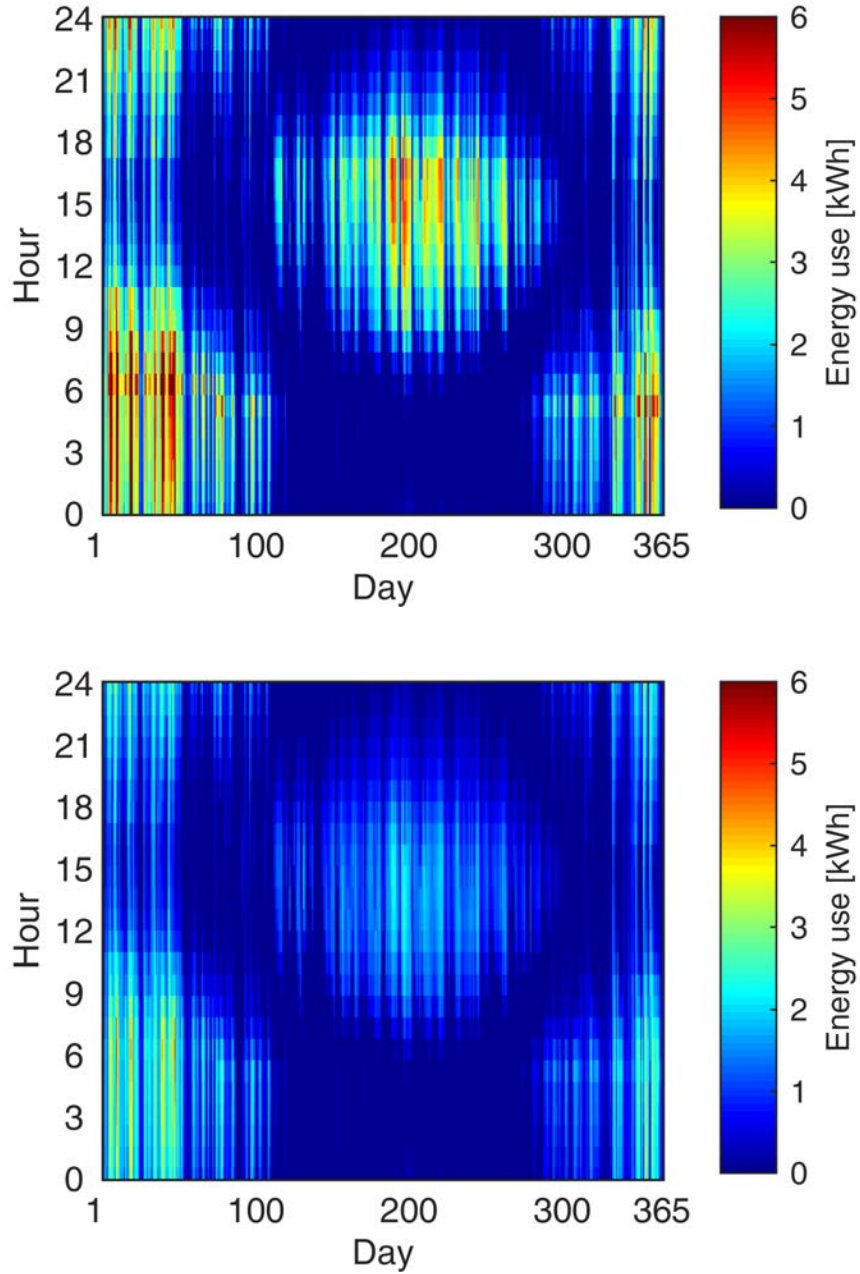


Figure 4.6: Hourly energy usage for the HVAC system of the simulated conventional house (a) and the hourly energy difference between the HVAC systems of the conventional house and the NNZE house (b) based on Knoxville, TN TMY3 weather data.

Table 4.4: Monthly and annual comparison of simulation results to measured data of NNZE based on actual locally measured weather data in 2010.

Month	Measured tot. energy (kWh)	Simulated tot. energy (kWh)	Tot. energy error (%)	Portion of meas. annual energy use [%]	Ratio of meas. to sim. energy
Jan	1,095	1,002	8	22	1.09
Feb	813	736	9	16	1.10
Mar	359	403	-12	7	0.89
Apr	53	149	-179	1	0.36
May	196	111	43	4	1.76
Jun	358	354	1	7	1.01
Jul	425	483	-14	8	0.88
Aug	448	468	-4	9	0.96
Sep	247	235	5	5	1.05
Oct	64	142	-123	1	0.45
Nov	220	204	7	4	1.08
Dec	750	813	-8	15	0.92
Total year	5,027	5,103	-1	100	0.99

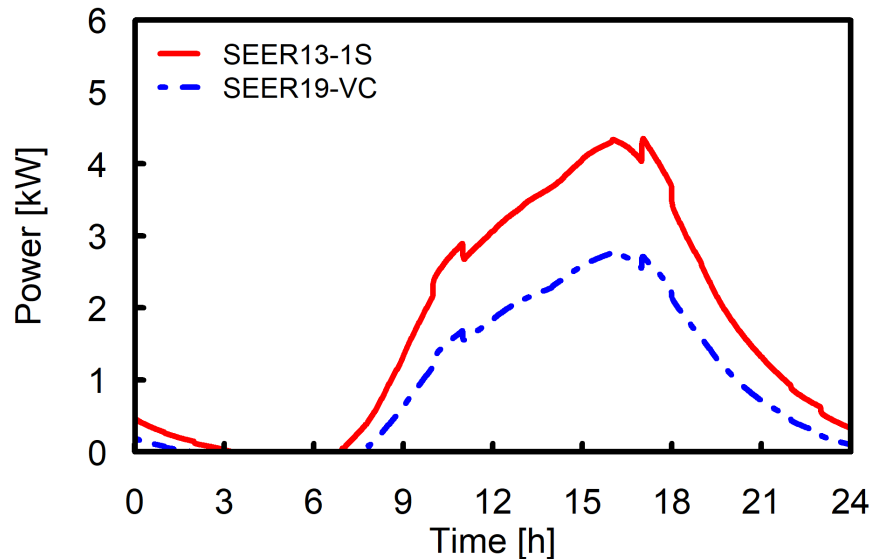


Figure 4.7: Power for the HVAC systems in the Conv13S and Conv19S models. Both were simulated using Knoxville TN, TMY3 weather data on an example summer day.

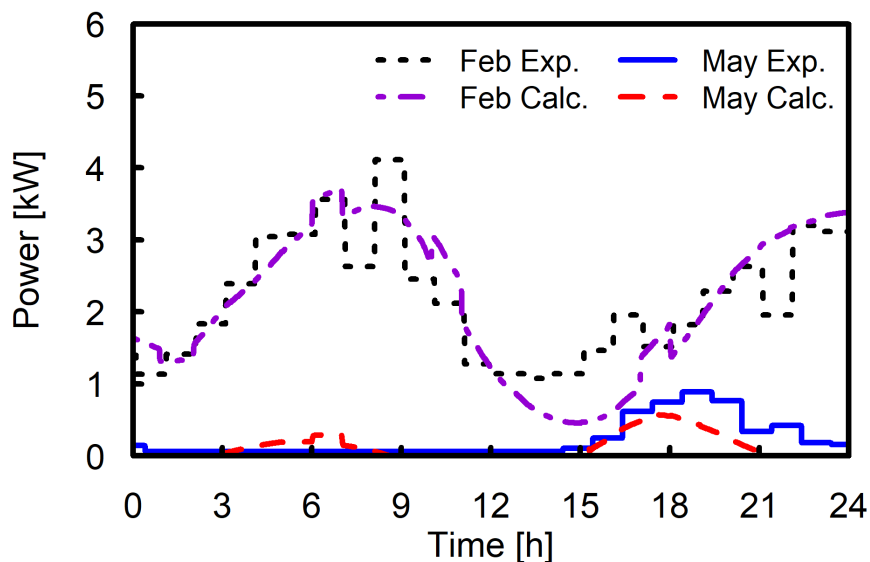


Figure 4.8: HVAC system power for a high energy use, heating-only February day and a low energy use day in May with a mixture of heating and cooling.

Table 4.5: Energy usage and peak power for different HVAC systems in the house models with Knoxville, TN TMY3 weather

House model	Annual total energy [kWh]	Peak hourly power [kW]
Conv13S	9,699	10.5
Conv19S	7,131	8.9
RetroF	5,467	6.9
NNZE	4,148	5.7

mild temperatures and much lower required HVAC energy use.

As anticipated, the SEER 19 variable capacity heat pump was much more energy efficient than the SEER 13 single stage heat pump with annual HVAC system energy savings of 2,568 kWh or 26% (13% of the total house use) and a 15% reduction in HVAC system hourly peak (Table 4.5).

When the HVAC system and building construction are both improved, as shown in the comparison between cases Conv13S and NNZE, the HVAC system annual total energy usage and hourly peak may be reduced by 57% and 46%, respectively.

4.5 Water Heaters and Other Appliances

Since schedule-based in-house devices, such as lighting and appliances that use DHW, are minimally affected by climate, experimental measurements from the TVA project are used directly for their analyses.

The measured loads in Fig. 4.9 shows that Water Heaters (WHs) are typically the second most energy using individual component of a house, after the HVAC system. This is another opportunity to realize significant energy savings through changing a single appliance. Since the energy usage of WHs is decisively dependent upon human behavior, the study of the component was based upon measured data. Inside the TVA robotic houses, automated systems implemented schedules to represent the use of DHW and appliances (Fig. 4.10) [76]. DHW use schedules in the project were derived from the Building America House Simulation Protocol [77].

According to the measured energy use of the WHs in the conventional and retrofit houses in 2010, it was found that upgrading from an Electric Water Heater (EWH) with typical appliances to a Heat Pump Water Heater (HPWH) with EnergyStar appliances yielded remarkable results in energy use reduction. Over the entire year, the 50 gallon HPWH in the retrofit house used a total of 2,179 kWh (57%) less than the EWH in the conventional house. This is due to the better appliances as well as the improved technology of the HPWH (Fig. 4.11).

Upon initial construction of the typical and retrofit homes in 2009, a 40 gallon EWH and a HPWH were selected to represent a baseline standard home and an improved, modified home for energy efficiency, [76]. The WHs have an energy factor

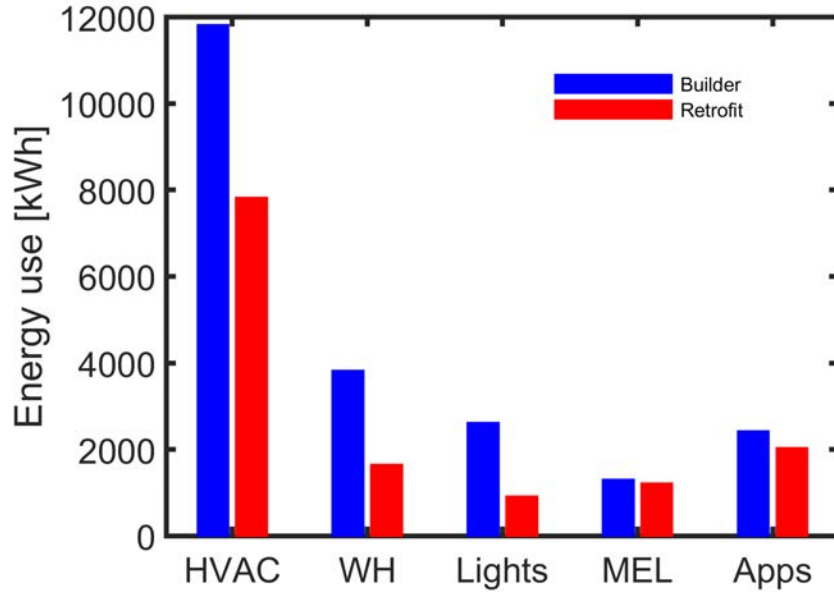


Figure 4.9: Total actual measured energy usage of the HVACs, WHs, lights, Miscellaneous Electric Load (MEL), and appliances (Apps) within the conventional and retrofit houses for the year of 2010. The HVAC is consistently the highest individual energy user, while the water heater is always the second highest.

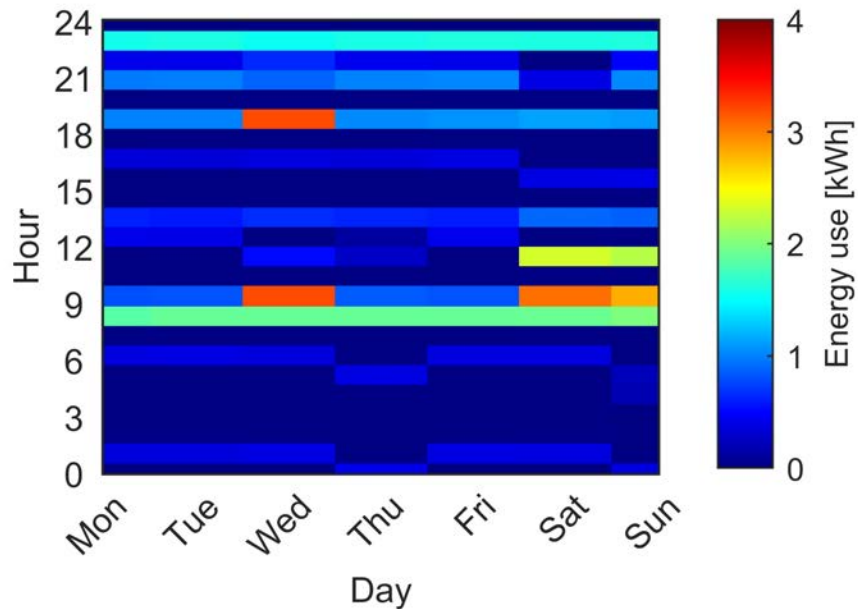


Figure 4.10: Example week for the electric water heater (EWH) schedule.

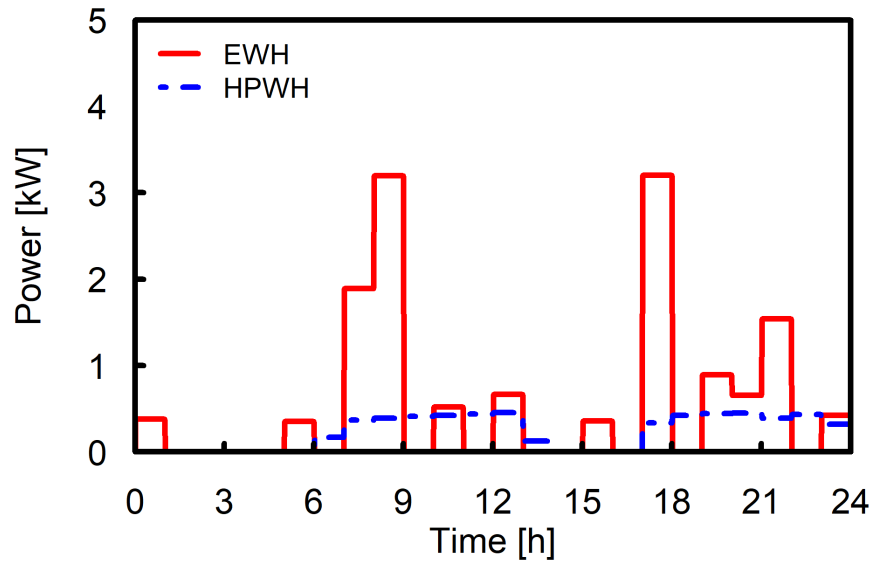


Figure 4.11: Power for the conventional house EWH and the retrofit house HPWH during an example day in 2010.

of 0.9 and 2.5. The retrofit home was also equipped with EnergyStar dishwashers, refrigerators, clothes washers and dryers.

Inside the homes, an automated robotic system implemented schedules to represent the use of DHW and appliances. The DHW use schedules for the showers, baths, sinks, dishwasher, and clothes washer were all based on WH studies and scientific references selected in the Building America House Simulations Protocol [77]. Equations based on the numbers of rooms and Finished Floor Area (FFA) in the home are provided as well for the DHW usage and miscellaneous loads.

Adjustments were made to the typical home to better simulate occupant load in October of 2013. The standard electric water heater was replaced with a GE HPWH. The year of 2013 to 2014 had 54% reduction in hot water energy use than 2012- 2013 with the electric water heater. This is a significant drop of 2052 kWh over a year from 3,839.2 to 1,787.3 kWh for domestic hot water in the typical home.

In the retrofit home from 2013 to 2014 an EcoCute CO₂ HPWH was installed. Compared to the GE HPWH in the typical home, it used 123 less kWh and is thus comparable as the typical home as it did not include Energy Star appliances. It is important to note that due to an equipment failure in the beginning of the year the total DHW energy use was higher in 2013 than 2011. Large energy savings potential are available with HPWHs.

In order to reduce peak time energy use by the water heater (for clothes washing hot water needs), two time-based load-manage temperature profiles were tested in 2010. 1) Tank temperature of 140°F during the night, 170°F from 3 am to 1pm, then 120°F during peak to 9pm. 2) Starting at 6 am to peak time set tank temperature to 150°F, 120°F during peak and then 170°F afterwards.

With only HPWH used to meet demand, both schedules succeeded at moving hot water load away from the peak on non-laundry days, but overall daily load increased. Less total energy was used by profile 2) than 1). When laundry was done, however, 1) had 8% less energy than 2), and 2) also failed to move the hot water load from peak time contradicting the results seen on non-laundry days. It was concluded that occupancy habits affect the success of scheduling hot water load management for HPWH.

4.6 Rooftop PV Performance for Different Geographical Locations

An external PV module was modeled and calibrated against the measured hourly average power generation through determination of unknown parameters by differential evolution to minimize error for the 2.5kW rooftop solar PV system on the NNZE

house (Fig. 4.3b). In retrospect, this calibration would have been an excellent application of linear regression. The DC power output of the PV module was determined as follows:

$$p_{g,pv} = \left[\left(\frac{\gamma}{1000} \right) p_{r,pv} \right] \left[1 - \left(\frac{k_p}{100} (t_c - 25^\circ C) \right) \right] * \eta_{pv}, \quad (4.1)$$

where γ , the solar irradiance [W/m^2]; $p_{r,pv}$, the PV array rated power [W]; k_p , the temperature coefficient of maximum power [$\%/^\circ C$]; η_{pv} , the efficiency considering losses due to the inverter, interconnection of modules with nonidentical properties, and dirt accumulation; t_c , the temperature of the PV cells [$^\circ C$], which is calculated by:

$$t_c = t_o + \left(\frac{t_n - 20^\circ C}{0.8} \right) \left(\frac{\gamma}{1000} \right), \quad (4.2)$$

where t_o is the outdoor ambient temperature [$^\circ C$] and t_n is the nominal operating cell temperature [$^\circ C$].

With T_{amb} and γ measured onsite hourly, average power output was calculated at the same timestep using the proposed PV module and compared to the actual values. Even though PV generation experiences significant transient behavior from variable weather conditions, an hourly timestep was found to be satisfactory for studies down to the daily level (Fig. 4.12). When considering days in the example year of measured data with error above 0.1 kWh between calculated and measured PV power output, only about 7% have a percent error above 10%. These days are likely due to the irradiance sensor and solar panels experiencing different solar radiation from weather effects such as cloud cover. At a monthly comparison, the results are satisfactory with error only ranging from approximately 1% to 6%.

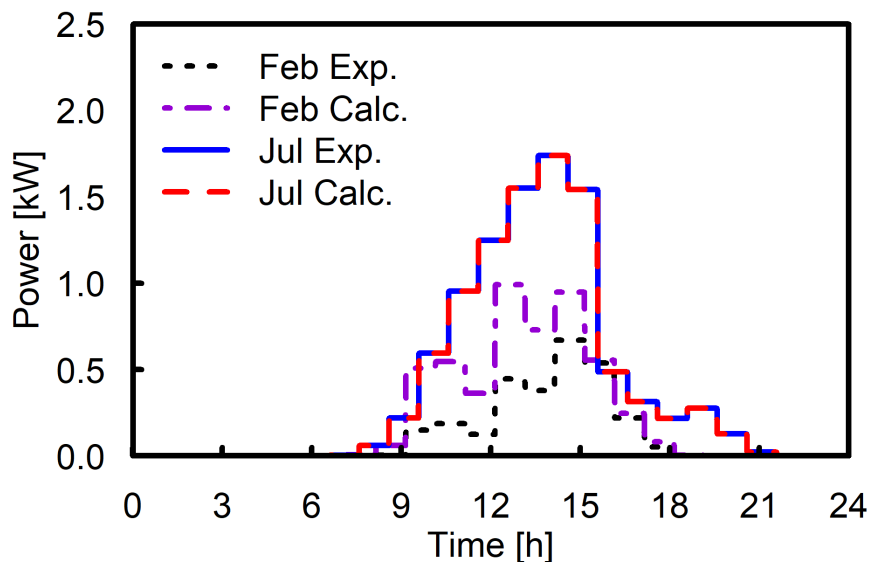


Figure 4.12: Example daily PV power for the typical case of very low daily energy error and the rare case of higher error which is likely due to differing solar radiation between the irradiance sensor and actual PV panel.

Table 4.6: Average hourly solar radiation, total annual PV energy generation calculated on an hourly basis, and CF for simulated locations based on TMY3 weather

Location	Radiation [W/m^2]	PV [kWh]	CF [kW]
Bowling Green, KY	154.9	2,927	13.4
Bristol, TN	174.5	3,392	15.5
Chattanooga, TN	178.8	3,313	15.1
Columbus, MS	182.2	3,345	15.3
Knoxville, TN	178.3	3,359	15.3
Memphis, TN	187.2	3,475	15.9

The performance of a simulated 2.5kW PV system was determined for six different locations over an entire year using TMY3 weather after the proposed PV module was calibrated based on onsite measured data. The annual PV generation and calculated Capacity Factor (CF) as well as average hourly solar irradiance, which is for illustration purposes only and not for calculations, are provided (Table 4.6).

As expected, the most northern location, Bowling Green, KY, had the smallest CF while one of the most southern, Memphis, TN, had the highest value (Fig. 4.13).

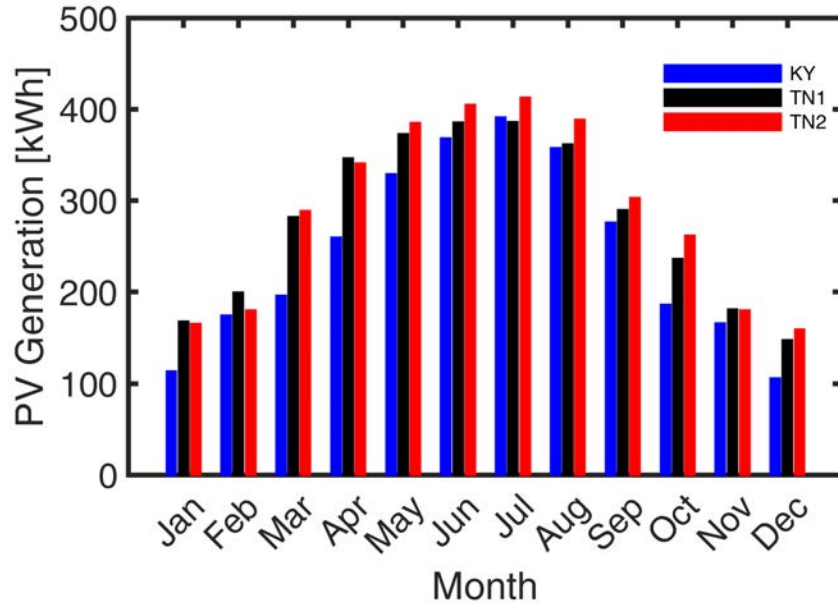


Figure 4.13: Monthly total PV generation for TN1 (Knoxville, TN), TN2 (Memphis, TN), and KY (Bowling Green, KY) locations.

To further illustrate the significant relationship between geographical location and PV generation, the full simulated year of PV generation in Memphis, TN is provided along with the hourly energy difference between the simulations in Memphis, TN and Bowling Green, KY (Fig. 4.14).

The PV system rating required for each building energy model to be considered NZE on an annual basis was determined for multiple locations [78]. The typical Conv13S house ranges from 14.2kW to 18.4kW. The NNZE house has a much lower range of 6.4kW to 8.3kW (Table 4.7). This illustrates that both the geographical location and the house type have a significant influence on the PV rating required for a house to be considered NZE.

Since the actual 2.5kW solar system took up nearly a third of the roof space of the NNZE example house, it would be fair to assume that a typical house of this

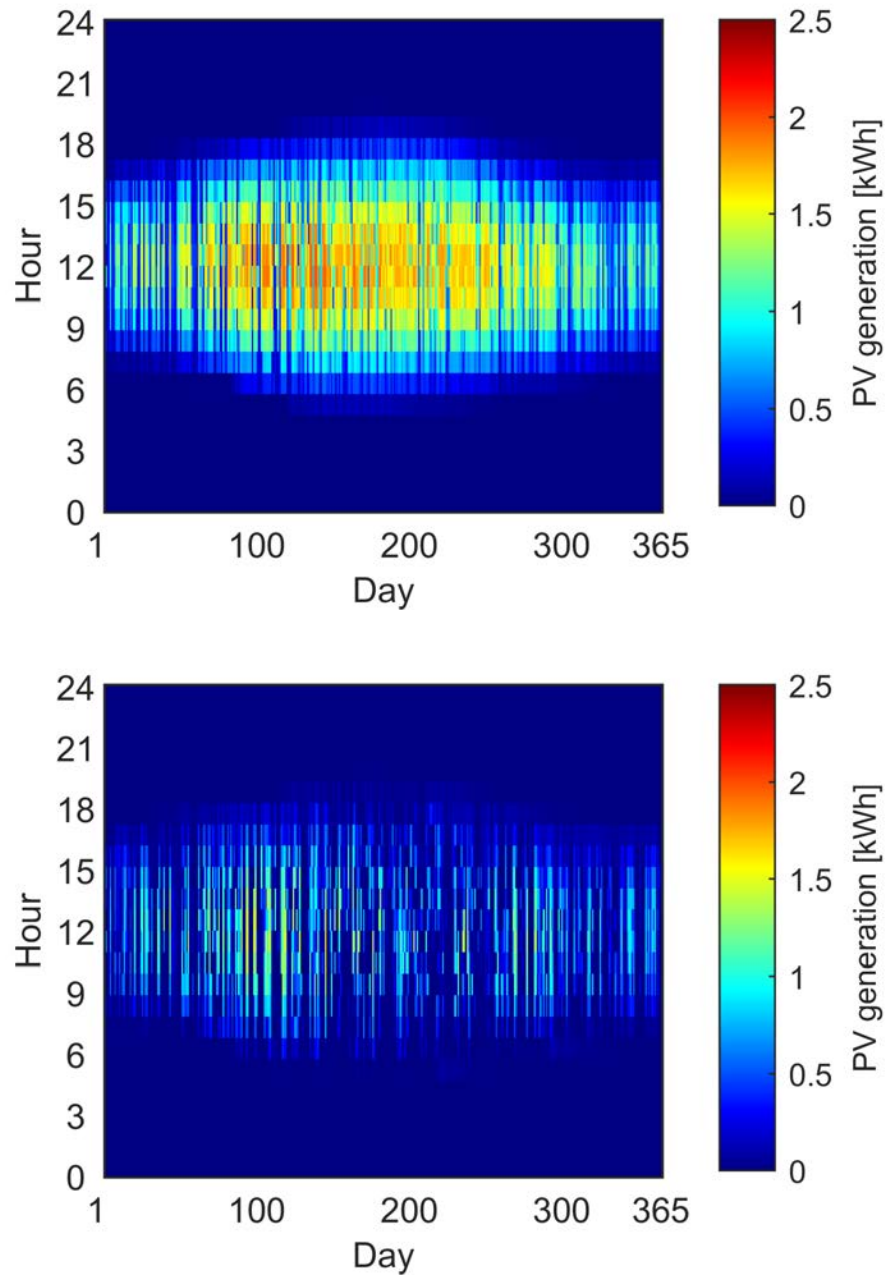


Figure 4.14: Hourly PV energy generation of the simulated 2.5kW PV system in Memphis, TN (a) and the hourly energy difference between system simulations in Memphis, TN and Bowling Green, KY (b). All simulations were based on TMY3 weather data.

Table 4.7: PV ratings (kW) required to achieve NZE for houses of different types in all simulated locations

Location	Conv13	Conv19	RetroF	NNZE
Bowling Green, KY	18.4	16.3	11.1	8.3
Bristol, TN	14.5	13.1	8.9	6.5
Chattanooga, TN	14.2	12.5	8.4	6.4
Columbus, MS	15.4	13.3	8.9	7.3
Knoxville, TN	14.8	13.1	8.9	6.7
Memphis, TN	14.4	12.4	8.3	6.8

size could only support, at best, a PV system of around 9kW maximum (Fig. 4.3b).

Therefore, only the RetroF or NNZE house types in certain locations would be able to realistically support a PV system large enough to be NZE.

4.7 Appliance Power Factor and Reactive Power

The main causes of reduced PF in electric power circuits include harmonic distortion and the displacement of phase angle between voltage and current. The general representations of displacement and harmonic effect in the overall "true" RMS PF of typical residential appliances in resistive elements, such as building wiring and transmission and distribution lines, are illustrated in Fig. 4.15.

Voltage and current waveform examples of actual data measured from a vacuum cleaner and DC power supply illustrate the influence of harmonic distortion on power factor and are provided in Fig. 4.16. Phase displacement occurs when the current of the reactive loads lag (for inductance) or lead (for capacitance) the voltage. Due to the displacement, increased current is required to sufficiently supply the load.

Residential building load types include resistive, reactive, and non-linear, including those that are electronically supplied or controlled (Table 4.8). Resistive loads

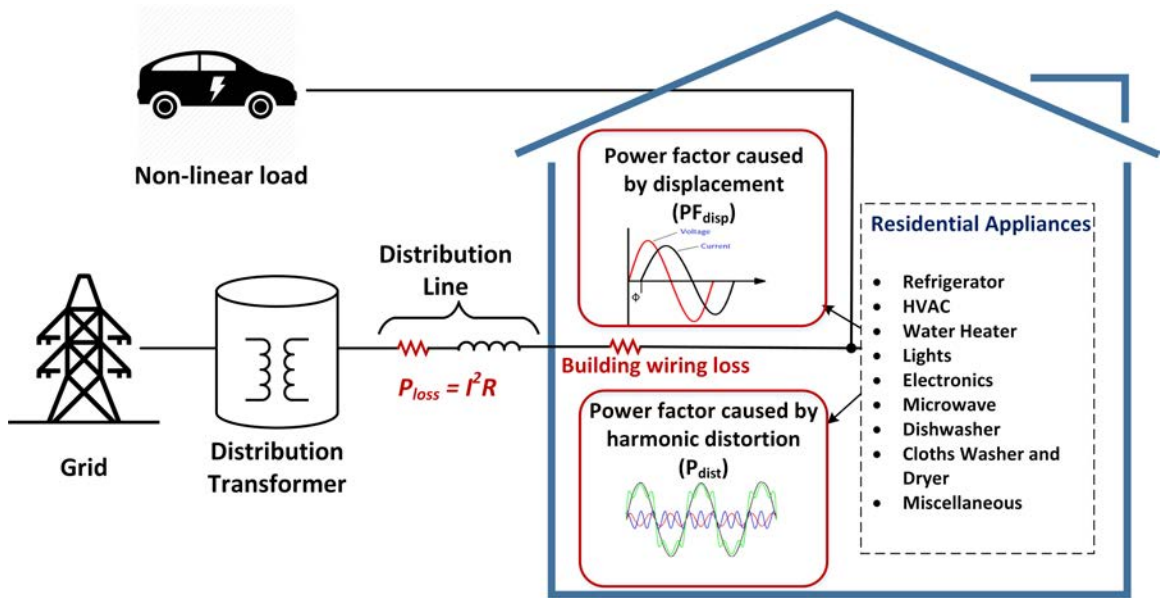


Figure 4.15: Overview of the system losses (grid and building level) caused by low PF of the typical residential home appliances. The upstream losses of the distribution transformers are not shown.

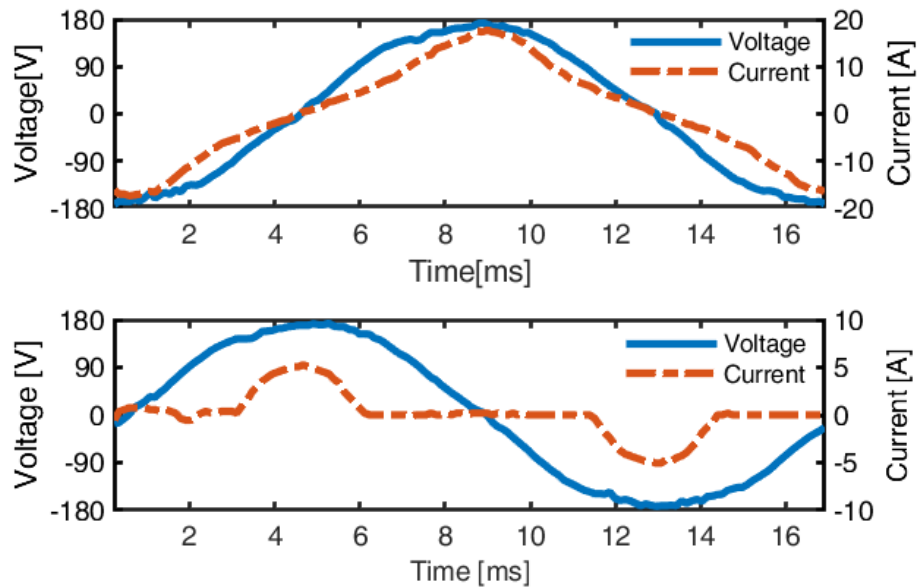


Figure 4.16: Real examples of voltage and current waveforms for (top) a vacuum cleaner and (bottom) DC power supply illustrating the influence of harmonic distortion on PF.

cause neither displacement nor harmonic impacts, resulting in unity PF. Such examples include incandescent lamps and electric water heaters. Reactive loads can be either inductive or capacitive, such as electric motors, pumps, and compressors. Switched-mode power converters are typically employed with non-linear loads to function as rectifiers, with examples including most electronic loads (i.e., computers, TVs, monitors, printers, etc.). Such loads may produce high harmonic content due to the solid-state converter or rectifier, which can be substantial without PF correction.

Although electronically-controlled loads may reduce PF, several advancements to improve overall energy efficiency for residential appliances have also been achieved with this technology, including energy use/consumption forecasting [86] and appliance control and energy monitoring through smart plugs [87].

Since the HVAC system is typically the largest energy-user, a specific example case of power requirements during operation is provided in Fig. 4.17(a). The HVAC power cycle has much less variability than that of the smaller appliance cycles illustrated in Fig. 4.17(b). HVAC systems are different from other typical residential appliances in that its operation schedule is dominantly climate-based. Weather effects generally supplant that of the occupant's influence. So, hot and humid climates may realize more energy savings than more mild regions.

Potential for energy savings at both the residential and community levels exists through PF management. Few regulations currently exist to encourage PF correction on typical household appliances and electronic devices. An early example of PF regulation in California applies to televisions of 100W and more with a PF requirement of at least 0.9 [85], but the considerable possible benefits of PF improvement at this

Table 4.8: Energy and Power Factor Characteristics of Typical Residential Appliances in the U.S.

Appliance	Energy Usage [%]	Active Power [W]	Power Factor	Source
Refrigerator	7.0	100-145	0.8-0.99	[79],[80],[81],[82]
Clothes dryer	4.5	2500-5700	1.0	[79],[80],[82]
Washing Machine	0.4	500-540	0.55-0.59	[79], [80]
Dishwasher	0.5	1100	1.0	[80]
Water heater	13.6	4500	1.0	[80]
Microwave oven	1.1	1700	0.9	[81],[82], [83]
HVAC	36.1	1840-2340	0.90-0.92	[79],[80]
Pool/hot tub/sauna pump	1.5	900-2300	0.35-0.8	[84]
Dehumidifiers	1.2	200-750	0.3-0.8	[84]
TV	<i>a</i>	49-190	0.53-0.94	[79],[85], [81]
Computers (Desktop)	<i>a</i>	95-200	0.63-0.99	[79],[81], [83]
Laptop	<i>a</i>	26-130	0.53-0.99	[79],[81]
LED Lamps	<i>b</i>	8-10	0.7-0.8	[84]
Fluorescent lamps	<i>b</i>	13-16	0.5-0.8	[79], [84]
Incandescent lamps	<i>b</i>	96	1.0	[79], [83]
Vacuum	<i>c</i>	987-1360	0.96-0.98	[79],[81]

^a 6.9% including all other electronics appliances

^b 10.3% including all other lighting loads

^c 13% including all other miscellaneous appliances

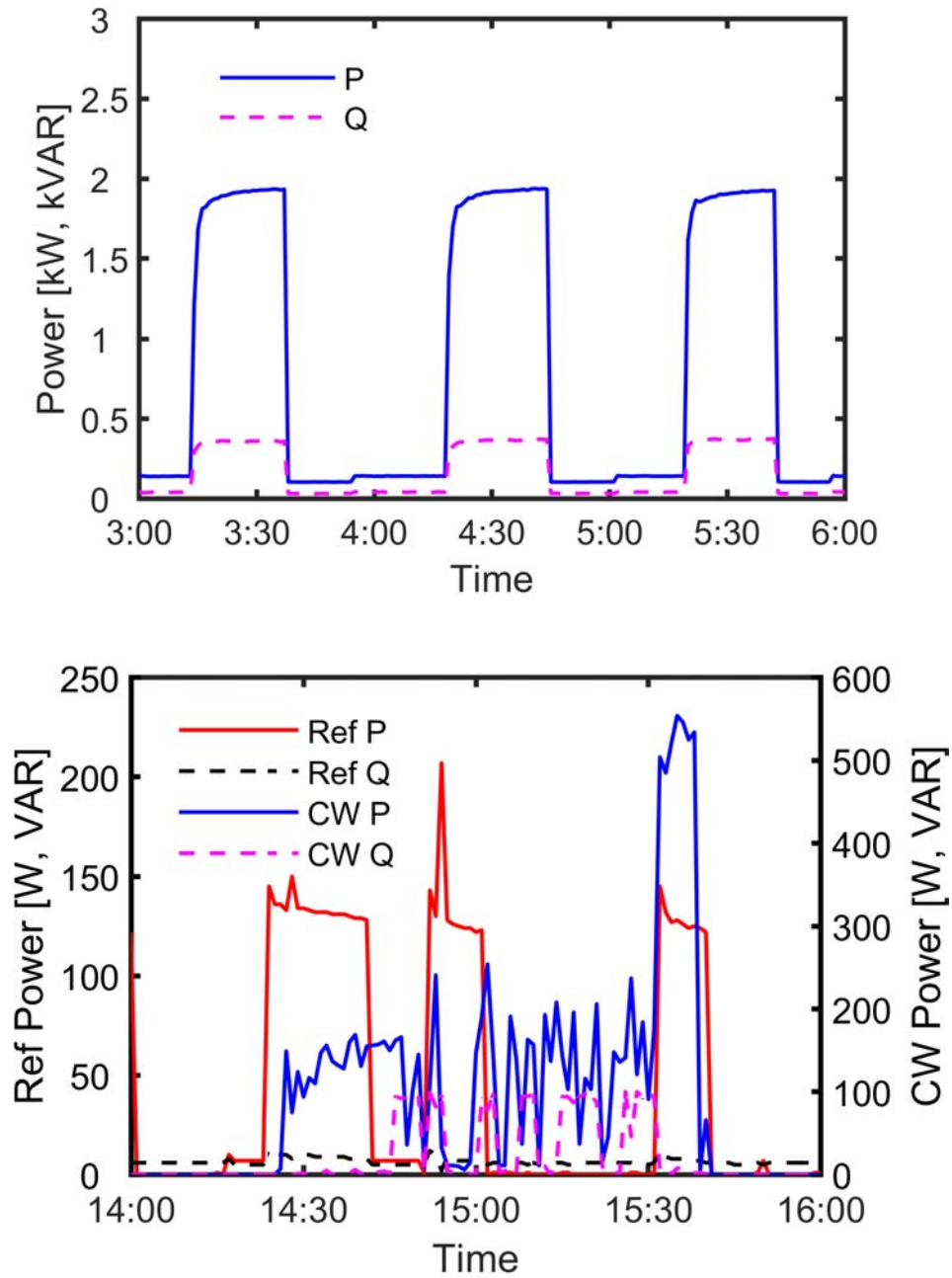


Figure 4.17: Real and reactive power during example operation cycles of (a) a typical HVAC system as well as (b) a refrigerator and a clothes washer based on experimental data.

level has still yet to be fully realized.

According to EPRI research, a 0.9 PF minimum requirement on plug loads above 50W at 50% and 100% load scenarios could save up to 241 GWh per year in California [85]. Nationally, the potential energy savings could be as much as 15.8 TWh per year [84]. California's Energy Commission has also provided studies on television PF, reporting that an improvement from 0.5 PF to 0.95 PF would reduce the associated load current from 1.7A to 0.9A and improve building wiring power losses by more than 70% [88].

As reactive power contributions from residential buildings become more prevalent in the electric power grid from advancing modern appliance technology, it is increasingly important to consider reactive power effects in building energy modeling. As discussed previously in section 4.3, the EnergyPlus building modeling software employs schedules of occupant use and weather data for simulation [70]. Both the schedule of occupant use and corresponding power ratings are important for equivalent PF calculation.

Reactive power may be calculated in post-processing or during BEM simulation as added functionality to building energy modeling software, such as EnergyPlus, that may not already consider it. Equivalent PFs are calculated by averaging the corresponding real and reactive power based on specified time scales and interpolating the average as a constant value to the original time scale. Example equivalent PF calculation is provided in Fig. 4.18 based on the same minutely data utilized in Fig. 4.17 for example appliances at 1-minute, 15-minute, and hourly time intervals, which correspond to smart metering and traditional building modeling practices.

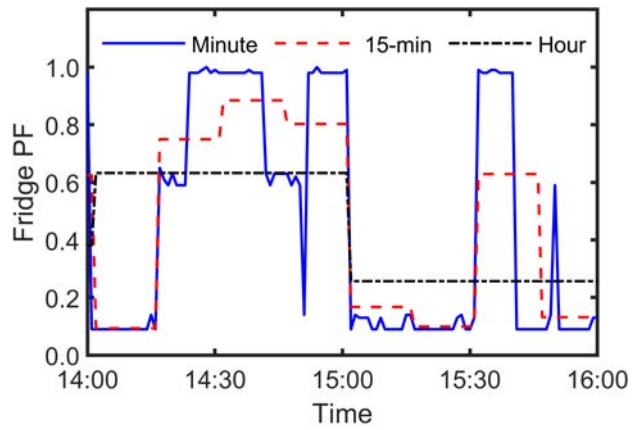
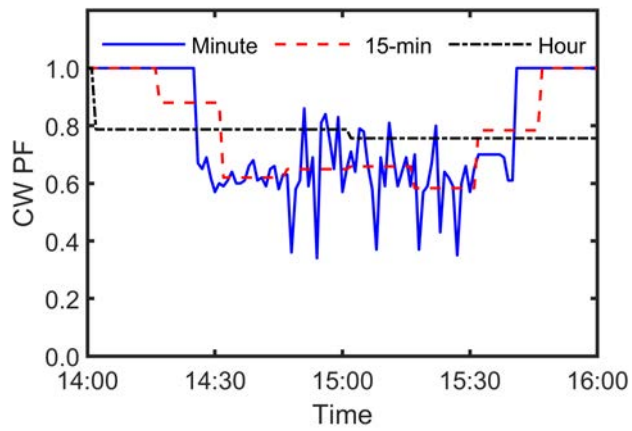
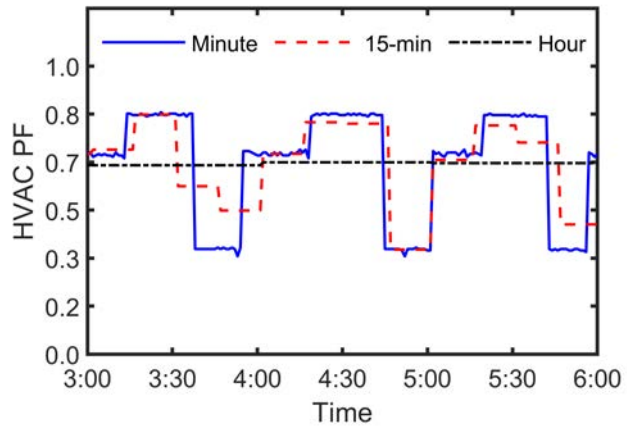


Figure 4.18: Experimental minutely PF and calculated equivalent PF for 15-minute interval, which corresponds to typical smart metering, and the traditional hourly interval for (a) an HVAC system, (b) a refrigerator, and (c) a clothes washer (CW).

The equivalent PF may vary greatly between time scales based on the provided example (Fig. 4.18). The determination of equivalent PF in aggregation through the proposed procedure may, in principle, be utilized for the determination of reactive power for entire communities by averaging from the house level.

4.8 Summary

There is significant opportunity for reducing energy use in the residential sector through high efficiency technologies and for increasing distributed solar Photo-Voltaic (PV) generation. This study illustrates this through the experimentation and simulation of buildings, Heating, Ventilation, and Air-Conditioning (HVAC) systems, and PV energy models as well as through comparison of schedule-based in-house devices such as Water Heaters (WHs) and appliances. It was shown that an HVAC system upgrade alone, without any changes to the building, can reduce energy use of the HVAC by 26% or by 13% of the total house's energy use.

With better construction materials and improved techniques, HVAC energy savings can more than double to 57% with a 46% reduction in HVAC system peak hourly power. It was shown that this combination may reduce the PV rating that is required for a house to be considered Net Zero Energy (NZE) by up to 55%, depending on location. For the simulation locations, it was determined that only the RetroF or NNZE house designs could support enough rooftop solar PV panels to be considered fully NZE over an entire year. It was also shown through experimental methods that Heat Pump Water Heater (HPWH) technology with better appliances can use up to 57% less energy than an Electric Water Heater (EWH) with typical appliances over

an example year. This reduction is very significant since the WH is the second most energy using device in a typical house.

Modern electric loads are increasingly including power electronics converters and are non-linear with respect to displacement and/or harmonic impacts. Therefore, the consideration of Power Factor (PF) and reactive power for typical residential loads in building energy modeling is becoming more important. A survey of typical residential appliance PF values and energy characteristics as well as a proposed approach for equivalent PF calculation is provided in this work, which may be employed at the community level for studies on residential reactive power contributions.

Equivalent PF calculation and reactive power estimation with building energy modeling may facilitate compensation technologies that promote considerable residential energy savings. A set of high resolution residential data is provide as an example and utilized to determine average PF of different appliances for 15-minute and hourly resolutions, which correspond to typical smart metering and building modeling practices. A method to apply equivalent PF to the EnergyPlus building energy modeling software is also proposed to determine reactive power contributions from simulated loads.

Chapter 5

Virtual Power Plant Control of Smart Homes and Grids

5.1 Introduction and Main Problem

Residential loads constitute approximately 25% of total annual energy in the U.S. compared to commercial and industrial [30]. Within these communities, Heating, Ventilation, and Air-Conditioning (HVAC) systems are the largest end use at around 50% of total typical building loads. There is significant opportunity in leveraging Distributed Energy Resources (DERs) like HVAC systems as energy storage solutions to shift or shape load over time through Virtual Power Plant (VPP) controls [33, 89].

Controls for load manipulation are invaluable tools for utilities to manage the emerging smart grid and optimally utilize increasingly more prevalent and intermittent demand-side generators, such as Behind-The-Meter (BTM) solar Photo-Voltaic (PV) systems [90–92]. As a promising DER type, battery energy storage systems (BESSs) can be an effective, but costly, utility grid energy management solution [35, 36, 92, 93]. They require planning and coordination strategies through simulation to ensure adequate sizing for other DERs that may generate power intermittently [94]. Such DERs can benefit greatly by co-location of BESSs in terms of grid interconnection and cost-effectiveness [95].

As an alternative to BESSs, HVAC and water heating systems that are already

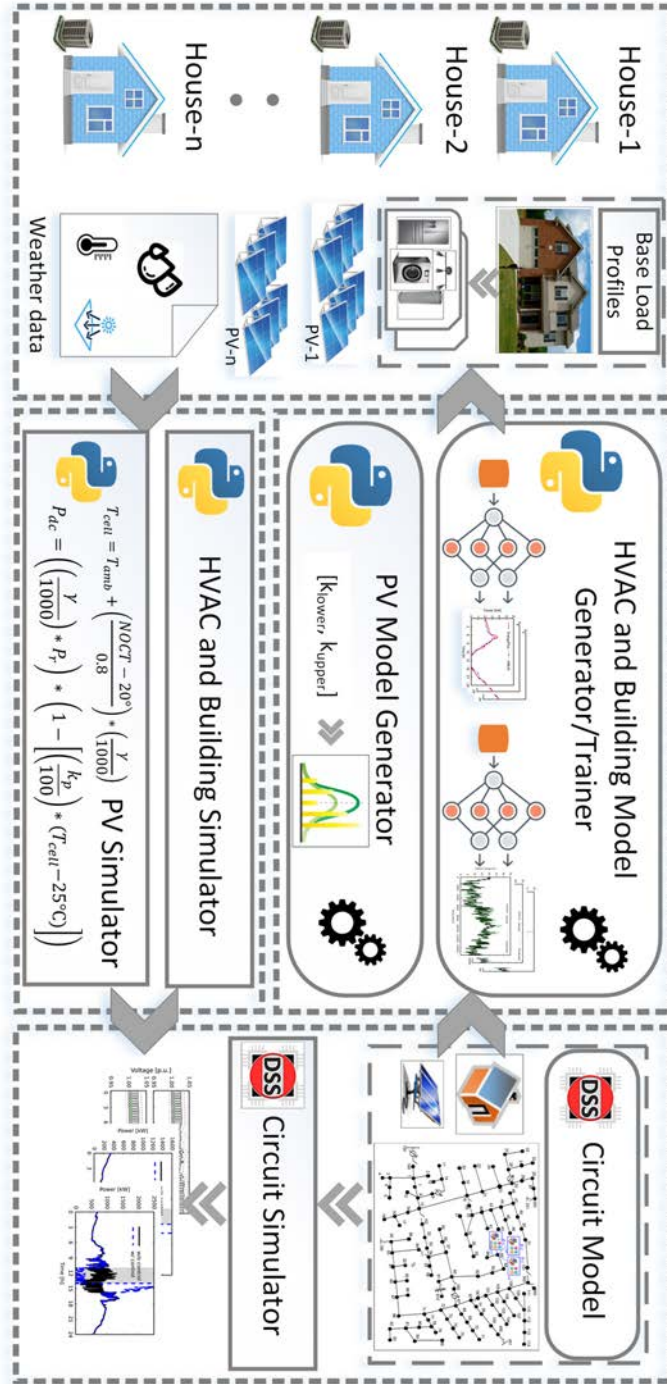


Figure 5.1: Schematic illustration of the newly developed co-simulation framework with multiple HVAC and building models and CTA-2045 control implementation. The framework employs ultra-fast HVAC system and building models with distinct base load energy profiles for typically human behavior-based loads. A representative community of individually unique building models for both electric power and indoor temperature may be simulated at the buildings and power system levels. It may also incorporate other DER types with controls, such as solar PV and BESSs.

widely available offer similar functionality when operated as generalized energy storage (GES) with additional appliance-specific constraints that are typically associated with occupant comfort and weather effects. Control strategies that coordinate multiple types of DERs, such as solar PV and GES, are an integral aspect of the smart grid and can be developed and tested through co-simulation [91, 96]. Simulation testbeds play an important role in both the development of such VPP control schemes and in the planning of DER deployment [34, 97].

This work employs a novel co-simulation framework that acts as a testbed for control strategies that may employ various GES systems, particularly HVAC systems, and DERs based on the Consumer Technology Association (CTA) 2045 standard [98, 99]. The evaluation of control cases at both the power system and individual building levels is enabled by the framework, which is facilitated by a physics-informed machine learning modeling procedure that is must faster than conventional white-box implementations.

Advanced control methodologies are utilized that incorporate HVAC system sequential phasing in batches of houses throughout the community and more gradual changes in setpoint temperatures. Also, the proposal of a multi-objective control optimization is provided with objectives to minimize targeted power peaks and possible resulting increases in total energy use. Independent variables for the optimization include “shed” and “load-up” control times for the HVAC systems, which are command types based on the CTA-2045 standard and made possible by GES characterization that inherently considers occupant thermal comfort.

This chapter discusses the development and application of a novel co-simulation

framework, DER and Power Distribution System (PDS) models, and control methodologies with the following objectives:

- Enable testing and study of DER control scenarios
- Evaluate improved power system operation, such as peak power shifting/shaving and DER coordination with increased utilization of local generation
- Identify opportunities for typical household appliances like HVACs to be employed as DERs
- Consider effects of control on occupants, such as change in thermal comfort, which may be a likely constraint in actual implementation
- Optimize control settings for VPP scenarios.

This chapter is substantially based on the following publications:

- **E. S. Jones**, *et al.*, “Co-simulation of Electric Power Distribution Systems and Buildings including Ultra-fast HVAC Models and Optimal DER Control,” 14p, 2023, *prepared for journal submission (April 2023)*.
- **E. S. Jones**, *et al.*, “Co-simulation of Smart Grids and Homes including Ultra-fast HVAC Models with CTA-2045 Control and Consideration of Thermal Comfort,” 2022 IEEE Energy Conversion Congress and Exposition (ECCE), Detroit, MI, USA, 2022, pp. 1-6, doi: 10.1109/ECCE50734.2022.9948200.

In section 5.2, the models for DER, including generators and energy storage, are established. Section 5.3 provides the operation of the DERs in aggregate at

the power system level considering different control and distribution-side generation scenarios. Section 5.4 formulates the optimization of HVAC system GES control settings. The results of the optimization and preceding central composite and full factorial simulation experiments are discussed in section 5.5. Having determined a “best compromise” set of optimal settings, section 5.6 further explores the effects of the control on individual buildings and occupants, and conclusions are provided in section 5.7.

5.2 Models for Buildings, Energy Storage, and PV Generation

A novel framework for co-simulation of DERs and PDSs is utilized as a testbed for control schemes, GES, and DER deployment (Fig. 5.1). The building models employed in the co-simulation framework are organized into four components: HVAC system, thermal building envelope, residential solar PV system, and base load (i.e., other home appliance electric load). As a basis for the HVAC and building components, three houses that are representative of a spectrum of energy efficiencies, from conventional performance to Near-Net-Zero Energy (NNZE), were modeled and calibrated in EnergyPlus [70, 100]. EnergyPlus is the U.S. Department of Energy’s flagship simulator for whole-building white-box simulation. It employs physics-based principles related to building construction as well as weather characteristics for the calculation of HVAC system energy use.

Through a new Python plugin, software was developed to synthesize many different EnergyPlus house models by varying internal HVAC and building characteristics of the base conventional EnergyPlus building model. A normal distribution of

key building characteristics spanning from the lower efficiency conventional house to highly efficiency NNZE house was used to ensure adequate and representative randomness between houses. Such HVAC system performance characteristics include the heating and cooling thermal energy capacities, coefficients of performance (COP), and air flow rates. The varied building thermal properties include conductivity, thickness, density, and specific heat of construction materials such as studs, insulation, and associated air cavities for walls and roofing as well as for attic trusses and additional ceiling insulation. Window U-factors and solar heat gain coefficients (SHGCs) were also considered.

All of the newly synthesized EnergyPlus models are then simulated for an example location and time period based on weather data to produce synthetic data of HVAC energy use and indoor building temperature for an entire community of individual houses. With this synthesized data, a Machine Learning (ML) process may be applied to train and develop new black and grey box versions through methods including Multi-Linear Regression (MLR), k-means clustering for weather grouping, and thermodynamic equations for specific heat conversions (Fig. 5.6) [101]. This process enables both ultra-fast simulation that is up to approximately 133 times faster than EnergyPlus as well as straightforward integration with other software as incorporated in the co-simulation framework.

The ML training procedure produces multiple models, which are satisfactorily accurate in capturing both the heating and cooling thermal energy of the HVAC system, as well as the indoor temperature of the building, while experiencing external weather effects. The inclusion of building indoor temperature enables the tracking

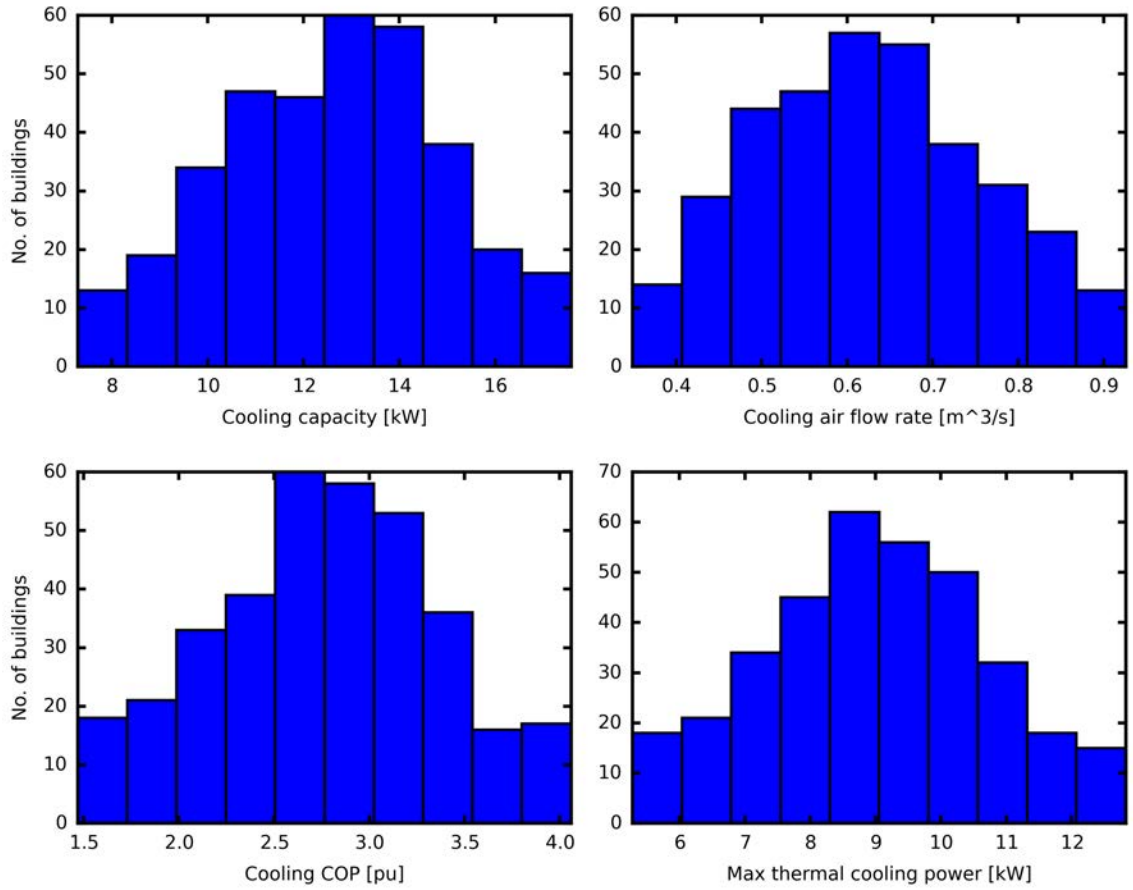


Figure 5.2: Histograms of HVAC cooling characteristics associated with the 351 synthesized EnergyPlus models from which the ML models were trained.

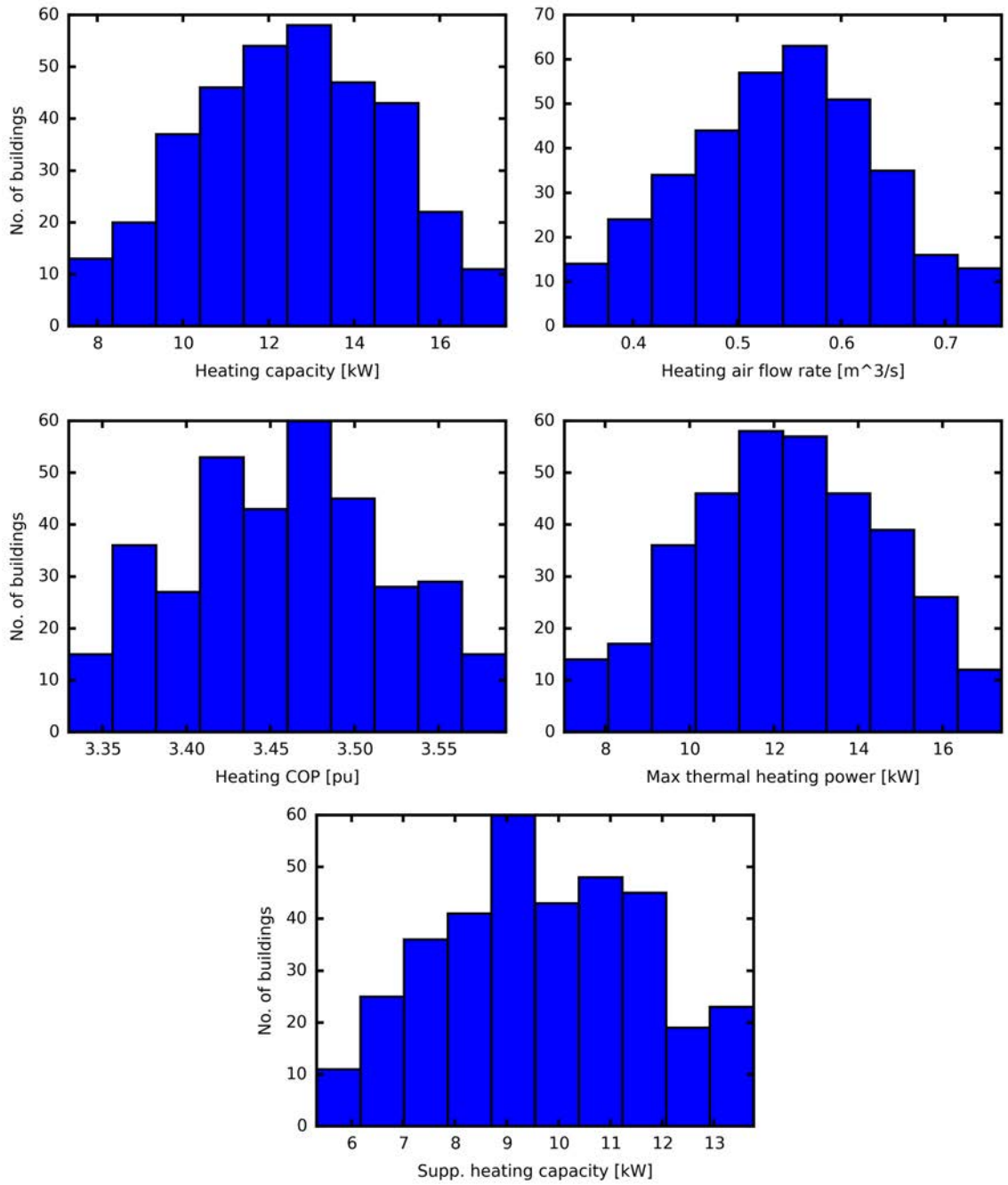


Figure 5.3: Histograms of HVAC heating characteristics associated with the 351 synthesized EnergyPlus models from which the ML models were trained.

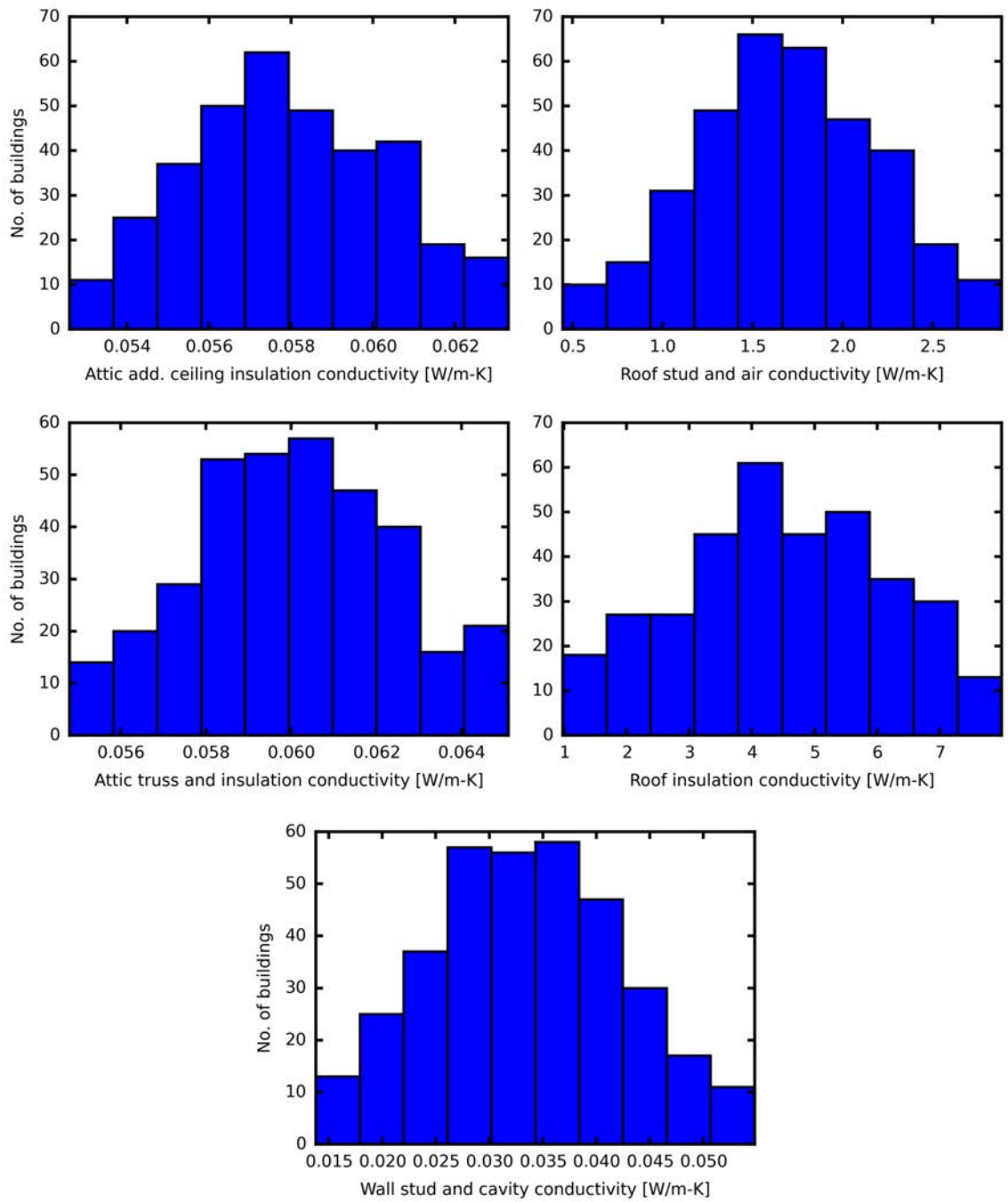


Figure 5.4: Histograms of conductivity values for different construction materials of the 351 synthesized EnergyPlus models from which the ML models were trained.

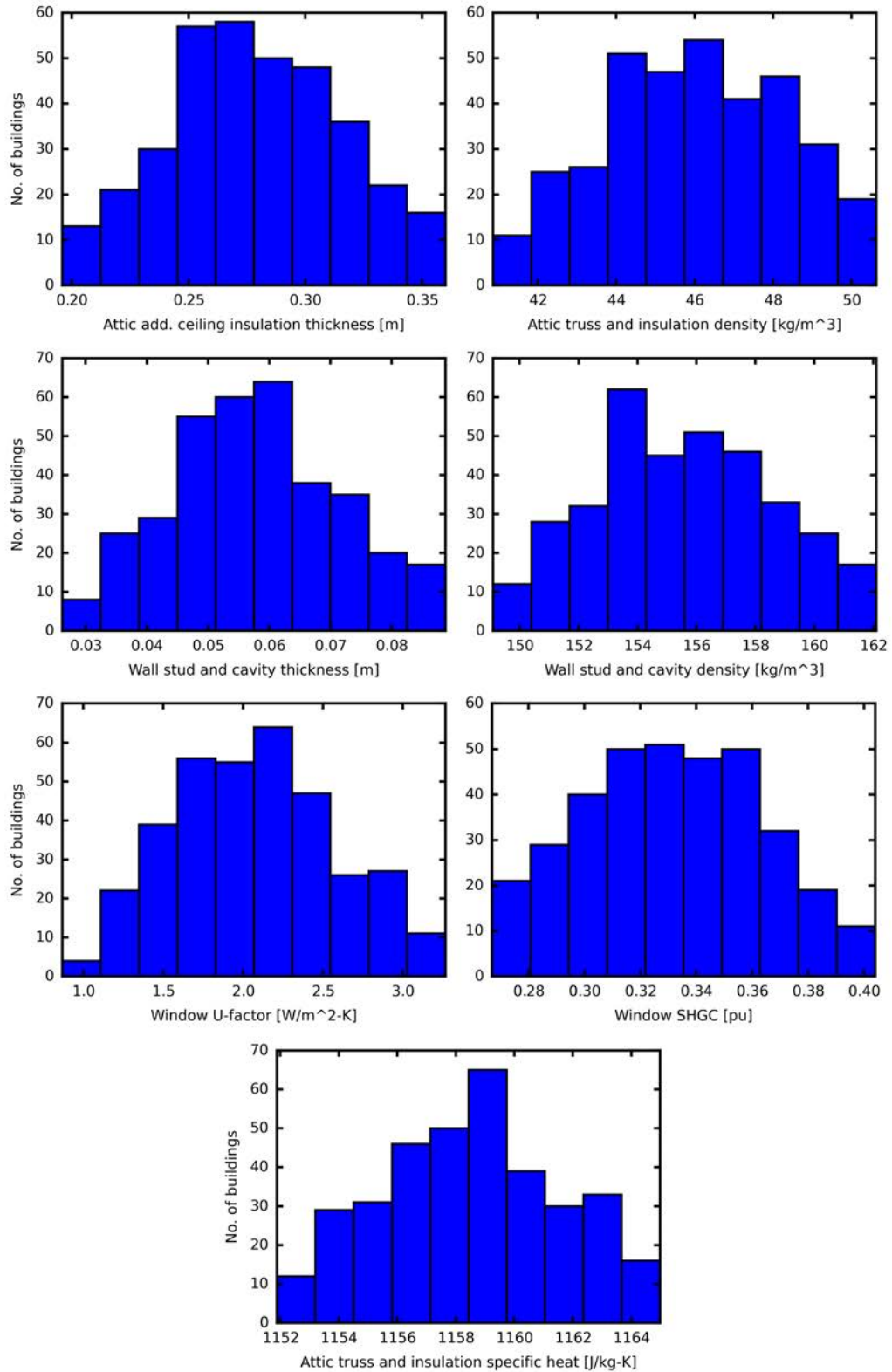


Figure 5.5: Histograms of thickness and density values for different construction materials as well as window efficiency metrics of the 351 synthesized EnergyPlus models from which the ML models were trained.

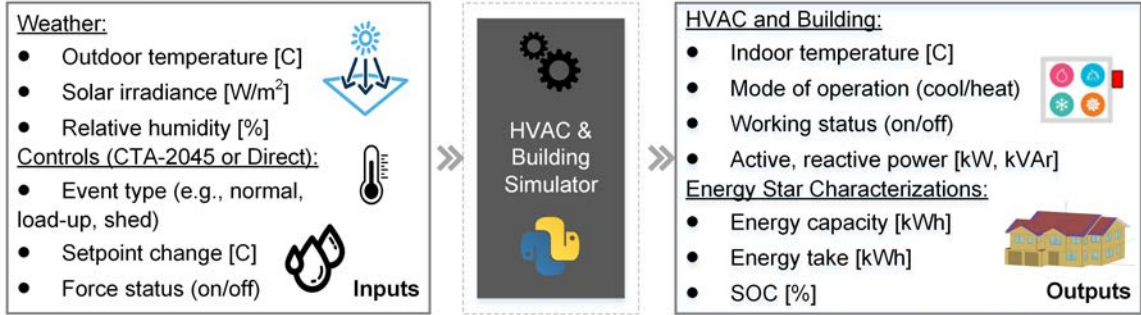


Figure 5.6: Schematic of HVAC and building time dependent simulator capable of executing both explicit and CTA-2045 commands, as well as providing Energy Star GES performance, such as electric energy capacity, energy take, and equivalent SOC.

and prediction of thermal comfort for occupants, which is a notable contribution and is integral for improved HVAC control. The ML models capture the thermal properties of the building and the HVAC system and their relationship with weather. As a result, the ultra-fast ML models are not limited to the location for which the original EnergyPlus input weather data is representative, which is an important and significant modeling contribution for VPP studies to be conducted across multiple locations and compared to determine optimal areas for control investment.

As part of the testbed, an HVAC and building simulator is custom-developed to utilize the ML models for co-simulation with a power PDS and are assigned to appropriate circuit nodes (Figs. 5.6). Simulation processes and control logic for the HVAC and building simulator is provided in Fig. 5.7, where t_d is indoor temperature deviation; t_s , setpoint temperature; t_i , indoor temperature; h_m , HVAC mode of operation; h_s , HVAC on or off status; t_{db} , the thermostat temperature dead-band; t_{tol} , the thermostat temperature tolerance; $p_{h,kW}$, the HVAC electric active power [kW], t_{in} , the indoor temperature of the next timestep; pf_h , the power factor of the HVAC

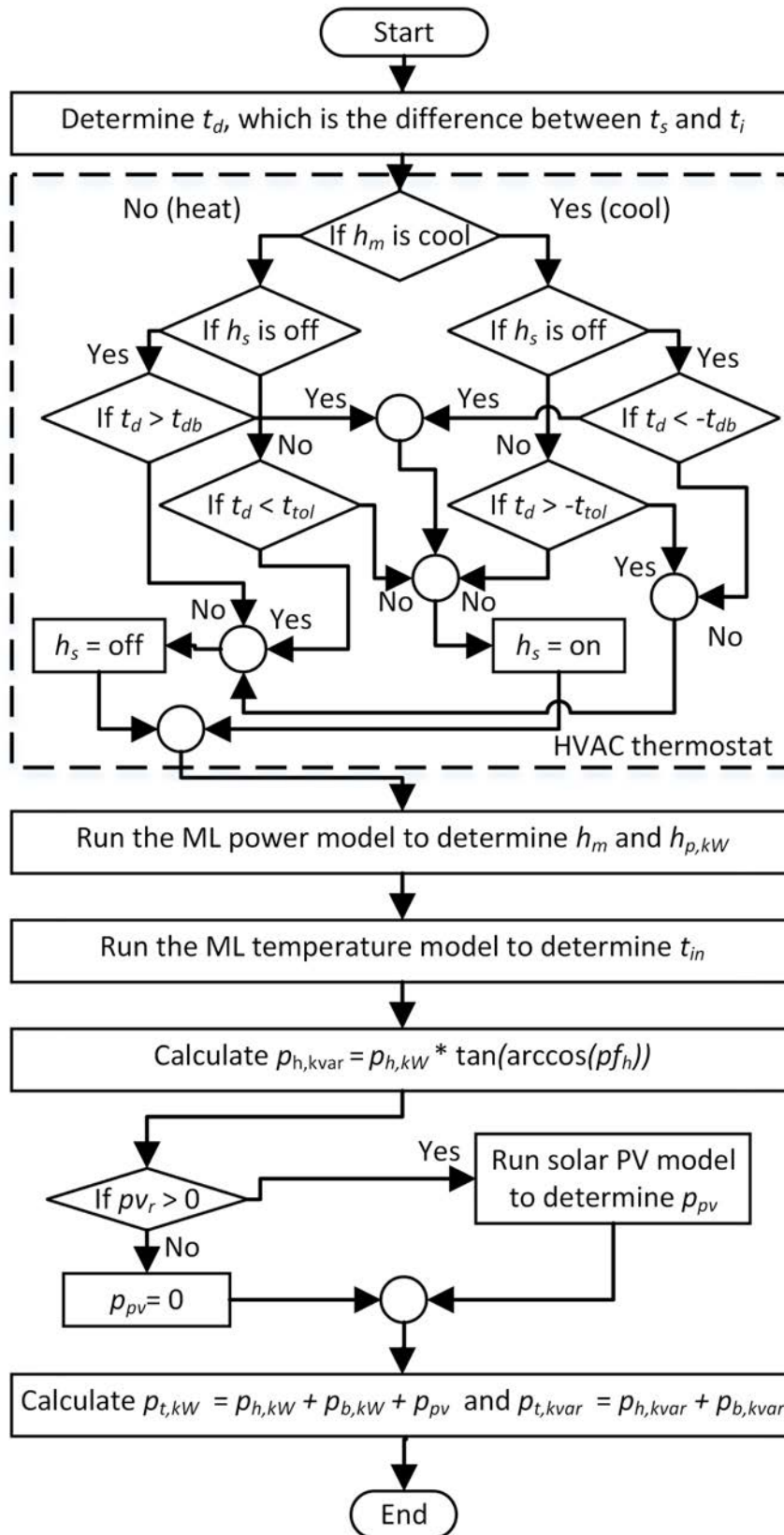


Figure 5.7: Flowchart for the HVAC and building simulator that employs ML HVAC models as well as the PV simulator.

system; $p_{h,kvar}$, the HVAC electric reactive power [kvar]; p_{v_r} , the rated power of the solar PV system [kW]; p_{pv} , the electric active power generated from the solar PV system; $p_{t,kW}$, the total electric active power of the building [kW]; $p_{t,kvar}$, the total electric reactive power of the building [kvar]; $p_{b,kW}$, the electric active power of the base load [kW]; $p_{b,kvar}$, the electric reactive power of the base load [kvar].

Residential solar PV systems may be assigned to the building models and simulated based on weather data through physical equations (Fig. 5.1). The PV simulator in the framework determines generated solar PV power ($p_{g,pv}$) based on the model established in section 4.6. Unlike HVAC and PV systems, other typical household appliances and devices are primarily human behavior-based and not dominantly weather dependent. Therefore, each building model may be assigned a random daily profile of energy use for other typical house loads, including water heaters, lights, and electronics. The schedules employed for the following studies were based on minutely household energy use data sourced from the Electric Power Research Institute (EPRI) SHINES project [102].

5.3 Power System and DER Operation

The co-simulation framework was utilized to simulate a very large subdivision in the U.S. with the buildings randomly populated at appropriate connection nodes throughout a modified IEEE 123-bus test PDS (Fig. 5.8) [103]. The initial load allocation of the test power system was considered by assuming 10kW of the original peak load at each connection node corresponds to a single building. This method resulted in 351 uniquely generated buildings, 52 (15%) of which having a BTM solar

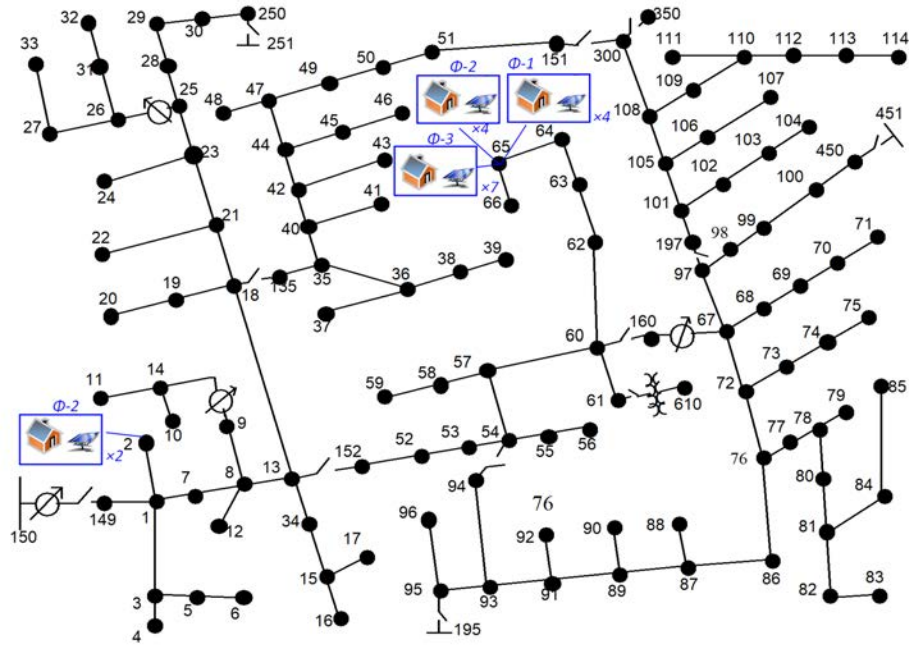


Figure 5.8: The circuit diagram for the modified IEEE 123-bus test system. The original circuit has a peak load of 3.6MW, 1.3MVAR and is to be representative of a very large residential subdivision in the U.S.

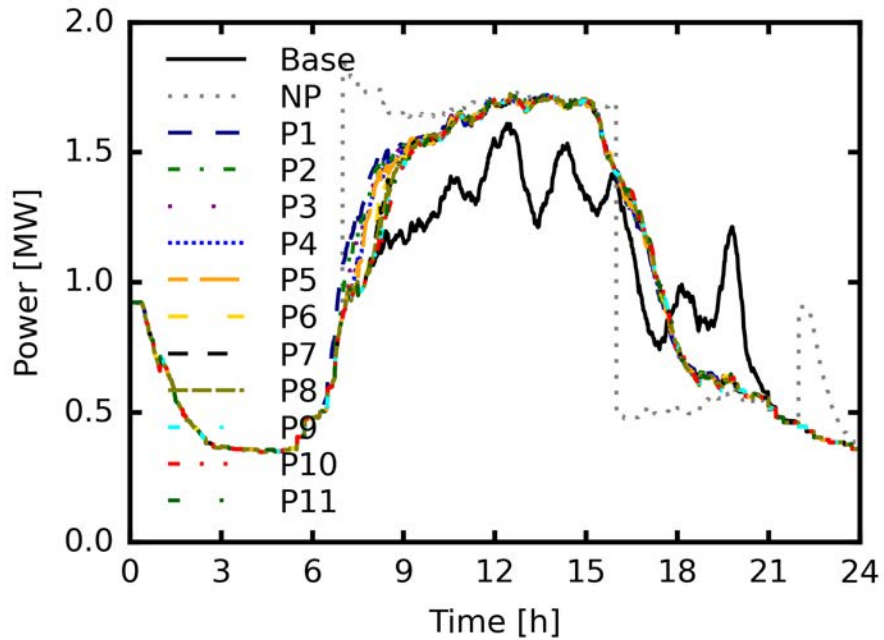


Figure 5.9: PDS total active power for the baseline and control cases. This is an aggregation of all building loads minus the power losses across the PDS without considering any contributions from PV generation.

PV system with typical power ratings randomly selected between 3 and 7.5kW. The houses with BTM PV generation capability were distributed throughout the power system to represent gradual adoption patterns of the technology.

For the simulated example day, minutely solar irradiance and outdoor temperature data collected in the southeast U.S. is employed as input to the models (Fig. 5.10). The baseline simulation case does not include any VPP control, and the HVAC systems operated as they normally would in accordance with their indoor temperature setpoints and associated building thermal properties. At the PDS level, the total power ramped up in the morning as both the solar irradiance and outdoor temperature increased (Fig. 5.9). HVAC systems constitute almost half of the energy used by typical residences and use more energy as indoor temperature changes [30]. As this change in temperature reduced in the midday, the HVAC systems settle into normal operation and maintain indoor temperature near setpoint.

Total system power ramped down as the sun set with a subsequent peak likely due to occupant arrival in the evening. This secondary evening peak is of particular interest as Electric Vehicle (EV) charging in scenarios of higher penetration may cause a significant system-wide power increase at this time [104]. Additionally, the longer midday peak may invert as distributed solar PV becomes more prevalent, which further contributes to the concern of the secondary evening peak (Figs. 5.10 and 5.11). The reshaping of the residential load profile from higher DER penetration levels, including contributions from solar PV and EVs, may be alleviated by VPP control of other residential loads, such as HVAC systems.

Considering occupant thermal comfort is a significant challenge in conventional

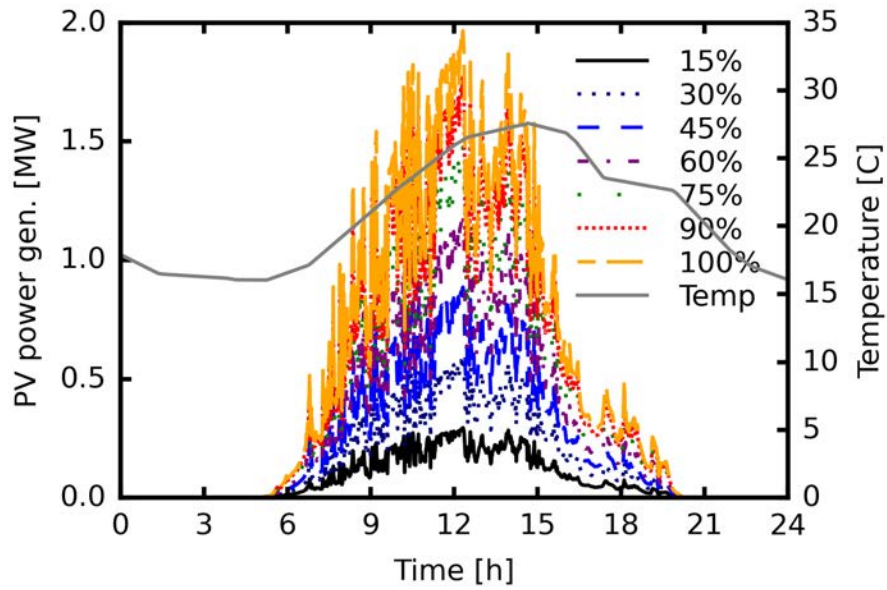


Figure 5.10: Results for the PDS total solar PV power generation for the simulated 15% and estimated solar PV penetration cases of up to 100%. The variability in solar PV power generation is caused by variability in irradiance.

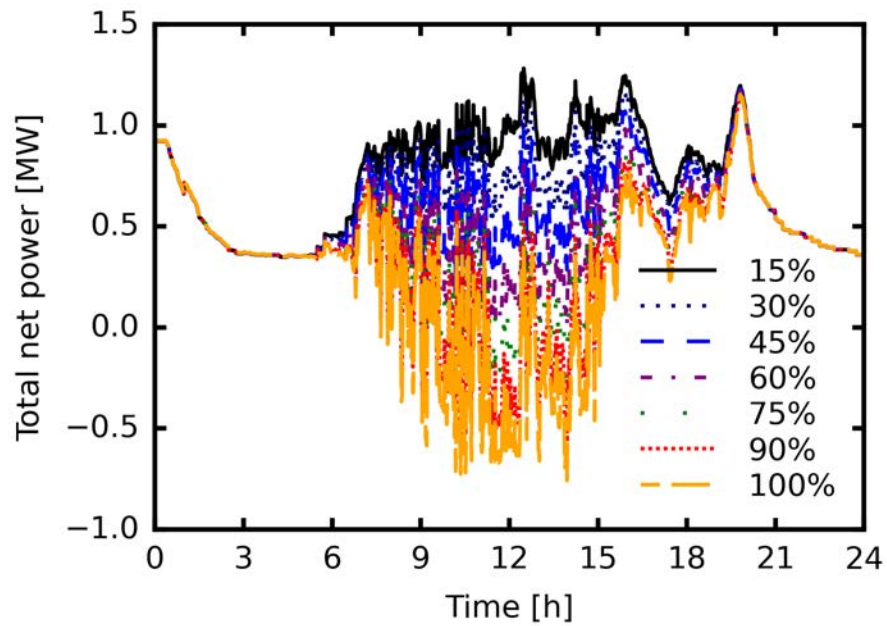


Figure 5.11: Results for the PDS total net power for the simulated 15% and estimated solar PV penetration cases of up to 100%.

HVAC control implementations due to the complex relationship between weather, HVAC power, and indoor temperature, which is unique for every building. Incorporating indoor temperature into VPP control schemes that leverage HVAC systems as DER is necessary to prevent violation of typical thermal comfort limits for occupants. Improved control methods through the CTA-2045 standard for DER control types and GES characterization based on Energy Star definitions address the issue through analogies of equivalent State-Of-Charge (SOC) and energy storage capacity [31, 105]. The equivalent SOC and energy storage capacity at time t of an HVAC system may be respectively defined by:

$$soc_h(t) = \frac{\theta_{max} - \theta_i(t)}{\theta_{max} - \theta_{min}}, \quad (5.1)$$

$$e_{c,h}(t) = \overline{e_{h,c}} \cdot (1 - soc_h(t)), \quad (5.2)$$

where the θ_{max} and θ_{min} are the maximum and minimum indoor temperatures, respectively; $\theta_i(t)$, the indoor temperature at time t ; $\overline{e_{h,c}}$, the input electric energy required for the HVAC system to reduce indoor temperature from θ_{max} to θ_{min} .

During simulation, the HVAC system and building models that are generally illustrated in Fig. 5.6 determine their corresponding $e_{c,h}(t)$ internally upon initialization based on their thermal properties and ability to maintain indoor temperature over time. The recalculation of $e_{c,h}(t)$ at multiple timesteps throughout simulation would capture the system's dependency on weather in this regard, which is analogous to effects also experienced by conventional electric battery energy storage systems, such as changes in capacity and self discharge.

When a CTA-2045 command is issued, such as a “shed” or “load-up”, the controller adjusts individual building indoor temperature setpoints based upon their $e_{c,h}(t)$, which are determined by considering building thermal properties and typical ASHRAE standard occupant thermal comfort limits [31]. Calculating the setpoint change in this way considers the individual building characteristics, thereby enabling more accurate prediction of the maximum energy that may be used from the demand-side without violation of indoor temperature limits. By incorporating the consideration of occupant thermal comfort directly into the controls, the degree to which occupant comfort is violated now correlates with the accuracy of the building $e_{c,h}(t)$ estimations and the θ_{max} and θ_{min} settings.

5.4 Problem Formulation and Algorithms for Optimal VPP Control of HVAC Systems

A VPP control scenario is proposed that employs the CTA-2045 command types to reduce the evening peak power. A “load-up” is planned before the evening to pre-cool the houses while they are the least occupied to provide a more sustained “shed” that will turn the HVAC systems off during the evening peak time window. The indoor temperature setpoint adjustments applied by these controls are issued incrementally over the first thirty minutes of the control period to provide a gradual change in power over time.

Additionally, these advanced controls employ phasing before and after active periods, by which batches of randomly selected HVAC systems are sequentially engaged and disengaged from the control as illustrated in Fig. 5.12 [31]. The box-and-whisker

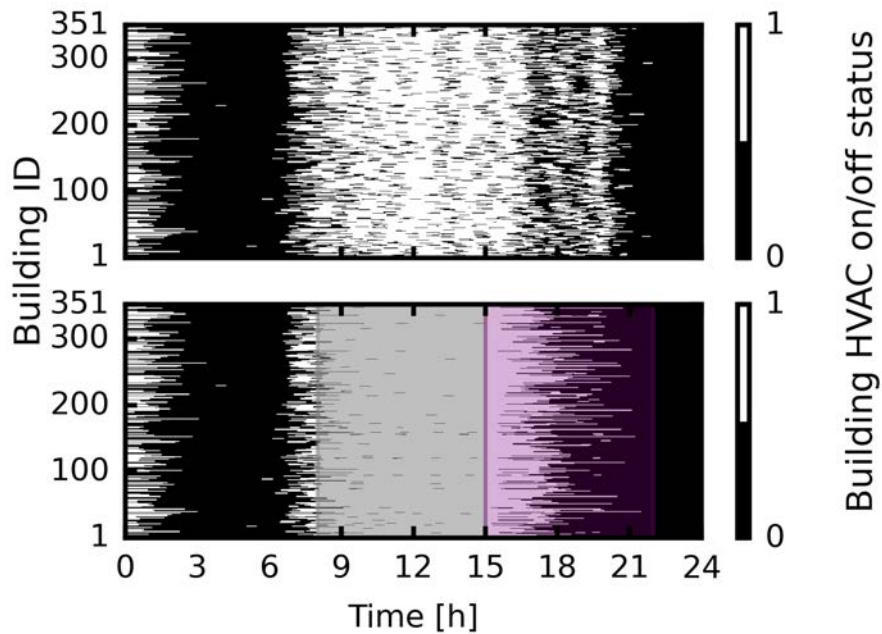


Figure 5.12: Simulation results for individual on/off statuses for HVACs to show control phasing in the baseline case (top) and in case P6 (bottom) for both the baseline and P6 cases. The “load-up” and “shed” event windows are shaded in light gray and purple, respectively. This format is replicated in following figures.

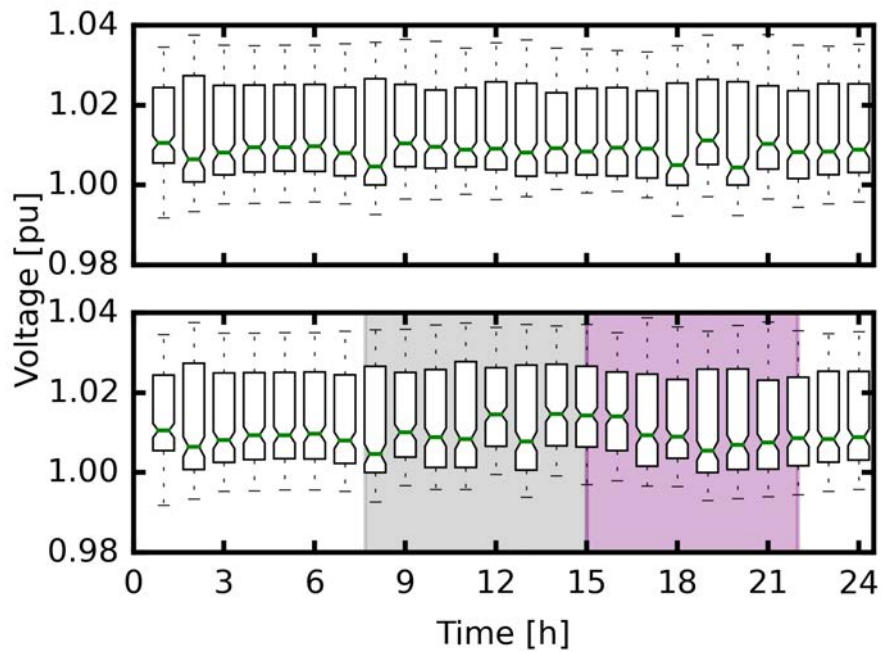


Figure 5.13: Simulation results hourly average PDS bus voltages for both the baseline and P6 cases.

format employed throughout is such that the box extends from the first quartile to the third quartile with a green line at the median. Whiskers extend from the box by 1.5x the inter-quartile range, and flier points are those past the end of the whiskers.

The improved control functionality prevents power spikes that would have occurred otherwise as illustrated with example case NP in Fig. 5.9. In such a case, all of the HVAC systems engaged and disengaged simultaneously as soon as the “load-up” and “shed” controls were issued, thereby causing a large spike and steep drop in total PDS power. Another power spike occurred in the evening after the “shed” control ended as the HVAC systems resumed cooling all at once (Fig. 5.21).

To ensure best performance, the controls are formulated as a multi-objective optimization to minimize both the total PDS peak power during the evening time period ($p_{a,t=t_{ep}}$) and possible resulting increase in total system energy use (e_d) over the example day, which are formally defined as:

$$\min \left[p_{a,t=t_{ep}} = \sum_{i=1}^{n_l} (w_{a,l,i}) + \sum_{j=1}^{n_t} (w_{a,x,j}) + \sum_{k=1}^{n_d} (p_{a,d,k}) \right], \quad (5.3)$$

$$\min \left[e_d = \sum_{i=1}^{n_t} (p_{a,t=i}) \right], \quad (5.4)$$

where n_l , the total number of lines; $w_{a,l,i}$, the active power losses over line number i ; n_t , the total number of transformers; $w_{a,x,j}$, the active power losses at transformer number j ; n_d , the total number of loads; $p_{a,d,i}$, the active power demand at load number i ; t_{ep} , the moment of maximum power in the evening peak time window of 5:30 to 9:00; n_t , the total number of timesteps (minutes) in the day.

A e_d value greater than the baseline case indicates that the energy used during

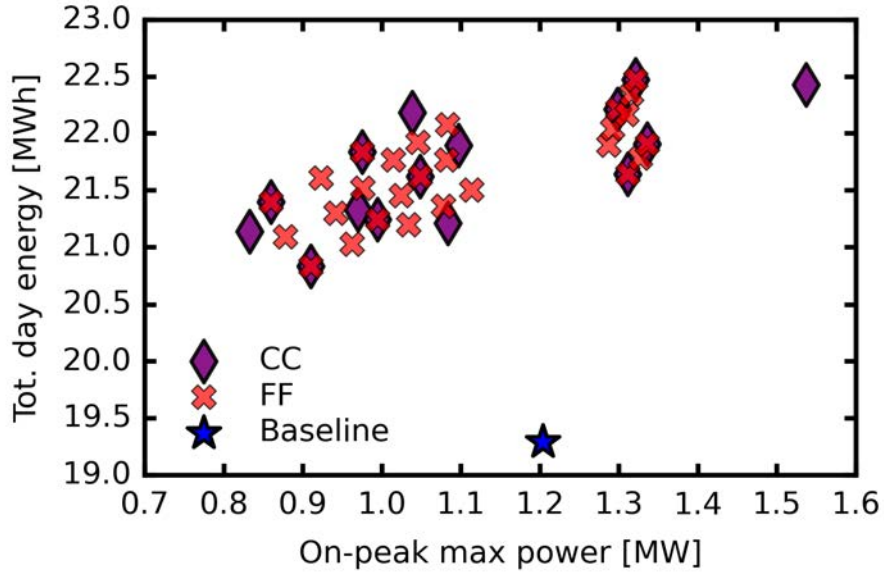


Figure 5.14: Resulting evaluation of optimization objectives for both the central composite (CC) and full factorial (FF) DOEs with respect to the baseline case.

the “load-up” command is greater than that of the avoided energy use during the “shed” command. Such a scenario can present a trade-off between $p_{a,t=t_{ep}}$ and e_d as both are to be minimized and compete to some degree. In this case, a Pareto set of best settings is expected to be determined by the optimization.

The independent variables of the control optimization include the “load-up” start time, the control transition time, and the “shed” end time. To establish independent variable bounds, a central composite and full factorial Designs Of Experiments (DOE) with response surfaces were performed (Figs. 5.14 and 5.15). The response surfaces for both the central composite and full factorial suggest the minimums for e_d and $p_{a,t=t_{ep}}$ are achieved with “load-up” start, control transition, and “shed” end times of 8:00, 15:00, and 22:00, respectively. Based on the DOEs, $p_{a,t=t_{ep}}$ is significantly less dependent upon “load-up” start time than the other independent variables.

The non-dominated sorting genetic algorithm (NSGA) III is utilized for the full

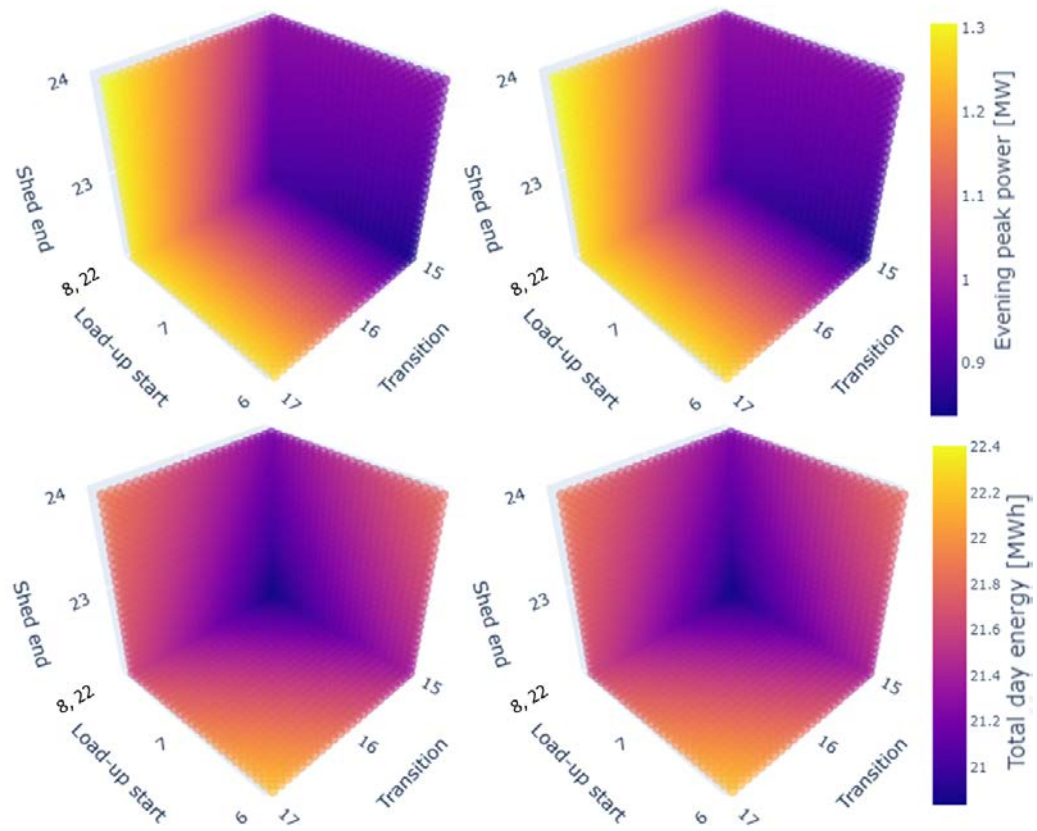


Figure 5.15: Response surfaces for the central composite (left) and full factorial (right) DOEs that captures the relationships between input control time settings and the objectives.

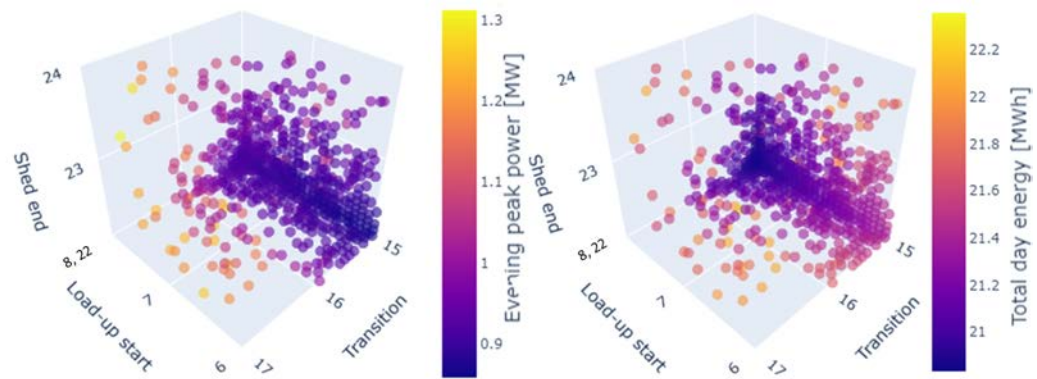


Figure 5.16: Four dimensional representations of the objective evaluations for the optimization results, which include over 750 designs.

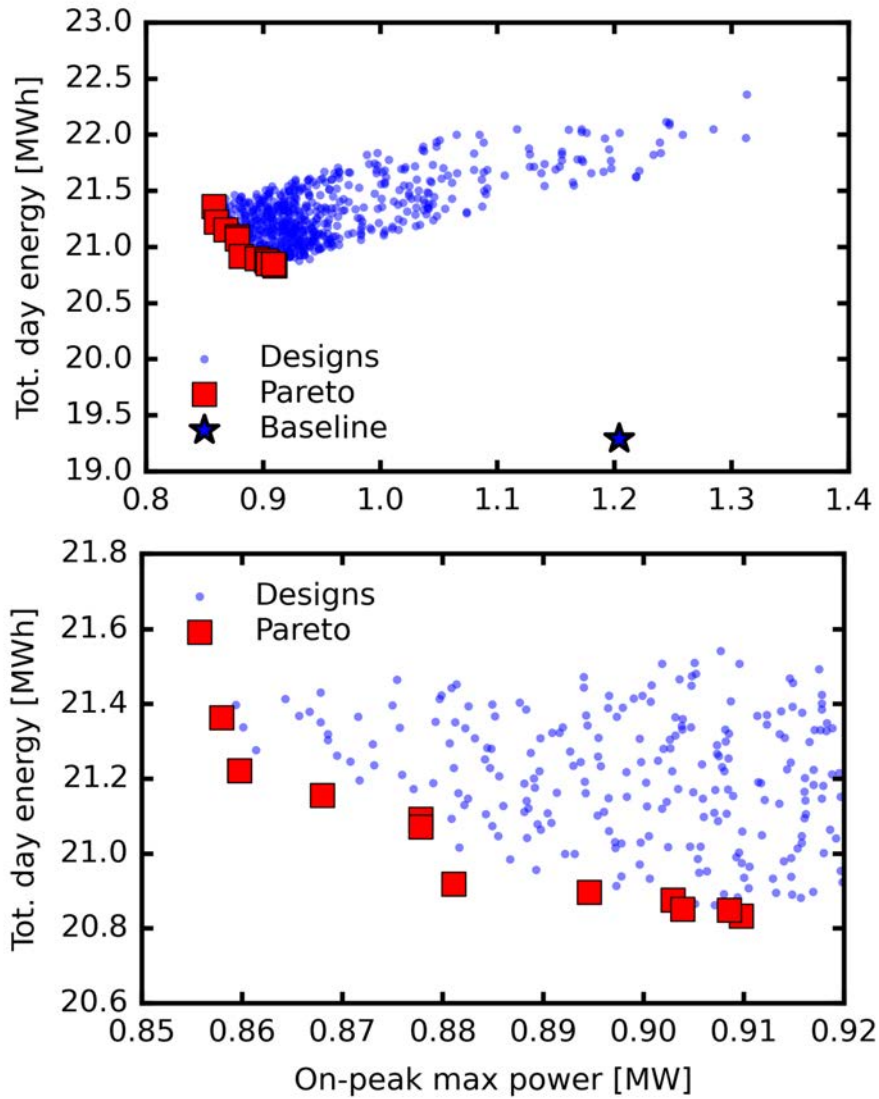


Figure 5.17: Resulting (top) objective evaluations and (bottom) a cropped view of all cases simulated during the NSGA-III optimization with respect to the baseline case and with the Pareto front of the eleven (11) best cases indicated.

Table 5.1: Results of optimal designs from the Pareto set and the baseline cases, including the maximum power during the evening peak (on-peak) as well as total energy for the full day, the on-peak time window, and off-peak time window.

Case	Base	P1	P2	P3	P4	P5	P6	P7	P8	P9	P10	P11
On-peak max power [MW]	1.20	0.86	0.86	0.87	0.88	0.88	0.88	0.89	0.90	0.90	0.91	0.91
Tot. day energy [MWh]	19.29	21.36	21.22	21.16	21.09	21.07	20.92	20.90	20.88	20.85	20.83	20.85
Tot. on-peak energy [MWh]	2.97	2.19	2.19	2.19	2.20	2.19	2.20	2.20	2.20	2.20	2.20	2.21
Tot. off-peak energy [MWh]	16.32	19.17	19.03	18.97	18.90	18.88	18.72	18.70	18.68	18.65	18.63	18.64

Table 5.2: The control time settings and resulting percent change with respect to the baseline case for all simulated cases in terms of maximum power during the evening peak (on-peak) as well as total energy for the full day, the on-peak time window, and off-peak time window.

Case	P1	P2	P3	P4	P5	P6	P7	P8	P9	P10	P11
Load-up start time	6:05	6:30	6:45	7:00	7:05	7:40	7:45	7:50	7:55	8:00	8:00
Control transition time	15:00	15:00	15:00	15:00	15:00	15:00	15:00	15:00	15:00	15:00	15:00
Shed end time	22:00	22:00	22:00	22:00	22:00	22:00	22:00	22:00	22:00	22:00	22:05
On-peak max power [%]	-28.75	-28.60	-27.91	-27.10	-27.10	-26.83	-25.70	-25.01	-24.93	-24.45	-24.55
Tot. day energy [%]	10.73	9.99	9.65	9.32	9.21	8.42	8.31	8.20	8.07	7.98	8.06
Tot. on-peak energy [%]	24.75	23.70	23.27	22.88	22.82	22.06	21.98	21.86	21.73	21.68	21.68
Tot. off-peak energy [%]	-4.40	-4.32	-4.21	-3.96	-3.95	-3.45	-3.42	-3.33	-3.27	-3.21	-2.93

optimization with independent variable bounds of 6:00-8:00, 15:00-17:00, and 22:00-24:00 for the “load-up” start, control transition, and “shed” end times, respectively, in increments of five (5) minutes [59]. Comprised of over 750 simulation cases, the optimization confirms the relationships established by the central composite and full factorial DOEs (Fig. 5.18). The dependency of $p_{a,t=t_{ep}}$ on “load-up” start time is more evident in the full optimization and opposes the objective to minimize e_d . Therefore, a Pareto front of eleven (11) best control settings is determined that showcases the inverse relationship between max power during the evening peak ($p_{a,t=t_{ep}}$) and total day energy use (e_d) (Figs. 5.17 and 5.18).

5.5 Case Study and Discussion of Optimal Control Settings

The Pareto set of optimal control settings provides designs that reduce $p_{a,t=t_{ep}}$ within a range of 24.45% and 28.75% by enacting the “shed” command (Tables 5.1

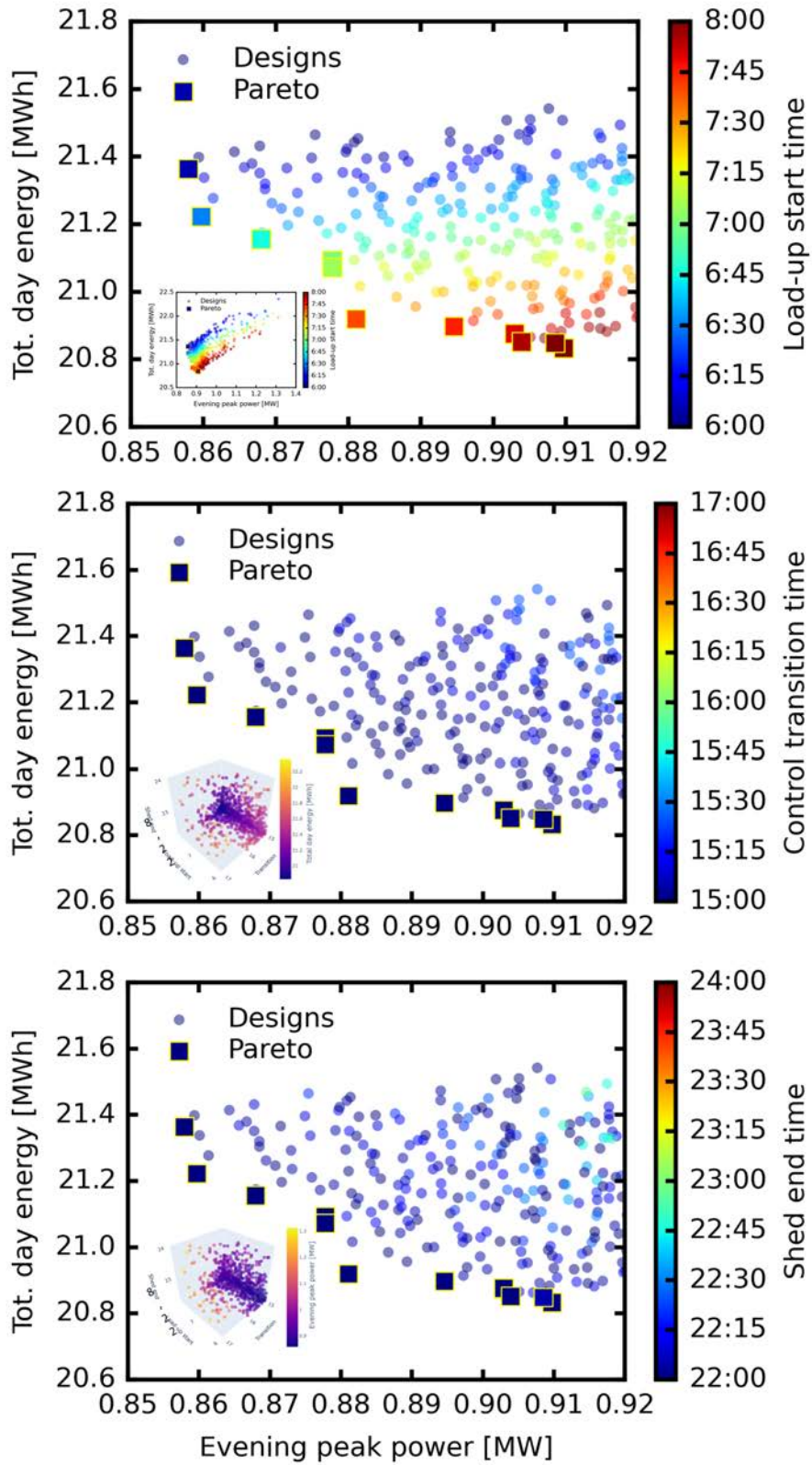


Figure 5.18: Relationships between the two (2) objectives and the three (3) independent variables of control times for all simulated cases during the optimization.

Table 5.3: Total energy during the “load-up” and “shed” time windows, which are different for each case based on the input time settings, with and without the controls active.

Case	P1	P2	P3	P4	P5	<i>P6</i>	P7	P8	P9	P10	P11
Load-up w/ ctrl [MWh]	11.78	11.44	11.22	10.95	10.86	<i>10.15</i>	10.05	9.95	9.84	9.73	9.73
Load-up w/o ctrl [MWh]	9.44	9.24	9.10	8.91	8.84	<i>8.32</i>	8.24	8.16	8.08	8.00	8.00
Shed w/ ctrl [MWh]	5.82	5.83	5.83	5.85	5.85	<i>5.88</i>	5.88	5.89	5.89	5.89	5.95
Shed w/o ctrl [MWh]	6.09	6.09	6.09	6.09	6.09	<i>6.09</i>	6.09	6.09	6.09	6.09	6.13

and 5.2). Such significant reduction in $p_{a,t=t_{ep}}$ is in part enabled by the pre-cooling of buildings through the “load-up” command, which, in these cases, increased e_d by 7.98% to 10.73%. Of the considered optimal control designs, P1 yielded the most reduction in $p_{a,t=t_{ep}}$ at 1.03MW (28.75%) and experienced the largest increase in e_d of 2.07MWh (10.73%) during “load-up” with respect to the baseline case. P10 represents the other extreme with a $p_{a,t=t_{ep}}$ reduction and e_d increase of 0.29MW (24.45%) and 1.54MWh (7.98%), respectively. The “best compromise” case of P6 achieved a $p_{a,t=t_{ep}}$ reduction of 0.32MW (26.83%) with a e_d increase of 1.63MWh (8.42%). The results of the two most extreme cases, P1 and P10, are emboldened, and the “best compromise” case, P6, is both emboldened and italicized in tables 5.1, 5.2, and 5.3.

If residential energy storage systems (RESSs) were to be utilized instead to realize the results of P6, each house would require an approximate RESS capacity of 5.2kWh, or 1.83MWh in total, based on the additional energy used in P6 during the “load-up” control window provided in Table 5.3. With a typical Tesla Powerwall as a currently available example RESS, which is rated at 13.5kWh in capacity [106], around 136 out of the 351 simulated houses would need to adopt the technology in order to achieve the same effect. Assuming a typical RESS round-trip efficiency of 86%, the RESSs would expend around 0.26MWh in total e_d as losses [107]. The e_d increase of 1.63MWh for

P6 may be recuperated over the following day(s) through specific controls, such as extended and more gradual “shed” commands.

From the utility perspective, the “load up” during midday is timed such that energy generated by solar PV may be better utilized locally. Considering PDS configurations with high penetration levels of solar PV and utility-scale renewable generation, improved BTM PV utilization by loading-up midday would also reduce total associated carbon emissions even with increased e_d as it would essentially replace higher carbon-emitting generation that would have been needed during the eliminated evening peak.

For the control and baseline cases at different levels of penetration, table 5.4 provides the BTM PV utilization factor, which represents the percentage of solar PV generation used BTM and not fed back to the utility. Generated energy begins to exceed the load demand and is fed back onto the transmission system once solar PV adoption surpasses 45% of the PDS. Each of the control cases improved BTM solar PV utilization similarly by approximately 3% to 8% across penetration levels. To further elaborate upon the features of the co-simulation framework as well as the effects of the optimal VPP controls at both the power system and individual occupant levels, the results of the “best compromise” control case P6 are discussed in further detail in the next section and considered as the primary example.

5.6 Individual Building and Occupant Effects

As the individual buildings experience large changes in indoor temperature due to quickly increasing outdoor ambient temperature and solar irradiance as the sun rises

Table 5.4: The BTM solar PV utilization for the baseline and control cases at different levels of penetration.

Pen./ Case	Base	NP	P1	P2	P3	P4	P5	P6	P7	P8	P9	P10	P11
15%	100.00	100.00	100.00	100.00	100.00	100.00	100.00	100.00	100.00	100.00	100.00	100.00	100.00
30%	100.00	100.00	100.00	100.00	100.00	100.00	100.00	100.00	100.00	100.00	100.00	100.00	100.00
45%	100.00	100.00	100.00	100.00	100.00	100.00	100.00	100.00	100.00	100.00	100.00	100.00	100.00
60%	99.86	99.93	100.00	100.00	100.00	100.00	100.00	100.00	100.00	100.00	100.00	100.00	100.00
75%	91.36	98.30	99.05	99.05	99.05	99.18	99.12	98.98	98.91	98.98	99.05	99.05	99.05
90%	85.96	92.20	93.12	93.12	93.18	93.25	93.25	92.86	92.80	92.80	92.94	92.94	92.94
100%	84.27	88.96	89.57	89.71	89.58	89.38	89.45	89.22	89.22	89.29	89.09	89.10	89.10

in the morning, HVAC systems will use more energy to maintain indoor temperature setpoints (Figs. 5.11, 5.21, and 5.20). Once the transition into daytime is complete, the HVAC systems settle into normal operation and maintain the indoor temperature with less energy use since outdoor temperature experiences relatively small change. As shown in Fig. 5.11, BTM solar PV generation exacerbates the additional peak in the evening.

The “load-up” and “shed” command types enact energy shifting rather than saving. They are useful for reducing total system power peaks and shifting energy in time such that BTM renewable energy may be better utilized. HVAC systems will increase energy use as the “load up” event decreases the setpoint temperature. This pre-cooling creates a larger range for temperature to increase during “shed”, which allows for a more sustained and significant drop in total system power during the on-peak time window (Fig. 5.21).

Upon control issuance, HVAC systems respond independently to newly assigned indoor temperature setpoints that are based upon their own unique electric energy capacities and equivalent SOC, which innately considers occupant comfort limits according to ASHRAE standards [31]. Indoor temperatures change at different rates between houses due to differing thermal properties and construction until equivalent

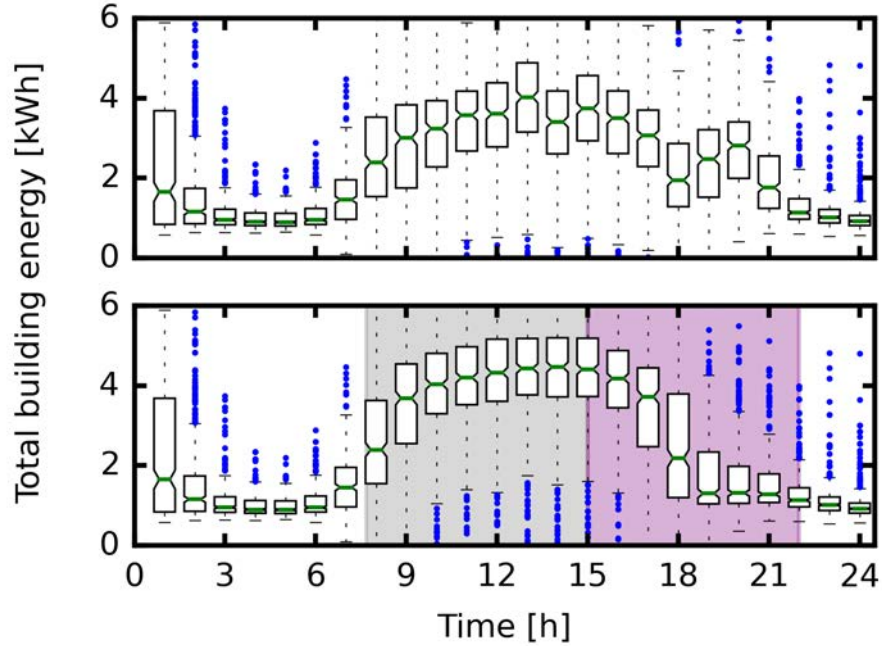


Figure 5.19: Total energy use for the baseline and P6 cases.

SOC reaches a maximum bound (Figs. 5.21, 5.22). Since the equivalent SOC of the individual buildings is dependent upon their estimated energy capacities, indoor temperatures may deviate from thermal comfort bounds for a short time. Such violations may be mitigated by improving the energy capacity estimation or by implementing tighter minimum and maximum SOC bounds.

5.7 Summary

A novel co-simulation framework is employed to optimize Virtual Power Plant (VPP) controls that leverage Heating, Ventilation, and Air-Conditioning (HVAC) systems as Generalized Energy Storage (GES) to reduce a targeted PDS power peak, while better utilizing Behind-The-Meter (BTM) solar Photo-Voltaic (PV) energy generation locally. The incorporation of HVAC system phasing and gradual setpoint

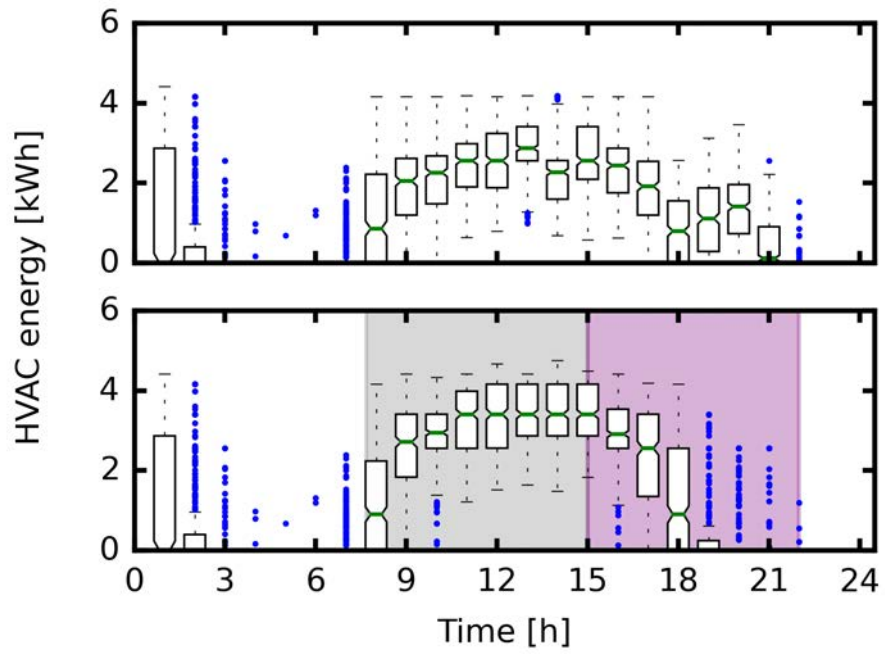


Figure 5.20: HVAC energy use only for the baseline and P6 cases.

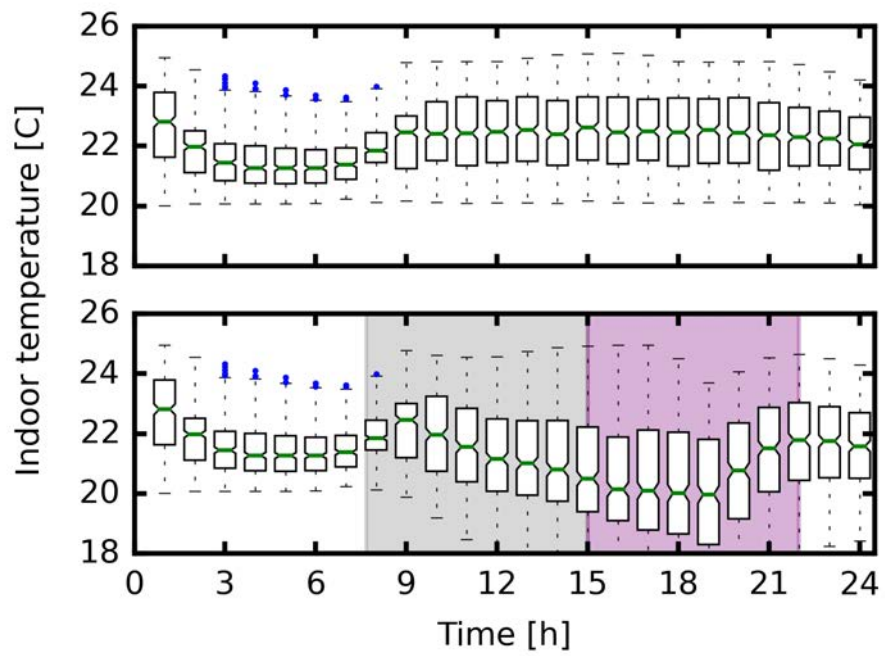


Figure 5.21: Hourly average indoor temperatures of all buildings for the baseline and P6 cases.

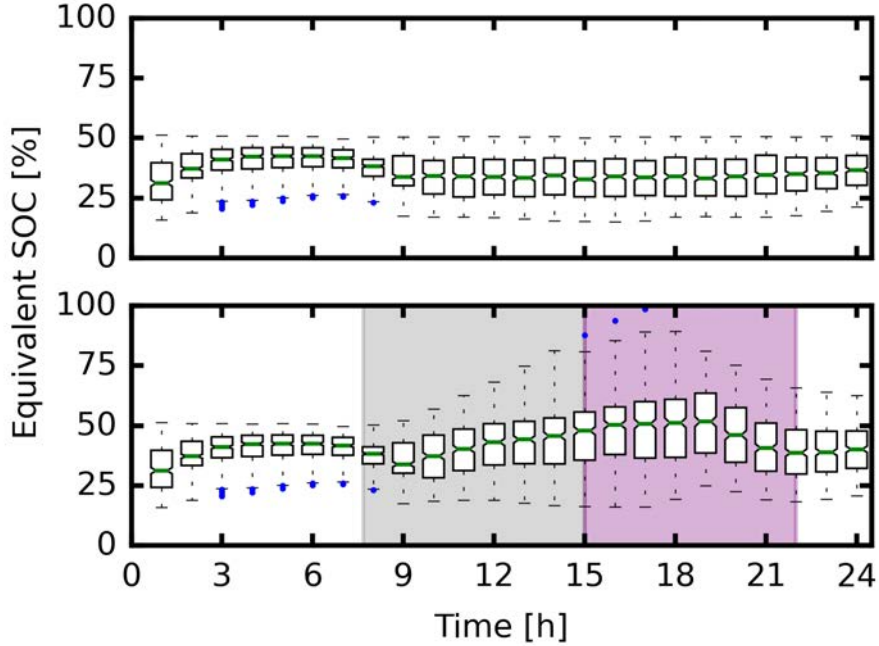


Figure 5.22: Hourly equivalent SOC, which is inversely related to indoor temperature, of all buildings for the baseline and P6 cases.

change functions effectively prevents power system peaking or dropping from start or completion of controls. The minimization of on-peak maximum power reduction ($p_{a,t=t_{ep}}$) and possible resulting total day energy use increase (e_d) can compete in certain scenarios. Therefore, the optimization produced a Pareto set of best designs with control settings that achieve a $p_{a,t=t_{ep}}$ of 24.45% to 28.75% and experience an increase in e_d of 7.98% to 10.73%. Each design yields improved BTM solar PV utilization by approximately 3% to 8% because of the “load-up” timing.

From among the best control designs, P6 offers a “best compromise” with a $p_{a,t=t_{ep}}$ reduction of 0.32MW (26.83%) and a e_d increase of 1.63MWh (8.42%). If Residential Energy Storage Systems (RESSs) were to be utilized instead to realize the same results as P6 with HVAC system control only, they would require a combined capacity of approximately 1.83MWh. Assuming a typical RESS round-trip efficiency of 86%,

the RESS would expend around 0.26MWh in e_d as losses. In contrast, the 1.63MWh increase in e_d in P6 to achieve a more significant $p_{a,t=t_{ep}}$ may be recuperated over the following day(s) through specific controls. For the P6 optimal control case, the individual building and occupant effects are observed, including indoor temperature and equivalent State-Of-Charge (SOC), which is made possible by the individual modeling of HVAC and building systems within the co-simulation framework. The ability to simulate individual effects in this way, which enables their incorporation into Distributed Energy Resource (DER) control methodologies, is integral for consideration of occupant thermal comfort during HVAC system control events.

Chapter 6

Conclusions

In this final chapter, the conclusions and contributions of the dissertation are summarized. Future research is recommended with a view at possible further progress in the subject area.

6.1 Summary

Novel multi-objective optimization methodologies were proposed in Chapter 2 for power distribution systems (PDSs) planning of capacitors rating and placement on three actual large-scale utility sub-circuits, which are collectively referred to KUs1. Two formulations were provided, each with four associated methods that were compared and discussed. A solution selection method through a pseudo-weight vector approach was also developed to compare selected configurations through sub-circuit analyses. Considerable improvements and associated costs were discussed for the three example circuits with respect to their corresponding reference cases. The evaluation of capacitor efficacy over time through time-series simulation and stochastic analysis was also presented in this chapter.

Chapter 3 includes new methods that adapt the optimization techniques studied in Chapter 2 to improve operation and control of PDSs over time. Circuits experience

continuous change in load and bus voltage over time due to weather and appliance use patterns. Conventional control was performed as a base case with typically available devices, such as switchable capacitors, LTC transformers, and voltage regulators. This control was optimized over time such that total energy use and utility asset degradation is minimized while remaining operationally compliant to traditional standards. Studies were based on the T1 sub-circuit from KUs1 with load data measured at the main transformer that allows for individual simulation over time and estimated equivalent ZIP parameters that capture voltage-dependency of loads.

Chapter 4 identified the significant opportunity for reducing energy use in the residential sector through high efficiency technologies and by increasing distributed Photo-Voltaic (PV) generation through the experimentation and simulation of buildings, Heating, Ventilation, and Air-Conditioning (HVAC) systems, and solar PV energy models as well as through comparison of schedule-based household devices such as water heaters and typical appliances. As an example, a simulated HVAC system upgrade without changes to the building was determined to reduce HVAC energy use by 26%, or 13% of the total building energy use. Incorporating improved construction significantly increases savings by 57% with a 46% reduction in HVAC system peak hourly power. Such improvements further enable residences to become Net-Zero-Energy (NZE), which is evident by the studied reduction in solar PV rating requirement by up to 55% depending on location.

Also considered in this chapter is the increasing prevalence of power electronics converters in modern electric loads. A survey of typical residential appliance Power Factor (PF) values and energy characteristics as well as a proposed approach for

equivalent PF calculation was provided, which may be employed at the community level for studies on residential reactive power contributions. A method to apply equivalent PF to the EnergyPlus building energy modeling software was also proposed to determine reactive power contributions from simulated loads.

In chapter 5, a novel co-simulation framework was employed to optimize Virtual Power Plant (VPP) controls that leverage HVAC systems as Generalized Energy Storage (GES) to reduce a targeted distribution system power peak, while better utilizing Behind-The-Meter (BTM) solar PV locally. The incorporation of HVAC system phasing and gradual setpoint change functions effectively prevented power system peaking or dropping from start or completion of controls.

The minimization of on-peak maximum power reduction and possible resulting total day energy use increase can compete in certain scenarios. Therefore, the optimization produced a Pareto set of best designs with control settings that achieve a targeted maximum power reduction of 24.45% to 28.75% with corresponding increases in total day energy uses between 7.98% and 10.73%. Each design yielded improved BTM solar PV utilization by 3% to 8% because of the “load-up” timing.

From among the best control designs, a “best compromise” case was determined with a peak power reduction of 0.32MW (26.83%) and total day energy increase of 1.63MWh (8.42%). If Residential Energy Storage Systems (RESSs) were to be utilized instead to realize the same results with HVAC system control only, they would require a combined capacity of approximately 1.83MWh. Assuming a typical RESS round-trip efficiency of 86%, the RESSs would expend around 0.26MWh in total energy losses over the day. In contrast, the 1.63MWh increase in total day energy use from

the HVAC control may be recuperated over the following day(s).

For the “best compromise” optimal HVAC control case, the individual building and occupant effects were observed, including indoor temperature and equivalent state-of-charge (SOC), which was made possible by the individual modeling of HVAC and building systems within the co-simulation framework. The ability to simulate individual effects in this way, which enables their incorporation into Distributed Energy Resource (DER) control methodologies, is integral for consideration of occupant thermal comfort during HVAC system control.

6.2 Original Contributions

1. A comparative study of multi-objective optimization approaches for a power system specific problem that employ computational intelligence methods, such as Differential Evolution (DE) and the Non-Dominated Sorting Genetic Algorithm III (NSGA-III), as applied to three real large-scale utility circuits (Chapter 2).
2. A new multi-step procedure for optimal power system configuration selection that utilizes a pseudo weight vector approach based on objective priority and a systematic analysis of the most extreme configuration types (Chapter 2).
3. An efficacy evaluation approach for power system configurations through time-series simulation and stochastic analysis (Chapter 2).
4. An approach for optimal operation of PDSs through capacitor and LTC transformer control that minimizes total system power and improves its voltage-time profile (Chapter 3).

5. A cluster-based method to optimally disperse PDS device control adjustments over time through load-forecasting in order to minimize utility asset degradation and maintain best performance (Chapter 3).
6. Development of EnergyPlus models through extensive multi-annual data from experimental homes with robot-operated appliances to mimic human habitation that represent different levels of energy efficiency for U.S. houses (Chapter 4).
7. Development and demonstration of a highly scalable co-simulation framework for ultra-fast machine learning models of building electric power and indoor temperature with actual many-thousand node PDSs (Chapters 4 and 5).
8. Simulation and analysis of VPP scenarios that employ hundreds of unique buildings and their corresponding HVAC systems with other DER, such as local solar PV, through GES characterization and Consumer Technology Association (CTA) 2045 control schemes (Chapters 4 and 5).
9. Multi-objective optimization of VPP HVAC control considering peak power reduction and increased total energy use through control timing (Chapter 5).

6.3 Recommendations for Future Research

Based on the results of this Ph.D. dissertation and recent research, possible further work may include the following:

1. The load modeling for voltage dependency and time-series simulation could be improved with application of AMI data and machine learning. The studies in this work utilize the data currently available from the utility, which was

measured only at the substation transformer. This data was employed for time series simulation and equivalent ZIP parameter estimation with the assumptions that the resulting load shape and voltage dependency would be applicable to the individual loads. The models could also be extended to include distribution transformers and associated secondary voltage drop for further improvements in energy use minimization through CVR and VVO functions.

2. Further evaluation of capacitor efficacy over time may be performed with optimal control for comparison with the presented results that were produced with conventional control. The effects of inaccuracies in load forecasting on the cluster-based optimal control method could also be explored.
3. The EnergyPlus building model calibration could be automated with the new Python plugin, appropriate measured data, and computational optimization. The method employed in this work required manual adjustments as the plugin was not available at the time. Automating this process would enable much more efficient and accurate production of new building models.
4. The simulation and control optimization of VPP scenarios could be extended to include other DERs, such as water heaters, electric vehicles, and residential energy storage systems, in addition to the HVAC and solar PV systems. Study of different penetration levels could be considered as the case study provided assumes 100% community participation. The testbed may also be applied to actual large-scale utility PDS models with the models for buildings and DERs as replacements for currently employed generalized load models.

References

- [1] Beckwith Electric, “Basic Considerations for the Application of LTC Transformers and Associated Controls,” Tech. Rep. Application Note No. 17, Beckwith Electric, 118 Avenue North, Largo, Florida 33773-3724, U.S.A.
- [2] H.-D. Chiang, J.-C. Wang, O. Cockings, and H.-D. Shin, “Optimal capacitor placements in distribution systems. i. a new formulation and the overall problem,” *IEEE Transactions on Power Delivery*, vol. 5, no. 2, pp. 634–642, 1990.
- [3] M. McNamara, D. Feng, T. Pettit, and D. Lawlor, “Conservation Voltage Reduction/Volt VAR Optimization EM&V Practices,” tech. rep., United States Environmental Protection Agency, January 2017.
- [4] S. Hossan, A. Khodaei, W. Fan, A. Saber, A. Wilson, M. Baran, E. Gupta, S. Fard, M. Simms, V. He, E. Wedemeyer, H. Abdurrahim, Y. Liao, Z. Wang, Z. Morton, D. Tholomier, D. Zhao, T. A. Tran, F. Rahmatian, F. Ding, and A. Contreras, “Measurement and Verification (M&V) for Conservation Voltage Reduction (CVR),” tech. rep., IEEE Power and Energy Society CVR M&V Task Force of Volt VAR Working Group.
- [5] Z. S. Hossein, A. Khodaei, W. Fan, M. S. Hossan, H. Zheng, S. A. Fard, A. Paaso, and S. Bahramirad, “Conservation voltage reduction and volt-var optimization: Measurement and verification benchmarking,” *IEEE Access*, vol. 8, pp. 50755–50770, 2020.
- [6] M. S. Hossan, P. Jover Almirall, E. A. Passo, H. Zheng, W. Fan, S. Fard, and S. R. Kothandaraman, “Deployment of conservation voltage reduction in sample feeders: A systemwide energy-savings analysis,” *IEEE Industry Applications Magazine*, vol. 27, no. 2, pp. 36–46, 2021.
- [7] S.-J. Huang and X.-Z. Liu, “A plant growth-based optimization approach applied to capacitor placement in power systems,” *IEEE Transactions on Power Systems*, vol. 27, no. 4, pp. 2138–2145, 2012.
- [8] S. Ganguly, N. C. Sahoo, and D. Das, “Multi-objective planning of electrical distribution systems incorporating shunt capacitor banks,” in *2011 International Conference on Energy, Automation and Signal*, pp. 1–6, 2011.
- [9] N. Krami, M. A. El-Sharkawi, and M. Akherraz, “Pareto multiobjective optimization technique for reactive power planning,” in *2008 IEEE Power and*

Energy Society General Meeting - Conversion and Delivery of Electrical Energy in the 21st Century, pp. 1–6, 2008.

- [10] K. Prakash and M. Sydulu, “Particle swarm optimization based capacitor placement on radial distribution systems,” in *2007 IEEE Power Engineering Society General Meeting*, pp. 1–5, 2007.
- [11] T. P. M. Mtonga, K. K. Kaberere, and G. K. Irungu, “Optimal shunt capacitors’ placement and sizing in radial distribution systems using multiverse optimizer,” *IEEE Canadian Journal of Electrical and Computer Engineering*, vol. 44, no. 1, pp. 10–21, 2021.
- [12] P. Díaz, M. Pérez-Cisneros, E. Cuevas, O. Camarena, F. A. Fausto Martinez, and A. González, “A swarm approach for improving voltage profiles and reduce power loss on electrical distribution networks,” *IEEE Access*, vol. 6, pp. 49498–49512, 2018.
- [13] A. Jafari, H. Ganjeh Ganjehlou, T. Khalili, B. Mohammadi-Ivatloo, A. Bidram, and P. Siano, “A two-loop hybrid method for optimal placement and scheduling of switched capacitors in distribution networks,” *IEEE Access*, vol. 8, pp. 38892–38906, 2020.
- [14] S. Gupta, V. K. Yadav, and M. Singh, “Optimal allocation of capacitors in radial distribution networks using shannon’s entropy,” *IEEE Transactions on Power Delivery*, vol. 37, no. 3, pp. 2245–2255, 2022.
- [15] L. A. Gallego, J. M. López-Lezama, and O. G. Carmona, “A mixed-integer linear programming model for simultaneous optimal reconfiguration and optimal placement of capacitor banks in distribution networks,” *IEEE Access*, vol. 10, pp. 52655–52673, 2022.
- [16] A. Águila, L. Ortiz, R. Orizondo, and G. López, “Optimal location and dimensioning of capacitors in microgrids using a multicriteria decision algorithm,” *Heliyon*, vol. 7, no. 9, p. e08061, 2021.
- [17] E. A. Almabsout, R. A. El-Sehiemy, O. N. U. An, and O. Bayat, “A hybrid local search-genetic algorithm for simultaneous placement of dg units and shunt capacitors in radial distribution systems,” *IEEE Access*, vol. 8, pp. 54465–54481, 2020.
- [18] A. Noori, Y. Zhang, N. Nouri, and M. Hajivand, “Hybrid allocation of capacitor and distributed static compensator in radial distribution networks using multi-objective improved golden ratio optimization based on fuzzy decision making,” *IEEE Access*, vol. 8, pp. 162180–162195, 2020.
- [19] M. Ahmadi, M. S. S. Danish, M. E. Lotfy, A. Yona, Y.-Y. Hong, and T. Senjyu, “Multi-objective time-variant optimum automatic and fixed type of capacitor bank allocation considering minimization of switching steps,” *AIMS Energy*, vol. 7, no. 6, pp. 792–818, 2019.

- [20] A. A. Ejajal and M. E. El-Hawary, “Optimal capacitor placement and sizing in unbalanced distribution systems with harmonics consideration using particle swarm optimization,” *IEEE Transactions on Power Delivery*, vol. 25, no. 3, pp. 1734–1741, 2010.
- [21] J. H. D. Onaka, A. S. de Lima, A. R. A. Manito, U. H. Bezerra, M. E. L. Tostes, C. C. M. d. M. Carvalho, T. M. Soares, and D. C. Mendes, “Optimal capacitor banks placement in distribution grids using NSGA II and harmonic resonance chart,” in *2016 17th International Conference on Harmonics and Quality of Power (ICHQP)*, pp. 89–94, 2016.
- [22] C.-F. Chang, “Reconfiguration and capacitor placement for loss reduction of distribution systems by ant colony search algorithm,” *IEEE Transactions on Power Systems*, vol. 23, no. 4, pp. 1747–1755, 2008.
- [23] M. Diaz-Aguiló, J. Sandraz, R. Macwan, F. de León, D. Czarkowski, C. Comack, and D. Wang, “Field-Validated Load Model for the Analysis of CVR in Distribution Secondary Networks: Energy Conservation,” *IEEE Transactions on Power Delivery*, vol. 28, no. 4, pp. 2428–2436, 2013.
- [24] H. Ahmadi, J. R. Martí, and H. W. Dommel, “A framework for volt-var optimization in distribution systems,” *IEEE Transactions on Smart Grid*, vol. 6, no. 3, pp. 1473–1483, 2015.
- [25] Z. S. Hossein, A. Khodaei, W. Fan, M. S. Hossan, H. Zheng, S. A. Fard, A. Paaso, and S. Bahramirad, “Conservation voltage reduction and volt-var optimization: Measurement and verification benchmarking,” *IEEE Access*, vol. 8, pp. 50755–50770, 2020.
- [26] Z. Wang and J. Wang, “Review on implementation and assessment of conservation voltage reduction,” *IEEE Transactions on Power Systems*, vol. 29, no. 3, pp. 1306–1315, 2014.
- [27] Y. Zhang, Y. Liao, E. Jones, N. Jewell, and D. Ionel, “ZIP load modeling for single and aggregate loads and CVR factor estimation,” *International Journal of Emerging Electric Power Systems*, vol. 23, pp. 839–858, Aug. 2022.
- [28] United States Energy Information Administration (EIA), “Use of energy explained, monthly energy review, table 2.1.” <https://www.eia.gov/energyexplained/use-of-energy/>, 2021. Accessed: April, 2021.
- [29] United States Energy Information Administration (EIA), “2015 residential energy consumption survey.” <https://www.eia.gov/energyexplained/use-of-energy/electricity-use-in-homes.php/>, 2019. Accessed: May, 2019.
- [30] United States Energy Information Administration (EIA), “2015 residential energy consumption survey.” <https://www.eia.gov/energyexplained/use-of-energy/homes.php>, 2019. Accessed: May, 2019.

- [31] H. Gong, E. S. Jones, R. E. Alden, A. G. Frye, D. Colliver, and D. M. Ionel, “Virtual power plant control for large residential communities using hvac systems for energy storage,” *IEEE Transactions on Industry Applications*, vol. 58, no. 1, pp. 622–633, 2022.
- [32] United States Department of Energy, “Energy Data Facts.” <https://rpsc.energy.gov/energy-data-facts#:~:text=1.,the%20United%20States%20in%202014.>, 2020. Accessed: Aug. 18, 2020.
- [33] H. Gong, V. Rallabandi, M. L. McIntyre, E. Hossain, and D. M. Ionel, “Peak reduction and long term load forecasting for large residential communities including smart homes with energy storage,” *IEEE Access*, vol. 9, pp. 19345–19355, 2021.
- [34] K. E. K. Schmitt, I. Osman, R. Bhatta, M. Murshed, M. Chamana, and S. Bayne, “A dynamic load control strategy for an efficient building demand response,” in *2021 IEEE Energy Conversion Congress and Exposition (ECCE)*, pp. 819–826, 2021.
- [35] Y. Singh, B. Singh, and S. Mishra, “Control strategy for multiple residential solar pv systems in distribution network with improved power quality,” in *2021 IEEE Energy Conversion Congress and Exposition (ECCE)*, pp. 919–924, 2021.
- [36] H. W. Yan, G. G. Farivar, N. Beniwal, N. B. Y. Gorla, H. D. Tafti, S. Ceballos, J. Pou, and G. Konstantinou, “Comparative study of coordinated photovoltaic and battery control strategies on the battery lifetime in stand-alone dc microgrids,” in *2021 IEEE Energy Conversion Congress and Exposition (ECCE)*, pp. 1034–1039, 2021.
- [37] Electrical Transient and Analysis Program, “Optimal Capacitor Placement: Costs Benefits Due to Loss Reductions,” tech. rep., Operation Technology, Inc., 17 Goodyear, Irvine, CA 92618.
- [38] J. Cabral Leite, I. Pérez Abril, and M. S. Santos Azevedo, “Capacitor and passive filter placement in distribution systems by nondominated sorting genetic algorithm-ii,” *Electric Power Systems Research*, vol. 143, pp. 482–489, 2017.
- [39] J. H. Onaka, U. H. Bezerra, M. E. Tostes, and Áthila S. Lima, “A posteriori decision analysis based on resonance index and nsga-ii applied to the capacitor banks placement problem,” *Electric Power Systems Research*, vol. 151, pp. 296–307, 2017.
- [40] L. A. Gallego, J. M. López-Lezama, and O. G. Carmona, “A mixed-integer linear programming model for simultaneous optimal reconfiguration and optimal placement of capacitor banks in distribution networks,” *IEEE Access*, vol. 10, pp. 52655–52673, 2022.

- [41] J. M. Home-Ortiz, R. Vargas, L. H. Macedo, and R. Romero, “Joint reconfiguration of feeders and allocation of capacitor banks in radial distribution systems considering voltage-dependent models,” *International Journal of Electrical Power & Energy Systems*, vol. 107, pp. 298–310, 2019.
- [42] E. A. Almabsout, R. A. El-Sehiemy, O. N. U. An, and O. Bayat, “A hybrid local search-genetic algorithm for simultaneous placement of dg units and shunt capacitors in radial distribution systems,” *IEEE Access*, vol. 8, pp. 54465–54481, 2020.
- [43] S. Das, D. Das, and A. Patra, “Operation of distribution network with optimal placement and sizing of dispatchable dgs and shunt capacitors,” *Renewable and Sustainable Energy Reviews*, vol. 113, p. 109219, 2019.
- [44] T. P. Nguyen, T. A. Nguyen, T. V.-H. Phan, and D. N. Vo, “A comprehensive analysis for multi-objective distributed generations and capacitor banks placement in radial distribution networks using hybrid neural network algorithm,” *Knowledge-Based Systems*, vol. 231, p. 107387, 2021.
- [45] S. F. Santos, D. Z. Fitiwi, M. Shafie-Khah, A. W. Bizuayehu, C. M. P. Cabrita, and J. P. S. Catalão, “New multistage and stochastic mathematical model for maximizing res hosting capacity—part i: Problem formulation,” *IEEE Transactions on Sustainable Energy*, vol. 8, no. 1, pp. 304–319, 2017.
- [46] A. Jafari, H. Ganjeh Ganjehlou, T. Khalili, B. Mohammadi-Ivatloo, A. Bidram, and P. Siano, “A two-loop hybrid method for optimal placement and scheduling of switched capacitors in distribution networks,” *IEEE Access*, vol. 8, pp. 38892–38906, 2020.
- [47] A. Noori, Y. Zhang, N. Nouri, and M. Hajivand, “Multi-objective optimal placement and sizing of distribution static compensator in radial distribution networks with variable residential, commercial and industrial demands considering reliability,” *IEEE Access*, vol. 9, pp. 46911–46926, 2021.
- [48] M. Babanezhad, S. Arabi Nowdeh, A. Y. Abdelaziz, K. M. AboRas, and H. Kotb, “Reactive power based capacitors allocation in distribution network using mathematical remora optimization algorithm considering operation cost and loading conditions,” *Alexandria Engineering Journal*, vol. 61, no. 12, pp. 10511–10526, 2022.
- [49] J. Deboever and M. R. Rylander, “Enhanced Load Modeling: Improved Reactive Power Load Modeling,” Tech. Rep. 000000003002022354, Electric Power Research Institute (EPRI), August 2021.
- [50] S. Duerr, C. Ababei, and D. M. Ionel, “A case for using distributed energy storage for load balancing and power loss minimization in distribution networks,” *Electric Power Components and Systems*, vol. 48, no. 9-10, pp. 1063–1076, 2020.

- [51] Electric Power Research Institute, “OpenDSS.” <https://www.epri.com/pages/sa/opensdss>. Accessed: 2023-5-1.
- [52] Z. Wang, M. Begovic, and J. Wang, “Analysis of conservation voltage reduction effects based on multistage svr and stochastic process,” *IEEE Transactions on Smart Grid*, vol. 5, no. 1, pp. 431–439, 2014.
- [53] H. Gong, E. S. Jones, and D. M. Ionel, “An Aggregated and Equivalent Home Model for Power System Studies with Examples of Building Insulation and HVAC Control Improvements,” in *2020 IEEE Power and Energy Society General Meeting (PESGM)*, pp. 1–4, 2020.
- [54] H. Gong, E. S. Jones, A. H. M. Jakaria, A. Huque, A. Renjit, and D. M. Ionel, “Large-scale modeling and dr control of electric water heaters with energy star and CTA-2045 control types in distribution power systems,” *IEEE Transactions on Industry Applications*, vol. 58, no. 4, pp. 5136–5147, 2022.
- [55] E. S. Jones, R. E. Alden, H. Gong, A. G. Frye, D. Colliver, and D. M. Ionel, “The effect of high efficiency building technologies and pv generation on the energy profiles for typical us residences,” in *2020 9th International Conference on Renewable Energy Research and Application (ICRERA)*, pp. 471–476, 2020.
- [56] H. Gong, E. S. Jones, A. H. M. Jakaria, A. Huque, A. Renjit, and D. M. Ionel, “Generalized Energy Storage Model-In-the-Loop Suitable for Energy Star and CTA-2045 Control Types,” in *2021 IEEE Energy Conversion Congress and Exposition (ECCE)*, pp. 814–818, 2021.
- [57] R. Storn and K. Price, “Differential Evolution - A Simple and Efficient Heuristic for Global Optimization over Continuous Spaces,” *Journal of Global Optimization*, vol. 11, no. 4, pp. 341–359, 1997.
- [58] K. Deb, A. Pratap, S. Agarwal, and T. Meyarivan, “A fast and elitist multiobjective genetic algorithm: NSGA-II,” *IEEE Transactions on Evolutionary Computation*, vol. 6, no. 2, pp. 182–197, 2002.
- [59] A. Ibrahim, S. Rahnamayan, M. V. Martin, and K. Deb, “EliteNSGA-III: An improved evolutionary many-objective optimization algorithm,” in *2016 IEEE Congress on Evolutionary Computation (CEC)*, pp. 973–982, 2016.
- [60] I. Das and J. E. Dennis, “Normal-boundary intersection: A new method for generating the pareto surface in nonlinear multicriteria optimization problems,” *SIAM Journal on Optimization*, vol. 8, no. 3, pp. 631–657, 1998.
- [61] J. Blank and K. Deb, “pymoo: Multi-objective optimization in python,” *IEEE Access*, vol. 8, pp. 89497–89509, 2020.
- [62] Y. Yang, S. Li, W. Li, and M. Qu, “Power load probability density forecasting using gaussian process quantile regression,” *Applied Energy*, vol. 213, pp. 499–509, 2018.

- [63] Y. Zhang, Y. Liao, E. Jones, N. Jewell, and D. M. Ionel, “Kalman filter based approach for zip load modeling for aggregate loads,” in *2021 IEEE Kansas Power and Energy Conference (KPEC)*, pp. 1–6, 2021.
- [64] M. S. Hossan, H. M. Mesbah Maruf, and B. Chowdhury, “Comparison of the ZIP load model and the exponential load model for CVR factor evaluation,” in *2017 IEEE Power and Energy Society General Meeting*, pp. 1–5, 2017.
- [65] A. Bokhari, A. Alkan, R. Dogan, M. Diaz-Aguiló, F. de León, D. Czarkowski, Z. Zabar, L. Birenbaum, A. Noel, and R. E. Uosef, “Experimental determination of the zip coefficients for modern residential, commercial, and industrial loads,” *IEEE Transactions on Power Delivery*, vol. 29, no. 3, pp. 1372–1381, 2014.
- [66] A. Bokhari, A. Raza, M. Diaz-Aguiló, F. de León, D. Czarkowski, R. E. Uosef, and D. Wang, “Combined effect of cvr and dg penetration in the voltage profile of low-voltage secondary distribution networks,” *IEEE Transactions on Power Delivery*, vol. 31, no. 1, pp. 286–293, 2016.
- [67] United States Energy Information Administration (EIA), “Frequently asked questions: How much electricity is lost in transmission and distribution in the united states?.” <https://www.eia.gov/tools/faqs/faq.php?id=105&t=3>, 2021. Accessed: May, 2021.
- [68] Energy and Environmental Economics Inc., “Residential building electrification in california: Consumer economics, greenhouse gases and grid impacts.” https://www.ethree.com/wpcontent/uploads/2019/04/E3_Residential_Building_Electrification_in_California_April_2019.pdf, 2019. Accessed: April, 2019.
- [69] A. Águila Téllez, G. López, I. Isaac, and J. González, “Optimal reactive power compensation in electrical distribution systems with distributed resources. review,” *Heliyon*, vol. 4, no. 8, 2018.
- [70] National Renewable Energy Laboratory, “Energyplus™, version 00,” 9.
- [71] National Renewable Energy Laboratory, “Building Energy Optimization Tool.” <https://beopt.nrel.gov/home>, 2020. Accessed: Aug. 18, 2020.
- [72] H. Gong, V. Rallabandi, M. L. McIntyre, and D. M. Ionel, “On the optimal energy controls for large scale residential communities including smart homes,” in *2019 IEEE Energy Conversion Congress and Exposition (ECCE)*, pp. 503–507, 2019.
- [73] K. S. Cetin, M. H. Fathollahzadeh, N. Kunwar, H. Do, and P. C. Tabares-Velasco, “Development and validation of an hvac on/off controller in energyplus for energy simulation of residential and small commercial buildings,” *Energy and Buildings*, vol. 183, pp. 467 – 483, 2019.

- [74] ASHRAE, “Guideline 14-2014,” *Measurement of Energy, Demand, and Water Savings*, 2014.
- [75] S. Wilcox and W. Marion, “Users Manual for TMY3 Data Sets,” Tech. Rep. NREL/TP-581-43156, National Renewable Energy Laboratory, May 2008.
- [76] Boudreaux et al, “Final Review of the Campbell Creek Demonstration Showcased by Tennessee Valley Authority,” Tech. Rep. ORNL/TM-2015/666, Oak Ridge National Laboratory, Oak Ridg, Tennessee 37831-6283, June 2015.
- [77] B. Hendron and C. Engebrecht, “Building America House Simulation Protocols,” Tech. Rep. NREL/TP-550-49426, National Renewable Energy Laboratory, October 2010.
- [78] E. S. Jones, H. Gong, and D. M. Ionel, “Optimal combinations of utility level renewable generators for a net zero energy microgrid considering different utility charge rates,” in *2019 8th International Conference on Renewable Energy Research and Applications (ICRERA)*, pp. 1014–1017, 2019.
- [79] M. J. Ghorbani; and H. Mokhtari, “Impact of harmonics on power quality and losses in power distribution systems,” *International Journal of Electrical and Computer Engineering*, vol. 5, pp. 166–174, 2015.
- [80] M. Pipattanasomporn; M. Kuzlu; S. Rahman and Y. Teklu, “Load profiles of selected major household appliances and their demand response opportunities,” *IEEE Transactions on Smart Grid*, vol. 5, no. 2, pp. 742–750, 2014.
- [81] P. Meehan; C. McArdle; and S. Daniels, “An efficient, scalable time-frequency method for tracking energy usage of domestic appliances using a two-step classification algorithm,” *Energie*, vol. 7, no. 11, pp. 7041–7066, 2014.
- [82] L. M. Hajagos and B. Danai, “Laboratory measurements and models of modem loads and their effect on voltage stability studies,” *IEEE Transactions on Power Systems*, vol. 13, no. 2, pp. 584–592, 1998.
- [83] D. Shmilovits, J. Duan, D. Czarkowski, Z. Zabar, and S. Lee, “Characteristics of modern nonlinear loads and their influence on systems with distributed generation,” *Int. J. Energy Technology and Policy*, vol. 5, no. 2, 2007.
- [84] P. M. Ostendorp; K. Dayem; C. Mercier; and E. Rubin, “Power factor requirements for electronic loads in california,” Tech. Rep. 19-AAER-03, 2014 ACEEE Summer Study on Energy Efficiency in Buildings, February 2020.
- [85] B. Fortenbery, “Power factor requirements for electronic loads in california,” tech. rep., 2014 ACEEE Summer Study on Energy Efficiency in Buildings, Asilomar, California, August 2014.
- [86] R. E. Alden, H. Gong, C. Ababei, and D. M. Ionel, “Lstm forecasts for smart home electricity usage,” in *2020 9th International Conference on Renewable Energy Research and Application (ICRERA)*, pp. 434–438, 2020.

- [87] R. E. Alden, P. Han, and D. M. Ionel, “Smart plug and circuit breaker technologies for residential buildings in the us,” in *2019 8th International Conference on Renewable Energy Research and Applications (ICRERA)*, pp. 1018–1021, 2019.
- [88] Codes and Standards Enhancement (CASE) Initiative, “California investor owned utilities comments response to invitation to submit proposals - power factor,” Tech. Rep. 17-AAER-12, California Investor Owned Utilities, September 2017.
- [89] E. Heydarian-Forushani, S. Ben Elghali, M. Zerrougui, M. La Scala, and P. Mestre, “An auction-based local market clearing for energy management in a virtual power plant,” *IEEE Transactions on Industry Applications*, vol. 58, no. 5, pp. 5724–5733, 2022.
- [90] G. Barchi, M. Pierro, and D. Moser, “Predictive energy control strategy for peak shaving and shifting using bess and pv generation applied to the retail sector,” *Electronics*, vol. 8, no. 5, 2019.
- [91] X. Zhang, C. Huang, and J. Shen, “Energy optimal management of microgrid with high photovoltaic penetration,” *IEEE Transactions on Industry Applications*, vol. 59, no. 1, pp. 128–137, 2023.
- [92] N. S. Kelepouris, A. I. Nousedilis, A. S. Bouhouras, and G. C. Christoforidis, “Cost-effective hybrid pv-battery systems in buildings under demand side management application,” *IEEE Transactions on Industry Applications*, vol. 58, no. 5, pp. 6519–6528, 2022.
- [93] J. Martinez-Rico, E. Zulueta, I. R. de Argandoña, M. Armendia, and U. Fernandez-Gamiz, “Sizing a battery energy storage system for hybrid renewable power plants based on optimal market participation under different market scenarios,” *IEEE Transactions on Industry Applications*, vol. 58, no. 5, pp. 5624–5634, 2022.
- [94] H. M. Abdeltawab and Y. A. I. Mohamed, “Distributed battery energy storage co-operation for renewable energy sources integration,” *Energies*, vol. 13, no. 20, 2020.
- [95] F. Fan, G. Zorzi, D. Campos-Gaona, G. Burt, O. Anaya-Lara, J. Nwobu, and A. Madariaga, “Sizing and coordination strategies of battery energy storage system co-located with wind farm: The uk perspective,” *Energies*, vol. 14, no. 5, 2021.
- [96] A. Saif, S. K. Khadem, M. F. Conlon, and B. Norton, “Impact of distributed energy resources in smart homes and community-based electricity market,” *IEEE Transactions on Industry Applications*, vol. 59, no. 1, pp. 59–69, 2023.
- [97] B. D. Biswas, M. S. Hasan, and S. Kamalasan, “Decentralized distributed convex optimal power flow model for power distribution system based on alternating direction method of multipliers,” *IEEE Transactions on Industry Applications*, vol. 59, no. 1, pp. 627–640, 2023.

- [98] E. S. Jones, R. E. Alden, H. Gong, A. Al Hadi, and D. M. Ionel, “Co-simulation of smart grids and homes including ultra-fast hvac models with cta-2045 control and consideration of thermal comfort,” in *2022 IEEE Energy Conversion Congress and Exposition (ECCE)*, pp. 1–6, 2022.
- [99] Consumer Technology Association (CTA), “CTA standard: Modular communications interface for energy management,” tech. rep., 2020.
- [100] E. S. Jones, R. E. Alden, H. Gong, A. G. Frye, D. Colliver, and D. M. Ionel, “The effect of high efficiency building technologies and pv generation on the energy profiles for typical us residences,” in *2020 9th International Conference on Renewable Energy Research and Application (ICRERA)*, pp. 471–476, 2020.
- [101] R. E. Alden, E. S. Jones, S. B. Poore, H. Gong, A. Al Hadi, and D. M. Ionel, “Digital twin for hvac load and energy storage based on a hybrid ml model with cta-2045 controls capability,” in *2022 IEEE Energy Conversion Congress and Exposition (ECCE)*, pp. 1–5, 2022.
- [102] Electric Power Research Institute, “DOE SHINES Residential Demonstration.” <https://dashboards.epri.com/shines-residential/dashboard>, 2020. Accessed: Aug. 4, 2020.
- [103] K. P. Schneider, B. A. Mather, B. C. Pal, C.-W. Ten, G. J. Shirek, H. Zhu, J. C. Fuller, J. L. R. Pereira, L. F. Ochoa, L. R. de Araujo, R. C. Dugan, S. Matthias, S. Paudyal, T. E. McDermott, and W. Kersting, “Analytic considerations and design basis for the ieeee distribution test feeders,” *IEEE Transactions on Power Systems*, vol. 33, no. 3, pp. 3181–3188, 2018.
- [104] E. Wood, C. Rames, M. Muratori, S. Raghavan, and M. Melaina, “National Plug-In Electric Vehicle Infrastructure Analysis.” Accessed: 2023-03-12.
- [105] H. Gong, T. Rooney, O. M. Akeyo, B. T. Braneky, and D. M. Ionel, “Equivalent electric and heat-pump water heater models for aggregated community-level demand response virtual power plant controls,” *IEEE Access*, vol. 9, pp. 141233–141244, 2021.
- [106] Tesla, Inc., “Tesla PowerWall Specifications.” <https://www.tesla.com/support/energy/powerwall/documents/documents>. Accessed: 2023-5-1.
- [107] National Renewable Energy Laboratory, “National Renewable Energy Laboratory Annual Technology Baseline.” https://atb.nrel.gov/electricity/2022/residential_battery_storage. Accessed: 2023-03-13.

Vita

Evan S. Jones, Ph.D. Candidate

Department of Electrical and Computer Engineering, University of Kentucky

Evan S. Jones is a Ph.D. candidate in electrical engineering and a GAANN Graduate Fellow in the SPARK Laboratory at the University of Kentucky (UK), Lexington, KY, USA. He received two B.S. degrees in electrical engineering and computer engineering with a minor in computer science, as well as an undergraduate certificate for studies in power and energy from UK in 2019. During his undergraduate studies, he worked concurrently as a student electrical engineer for the East Kentucky Power Cooperative (EKPC). There, he helped to maintain and deploy advanced supervisory control and data acquisition (SCADA) systems in transmission and distribution substations across Kentucky. At UK, he served as the inaugural vice president for the IEEE PES and IAS joint student chapter and was an L. Stanley Pigman and IEEE PES scholar. In 2020, he was awarded a multi-year GAANN Ph.D. Fellowship administered by the U.S. Department of Education. He worked as both a teaching and research assistant on projects sponsored by the Department of Energy (DOE), National Science Foundation (NSF), Tennessee Valley Authority (TVA), Louisville Gas and Electric and Kentucky Utilities (LG&E and KU), part of the PPL Corporation family of companies, and the Electric Power Research Institute (EPRI). His main research focuses on Building Energy Modeling (BEM), Distributed Energy Resources (DERs), Virtual Power Plant (VPP) control, and optimal planning and operation of electric power distribution systems.